From the Department of Clinical Neuroscience

Karolinska Institutet, Stockholm, Sweden

DEVELOPMENT OF RADIOFREQUENCY PULSES FOR FAST AND MOTION-ROBUST BRAIN MRI

Ola Norbeck

Karolinska Institutet

Stockholm 2020

Published by Karolinska Institutet.
Printed by Universitetsservice US-AB.

ISBN 978-91-7831-869-8

DEVELOPMENT OF RADIOFREQUENCY PULSES FOR FAST AND MOTION-ROBUST BRAIN MRI

THESIS FOR DOCTORAL DEGREE (Ph.D.)

By

Ola Norbeck

Principal Supervisor:
Assoc. Prof. Stefan Skare, Ph.D.
Karolinska Institutet
Department of Clinical Neuroscience

Co-supervisors:
Enrico Avventi, Ph.D.
Karolinska Institutet
Department of Clinical Neuroscience

Mathias Engström, Ph.D.
GE Healthcare

Opponent:
Assoc. Prof. Lars Hanson, Ph.D.
Technical University of Denmark
DTU Health Tech
Center for Magnetic Resonance
&
Copenhagen University Hospital
Hvidovre
Danish Research Centre for Magnetic Resonance

Examination Board:
Assoc. Prof. Jonas Svensson, Ph.D.
Lund University
Department of Medical Radiation Physics

Assoc. Prof. Gunther Helms, Ph.D.
Lund University
Medical Radiation Physics
Department for Clinical Sciences Lund (IKVL)

Andreas Sigfridsson, Ph.D.
Karolinska Institutet
Department of Molecular Medicine and Surgery
Division of Clinical Physiology

Abstract

This thesis is based on three projects and the three scientific articles that were the result of each project. Each project deals with various kinds of technical software development in the field of magnetic resonance imaging (MRI). The projects are in many ways very different, encompassing several acquisition and reconstruction strategies. However, there are at least two common denominators. The first is the projects shared the same goal of producing fast and motion robust methods. The second common denominator is that all the projects were carried out with a particular focus on the radiofrequency (RF) pulses used.

The first project combined the acceleration method simultaneous multi-slice (SMS) with the acquisition method called PROPELLER. This combination was utilized to acquire motion-corrected thin-sliced reformattable T2-weighted and T1-FLAIR image volumes, thereby producing a motion robust alternative to 3D sequences.

The second project analyzed the effect of the excitation RF pulse on T1-weighted images acquired with 3D echo planar imaging (EPI). It turned out that an RF pulse that reduced magnetization transfer (MT) effects significantly increased the gray/white matter contrast. The 3D EPI sequence was then used to rapidly image tumor patients after gadolinium enhancement.

The third project combined PROPELLER's retrospective motion correction with the prospective motion correction of an intelligent marker (the WRAD). With this combination, sharp T1-FLAIR images were acquired during large continuous head movements.

List of Scientific Papers

I. Simultaneous Multi-Slice combined with PROPELLER
***Ola Norbeck**, Enrico Avventi, Mathias Engström, Henric Rydén, & Stefan Skare.*
2018. Magnetic Resonance in Medicine: 80(2), 496–506.
https://doi.org/10.1002/mrm.27041

II. Optimizing 3D EPI for Rapid T1-weighted Imaging
***Ola Norbeck**, Tim Sprenger, Enrico Avventi, Henric Rydén, Annika Kits, Johan Berglund, & Stefan Skare.*
2020. Magnetic Resonance in Medicine: 84, 1441–1455.
https://doi.org/10.1002/mrm.28222

III. T1-w FLAIR imaging during continuous head motion: combining PROPELLER with an intelligent marker
***Ola Norbeck**, Adam van Niekerk, Enrico Avventi, Henric Rydén, Johan Berglund, Tim Sprenger, & Stefan Skare.*
Magnetic Resonance in Medicine: Accepted for publication 20-07-24

Contents

List of Abbreviations

MRI	Magnetic Resonance Imaging
B_0	Main magnetic field
B_1	Radiofrequency magnetic field
BW	Bandwidth
CPMG	Carr Purcell Meiboom Gill
ETL	Echo Train Length
EPI	Echo Planar Imaging
ESP	Echo Spacing
FA	Flip Angle
FLAIR	Fluid Attenuated Inversion Recovery
fMRI	Functional magnetic resonance imaging
FOV	Field of view
GRE	Gradient Echo
IR	Inversion Recovery
rBW	Receiver Bandwidth
SE	Spin Echo
SNR	Signal-to-noise ratio
CNR	Contrast-to-noise ratio
TE	Echo Time
SPSP	Spectral Spatial
TR	Repetition Time
WM	White Matter
GM	Gray Matter
RF	Radiofrequency
PSD	Pulse Sequence Diagram
SLR	Shinnar–Le Roux
WRAD	Wireless Radiofrequency Triggered Acquisition Device

PROPELLER	Periodically Rotated Overlapping Parallel Lines with Enhanced Reconstruction
SMS	Simultaneous Multi-Slice
CAIPIRINHA	Controlled Aliasing in Parallel Imaging Results in Higher Acceleration
PMC	Prospective Motion Correction
RMC	Retrospective Motion Correction
M	Net magnetization
M_0	Initial maximum value of M
M_z	Longitudinal magnetization
M_{xy}	Transverse magnetization
MT	Magnetization Transfer
FT	Fourier Transform
EPG	Extended Phase Graphs
PINS	Power Independent of Number of Slices
SENSE	Sensitivity Encoding
GRAPPA	Generalized Autocalibrating Partial Parallel Acquisition
RARE	Rapid Acquisition with Relaxation Enhancement
TRAPS	Smooth Transitions between Pseudo Steady States
ACS	Auto Calibration Signal
SAR	Specific Absorption Rate
WE	Water Excitation
p3D	Pseudo 3D
PI	Parallel Imaging
2D	Two Dimensional
3D	Three Dimensional
FIR	Finite Impulse Response
SPGR	Spoiled Gradient Echo

1 Thesis Overview

This thesis begins with a popular science introduction, followed by a chapter on the background and theory, which covers MRI physics, focusing on the details that are relevant to the methods and algorithms used in the studies. Since one of the main intended learning outcomes of this PhD project was an understanding of radiofrequency pulses, the background and theory chapter begins with an introduction to fundamental radiofrequency theory. It then continues with a rundown SMS acceleration methods. Finally, the chapter details issues of motion during the process of acquiring an image. Since the author is employed at a neuroradiology department, the thesis has a strong focus on neurological imaging and its specific problems with head motion.

Next, the aim of the thesis is stated, which explains the hypothesis and goals of the three sub-projects and subsequent scientific papers. The following chapter overviews several of the methodological choices made during the three projects, including additional results to support the motivations. The final chapter provides an overview of the results and discussion, which also includes unpublished research results, future developments and thoughts on the limitations of the projects.

2 Popular Science Introduction

Anyone who has undergone an MRI examination will probably tell you that it was loud and fairly boring (or even claustrophobic). An MRI scan can last up to an hour, during which time you have to lie perfectly still. If that sounds difficult, imagine that you are a kid that cannot sit still for 30 seconds or that you have a disease that makes it hard to remain stationary. In other words, an MRI procedure would be better if it was faster and not so sensitive to motion.

MRI is a technique used to look inside the body by placing it inside the bore of a large magnet where magnetic fields are bounced against it. This makes it possible to locate and recognize different tissues. The MRI machine typically produces cross sections of the body, which can be used to identify various diseases. There are three examples of different cross sections shown in Figure 1. There exists a wide variety of different types of MRI images; for example, water can be bright in one and dark in another type of image. By combining information from several images, a radiologist can identify diseases.

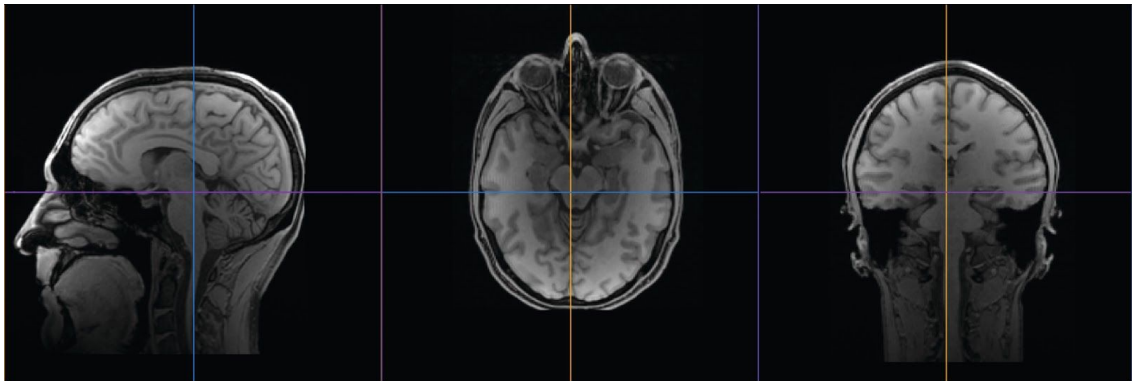

Figure 1. *Three cross sections through the author's brain.*

In the last 70 years since the birth of MRI, physicists, mathematicians and engineers have been able to greatly increase the speeds and robustness at which an MRI scanner operates. Nevertheless, it can take between 1 to 10 minutes to produce an image. One can imagine how still a person would have to remain if it took 10 minutes to take their photograph with a regular camera. MRI has the same

problem; the patient must remain as still as possible for those 10 minutes. Otherwise, the images become blurry and corrupted.

This book revolves around three scientific articles, all of which are included at the end of the book. They each describe a particular step to further improve the methods used to image the head with an MRI machine and tackle both the slowness of the MRI and its sensitivity to motion.

The first article is about a seemingly simple trick that has been used by other researchers to reduce the time it takes to produce an MRI image by up to 15 times: taking several pictures at the same time. When shooting a large number of pictures with an old analog camera at high speed, the process is significantly slowed down by winding the film roll to produce a fresh frame. The process would go much faster if it was possible to shoot several of the images on the same frame. This would produce overlaid images on each frame, which might have artistic qualities but would not be very informative. However, if pictures are taken at the same time with an MRI camera, which is a very different machine than an analog one, it is possible to disentangle the overlaid images and construct them as separate pictures (see Figure 2).

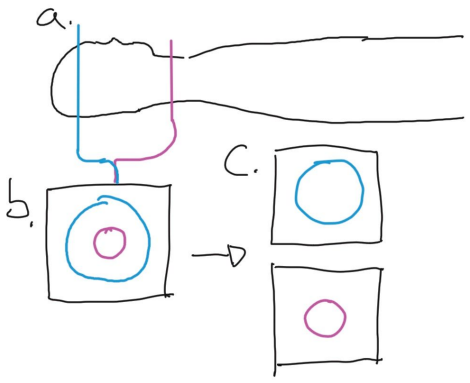

Figure 2. *Images from two locations in the body (a) are taken at the same time. They are overlaid on each other (b), but can be separated (c).*

This method is called *simultaneous multi-slice* or SMS for short. In this project, SMS was used for the first time to speed up a specific technique of producing images that are less sensitive to movement, called PROPELLER. The PROPELLER technique divides the imaging process into shorter steps and takes many low-resolution images, during which there is no time to move. These snapshot images are then combined into a high-resolution image.

The second project demonstrates how a rapid imaging method can be utilized if used correctly. Images like the ones in Figure 1 covering the whole head are scanned in just 24 seconds. Speeding up the MRI scans unlocks many possibilities both for science and medicine. Scientists trying to map and understand how the mind works can obtain extremely high-resolution images of the brain. At hospitals, faster scans can lead to increased patient comfort, since it reduces the time spent in the scanner. In some cases, higher image quality can be achieved, which in turn helps the radiologists make more accurate diagnoses.

The third article focuses on MRI images taken when the person in the scanner moves too much. This is accomplished by tracking the head with a small device attached to the person's nose. The scanner can then adapt to the position of the head and produce sharp images of it even though when it moves. In the future, such a technique could be used to take MRI images of patient groups that find it difficult to lie still, such as kids.

3 Background and Theory

In this chapter the theory of the three main topics of the thesis are explored; the topics being: RF pulses, acceleration via SMS, and motion correction. The chapter begins with a section on radio frequency pulses, which starts from the basic MRI physics and goes through several of the methods and techniques later used in the three projects of the thesis. The second section reviews SMS acceleration; including: multiband RF pulses, reconstruction methods, and applications of SMS. The last section discusses motion correction, with a focus on two techniques used in subsequent studies.

3.1 Radio Frequency Pulses

3.1.1 An abbreviated history of MRI

Following Rabi's 1937 experiments investigating the magnetic moments of atoms and nuclei (1), nuclear magnetic resonance in bulk matter was discovered in 1945 by two independent research groups – Felix Bloch's group at Harvard and by Edvard Purcell's group at Stanford (2,3). Even though they were working on similar research, Bloch and Purcell had different backgrounds and therefore addressed the subject in different ways. Bloch's interpretation was based on classical physics including induction and magnetic fields. Purcell, on the other hand, viewed the phenomenon as quantum mechanical with quantized states and energy transfers. More details on the history of these Nobel prize-winning discoveries that laid the ground for what MRI has become today can be found in Ref. (4). The two approaches (the classical and the quantum mechanical) have since been used to explain the concept of MRI, both in textbooks and lectures, sometimes separate and sometimes in a confusing mix. The more intuitive classical view of Bloch (5) is fully adequate to explain the vast majority of MRI phenomena (6) and will, therefore, be used in the following short introduction to the physics of MRI.

3.1.2 Exciting spins and receiving their signal

At the heart of MRI is the hydrogen (^{1}H) proton. It is abundant in the human body due to its inclusion in both water and fat. It also possesses a number of practical

properties making it ideal to use for MR imaging. The proton exhibits an intrinsic quantum mechanical property called *nuclear spin* and is associated with a magnetic dipole moment (μ). The magnetic moment of a particle is sometimes called a *spin* or, if there are multiple, *spins*. The classical view of the proton is that of an electrical charge experiencing constant angular momentum (i.e. a spinning charge) which then gives rise to the magnetic dipole moment and corresponding magnetic field. This magnetic moment bears many similarities with that of a compass needle, for example, it has a direction with a north and south pole. It turns out that one can gain some intuition about the MRI signal by using the compass as a proxy for the proton.

If a compass needle (Figure 3A) is placed in an external magnetic field, like the earth's magnetic field, it will experience torque, start to oscillate, and eventually align itself with the external field (Figure 3B). The needle can be made to oscillate again by moving a bar magnet in its vicinity, creating a time-varying magnetic field (Figure 3B). If the rate of change (frequency) of this magic field matches the *natural frequency* of the compass needle, its oscillations will be the largest and the system will be in so-called *magnetic resonance*.

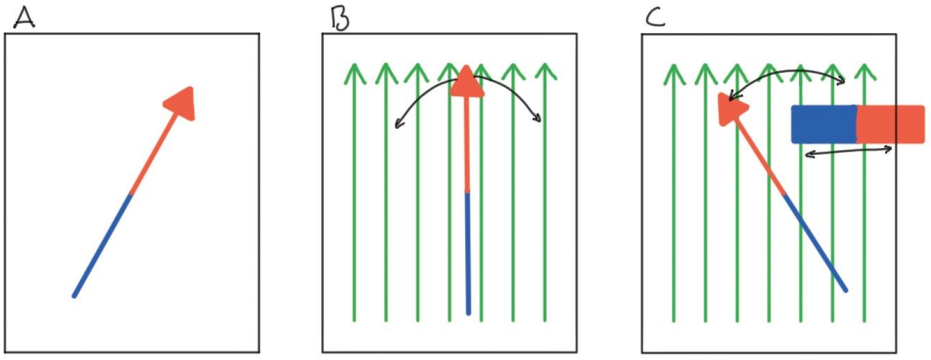

Figure 3. (A) *A compass needle;* ***(B)*** *an oscillating compass needle, coming to rest in an external magnetic field; and* ***(C)*** *a moving bar magnet makes the needle oscillate again.*

The moving bar magnet can be replaced by a coil with a time-varying current running through it, creating an equivalent time-varying magnetic field (Figure 4A). If the current is turned off, the needle will continue to oscillate for a short time period. While it oscillates it will create its own time-varying magnetic field which, in turn, will induce a measurable current in the coil (Figure 4B).

If a proton is placed in an external magnetic field, such as when a person enters an MRI scanner, it will behave very similarly to the compass needle. It will also start to oscillate, but in a three-dimensional motion known as precession (Figure 5B). Precession is a type of motion usually illustrated with a tilting spinning top slowly drawing a circle with its tip. The rate, or frequency, of precession (ω) of the proton (i.e., how fast the spinning top would draw one circle) can be calculated using the Larmor equation:

$$\omega = \gamma B_0 \qquad [1]$$

where ω is in MHz and B_0 is the strength of the external magnetic field in Tesla (T). The gyromagnetic ratio (γ) is 42.58 MHz/T for the hydrogen proton.

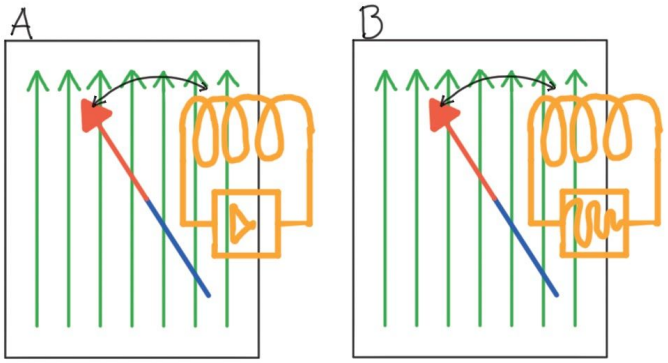

Figure 4. (A) *A varying current running through a coil creates a varying magnetic field that makes the compass needle oscillate.* ***(B)*** *When the current is turned off, the oscillating needle induces a current in the coil.*

While the compass needle eventually comes to rest, the hydrogen protons in the body are constantly disturbed by the effects of molecular motion, randomly and magnetically interacting with each other and other molecules (Figure 5C). The magnetic moments, or spins, in a sample of tissue will be randomly distributed outside of B_0. However, when placed in B_0 (i.e., when entered into the MRI scanner) their interactions will have a slight tendency to align the spins with the external field, slightly skewing the distribution in the direction of B_0 (Figure 5D). This effect, when spins go from any orientation to a so-called equilibrium state, is called T1 relaxation. When all magnetic moment vectors are added together in the equilibrium state, most of them are cancelled out. However, the slight skewness gives the sample a net magnetization vector, M, with a maximum initial value of M_0, which is what is measured by an MRI scanner.

According to convention, the spins are placed in a coordinate system (x´, y´, z), where z is in the direction of B_0. To make things easier, a rotating coordinate system is also defined (x, y, z), where the xy-plane (also called the transverse plane) rotates with the spins at the Larmor frequency. In this coordinate system, M can have components in each direction: M_z, M_x and M_y. The sum of M_x and M_y is denoted as M_{xy}.

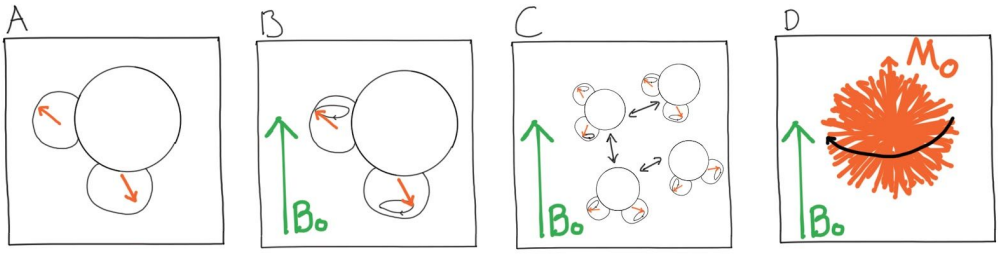

Figure 5. (A) *A water molecule with two hydrogen atoms and two spins of the hydrogen protons in orange.* ***(B)*** *When the water molecule is placed in an external magnetic field (B_0) the spins start to precess.* ***(C)*** *Due to molecular interactions, the spins continuously reorient themselves with a slight tendency towards the direction of B_0.* ***(D)*** *If all vectors of a voxel, representing the magnetic moments of spins, of a voxel are placed on the same origin they will form an almost random 3D distribution. However, the spins' tendency to align toward B_0 creates a small net magnetization (M_0) in the same direction.*

In order to measure M, it requires a component perpendicular to B_0, in the xy-plane. This can be achieved with the same principle as with the compass needle. A time-varying magnetic field, generated by a coil, at the correct frequency will resonate with the spins, effectively rotating their orientations. The same way B_0 exerts a torque on the spins, another magnetic field (B_1) applied perpendicular to B_0 can exert torque and rotate the spins. The torque is only effective, however, if B_1 rotates with the same frequency as the spins (i.e., the resonance condition is met). Consequently, this frequency can be calculated with the Larmor equation (Eq. [1]). B_1 can be much weaker than B_0 as long as it is in resonance with the spins. After some time the whole spin distribution is rotated around B_1, and M now has a component perpendicular to B_0 (Figure 6). The rotation of the spins away from their equilibrium position, into the xy-plane, is called *excitation* and the angle between z and M is called the *flip angle* (FA).

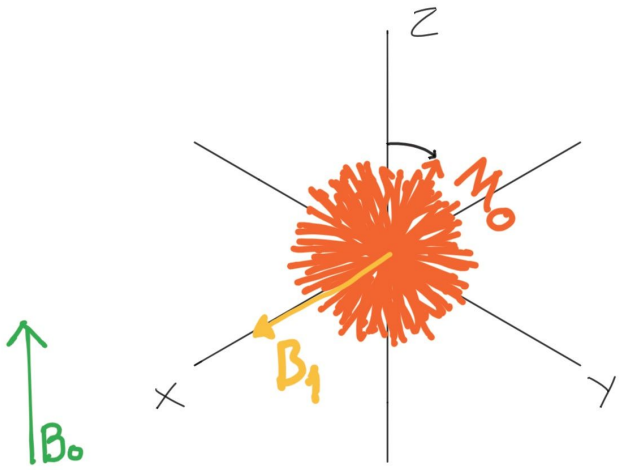

Figure 6. *When B_1 is applied perpendicular to B_0, the net magnetization is tipped away from the longitudinal axis.*

When the B_1 field interacts with the body, it does not only interact with the spins around the Larmour frequency; in fact, most of its energy results in the heating of the tissue. The MRI machine limits its RF energy output to avoid any dangerous tissue heating. The amount of heating is typically characterized by the specific absorption rate (SAR). SAR is an estimate of how much energy has been absorbed over time and it is proportional to the square of B_1 and B_0, and the bandwidth of B_1 (7).

To summarize, the signal measured with an MRI machine comes from the magnetic moments (spins) of protons in the hydrogen atom. In order for it to be measured, a net magnetization (M) has to be created using a strong external magnetic field (B_0) and the T1 relaxation effect. This magnetization then has to be excited from its equilibrium state, pointing along the direction of the B_0 field (the z-direction), into the transversal xy-plane. Excitation can be produced by inducing a weak magnetic field (B_1) rotating with the same frequency as the spins, or in other words, putting the system in magnetic resonance.

3.1.3 The small tip angle approximation

Application of B_1 in MR is typically pulsed (i.e., the B_1 field is turned on and off many times during an image acquisition). Consequently, the relatively short period when the B_1 field is turned on is called an RF pulse. During an RF pulse B_1 can change amplitude and direction (i.e., phase). The change in amplitude is

sometimes called the envelope of the RF pulse. A lot of the work in this thesis revolves around the shape of this envelope and how it affects the MR images.

The frequency response of any RF pulse can be determined, as most MR phenomena, by solving the Bloch equations (5). Here, frequency response refers to how a range of frequencies are affected by the RF pulse, in other words, at which frequencies resonance occurs and what FA is achieved at these frequencies.

To gain an intuitive understanding of what will be the result of an RF pulse the so-called *small tip angle approximation* can be used (8). The small tip angle approximation is a simplification of the Bloch equations, neglecting T1 and T2 relaxation, based on the assumption that regardless of the FA applied, M_z is left almost unchanged. For example, if an RF pulse creates a FA of α, it rotates some of M_z into the M_{xy} plane, leaving $M_z = \cos(\alpha)M_0$ and producing $M_{xy} = \sin(\alpha)M_0$. However, with the small tip angle approximation, M_z is always approximately equal to M_0 and M_{xy} is equal to αM_0.

The Bloch equations are nonlinear. Linear systems are typically characterized by the superposition principle. For the Bloch equations to be linear, the resulting M_{xy} magnetization of two RF pulses with FAs a1 and a2 would be the same as the resulting M_{xy} magnetization of one RF pulse with the FA of a3 = a1 + a2. This is not the case; for example, the response to a 180° pulse is not the same as the sum of the responses to a 39° and a 141° pulse and this is reflected in the non-linearity of the Bloch equations. However, the response to a 3° is almost the same as the sum of the responses to a 1° and a 2° pulse. Which is why the small tip angle approximation works. The solution to the Bloch equations that the approximation provides is linear. This enables the use of linear methods to analyse the system. More specifically, it enables a Fourier relationship between an RF pulse's frequency response and its envelope. This means that the frequency response of an RF pulse is approximately its Fourier transform and that all the properties of Fourier transforms can be applied to analyze an RF pulse. For example, it is now clear that a sinc (sine cardinal function) shaped RF pulse will have a rectangular frequency response since the Fourier transform of a sinc function is a rect (rectangle function). The small tip angle approximation is surprisingly accurate at predicting the frequency response of RF pulses of FAs up to almost 90°. However, when 90° is exceeded the approximation is less accurate.

The small tip angle approximation has been developed into the concept of excitation k-space (9), based on the same principles as the k-space of an MR image (10,11). In k-space the encoding gradients draw a trajectory and the received signal is placed along this trajectory. In excitation k-space the gradients associated with

the RF pulse draw the trajectories and they are weighted by the RF pulse. The frequency response is then the Fourier transform of the excitation k-space.

The concept of excitation k-space is demonstrated in Figure 7 with a simple slice selective RF pulse. In Figure 7B the excitation k-space is shown, where the gradients of Figure 7A move along the k_z plane, which has the units of 1/cm. Consequently, the 1D inverse Fourier transform of the excitation k-space is shown in Figure 7C.

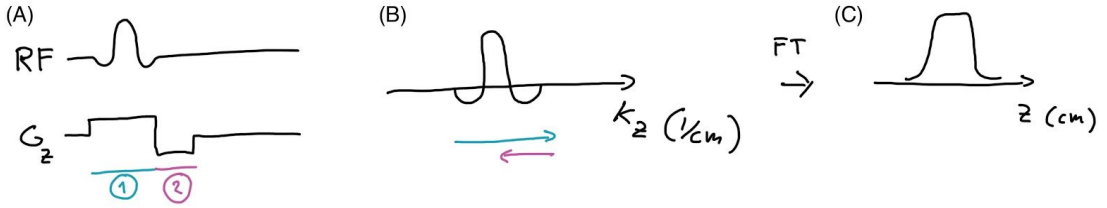

Figure 7. (A) *A slice selective RF pulse and gradient combination (1), with a rephasing gradient (2);* ***(B)*** *the excitation k-space of* ***(A)****; and* ***(C)*** *the Fourier transform of* ***(B)****, resulting in the slice profile of* ***(A)*** *as predicted by the small tip-angle approximation.*

This example might seem trivial; however, excitation k-space can also be used to analyze more complicated trajectories such as the one in Figure 8, where a spiral gradient trajectory weighted by a skewed RF pulse creates a gaussian shaped *mound* in excitation k-space, which then excites a rod shape. This type of 2D RF pulse can be used for inner volume imaging, where only the anatomy of interest is excited (12,13).

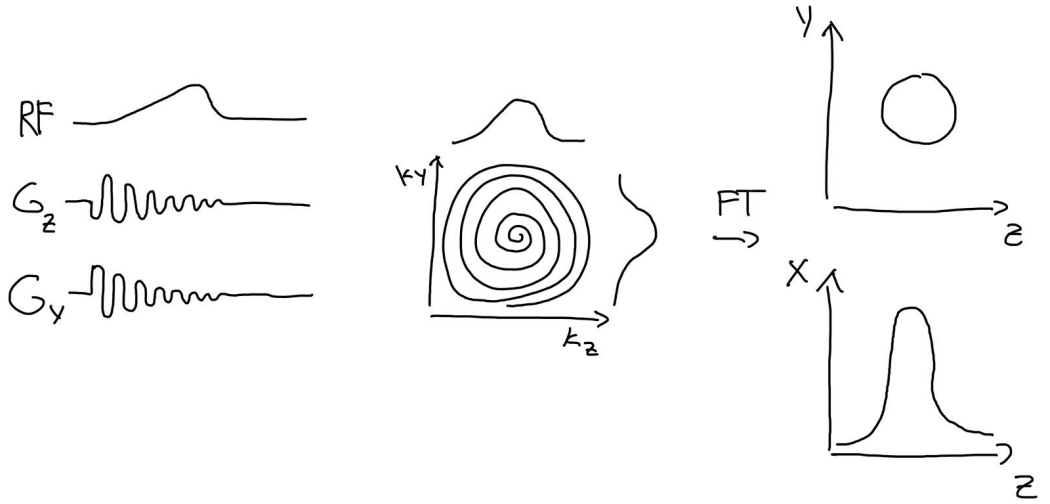

Figure 8. *An 2D selective pulse with a spiral trajectory and its excitation k-space analysis.*

Thus, the small tip angle approximation, together with the excitation k-space concept, is a powerful tool for designing low FA pulses, but, more importantly, it lends a more intuitive sense of what to expect from an RF pulse and how a specific frequency response could be achieved.

3.1.5 Higher flip angles

As mentioned in the previous section, the small tip angle approximation breaks down around an FA of 90°. However, many RF pulses are of course of higher FAs and must use other design methods. To predict the frequency response of an RF pulse using the Bloch equations is actually straight forward. It is the inverse problem that poses the biggest problem; to design a specific frequency response and then calculate the RF pulse that can produce it. The most prevalent solution to solve the inverse problem is the Shinnar–Le Roux (SLR) transform that was independently proposed by Shinnar (14,15) and Le Roux (16). The SLR transform provides an analytical inversion of the Bloch equations. This solution is then used to get to a space where a digital filter design algorithm, such as the finite impulse response (FIR), can be used to design the wanted frequency response. By using different types of FIR filters a range of RF pulses with different characteristics can be generated with the SLR transform (17).

3.1.4 Spectrally selective RF pulses

Water and fat in tissues are the largest sources of signal in MRI. Fat molecules are long chains of triglyceride. They have a much larger electron cloud that shields the hydrogen atoms from the B_0 field. Therefore, according to the Larmor equation, the spins in fat molecules have a lower Larmor frequency. The difference in frequency between water and fat is called *chemical shift*. In some cases, the signal from fat itself or together with chemical shift causes problems or artifacts that can make the images difficult for the radiologist to interpret. Thus, there exists many different ways of suppressing the fat signal. The following section provides a short account of a few of those methods.

Fat saturation

A common tactic to reduce the signal of fat is to use a so-called CHESS (Chemical Shift Selective) method (18), also known as fat saturation (fat-sat), where an RF

pulse with a narrow frequency response and an FA of 90° is aimed at the fat peak, effectively exciting only fat. This pulse is closely followed by a spoiler gradient that dephases all of the signal in the transverse plane. After this preparation a regular excitation pulse can be used to excite the untouched water peak and create an image where the signal from fat is suppressed.

Binomial pulses

A binomial pulse can be used to excite water or fat; however, they are most commonly used to excite only water to achieve fat suppression. They are composite pulses made up of multiple sub-pulses with different FAs (19). The specific sub-pulse FAs are determined by rows in Pascal's triangle (20) and sum up to the desired FA of the pulse. A binomial pulse's frequency response is a repeated pattern of pass- and stopbands, and the frequency range between pass-band peaks is a function of the time between sub-pulses. Increasing the number of sub-pulses widens the stopband and narrows the pass-band.

The duration between sub-pulses (τ_{bino}) is calculated with the following equation:

$$\tau_{bino} = \frac{1}{2|\Delta\omega|} \quad [2]$$

where $\Delta\omega$ is the frequency offset between fat and water, where the main fat peak is at -3.3 ppm from the water peak (21). At 3 T $|\Delta\omega|$ becomes approximately 422 Hz and the duration is consequently 1,18 ms.

An example of a binomial pulse is displayed in Figure 9. In this case it has two sub-pulses with the same area but with opposite polarities. It is therefore called a binomial $1\text{–}\bar{1}$ pulse. The numbers describe the relative sub-pulse areas and the line above the second number signifies that it has an opposite polarity. How this pulse can excite only water is schematically described in Figure 9. The first sub-pulse excites both water and fat to 45°. The second 45° sub-pulse is applied when water and fat are exactly 180° out-of-phase. This brings the fat back to the longitudinal axis while the water is excited all the way down to the transverse plane, at a 90° FA.

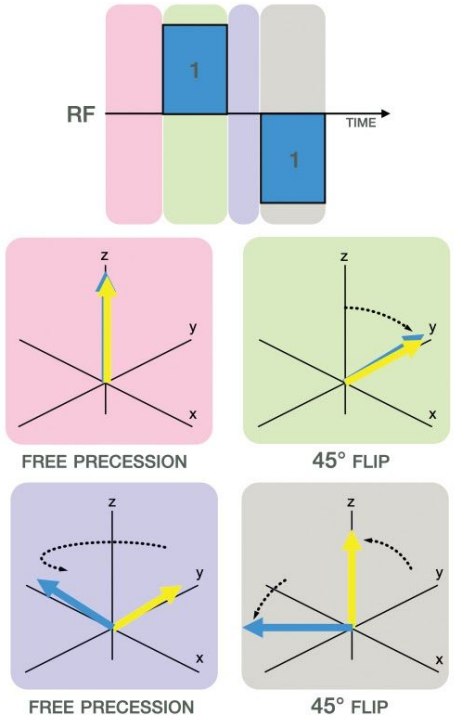

Figure 9. At the top: *a schematic binomial pulse with color coded time periods.* ***Pink period:*** *Before the pulse water (blue arrow) and fat (yellow arrow) precess around* B_o. ***Green period:*** *The first sub-pulse flips both water and fat to 45°.* ***Lilac period:*** *Water and fat precedes at different rates, eventually ending up completely opposite of each other.* ***Gray period:*** *Here the second 45° sub-pulse flips the fat back along the longitudinal axis, while water is flipped all the way down to the transverse plane.*

A rectangular pulse

Another way to excite only water or fat is the water exciting rectangular pulse (WE-rect) (22–24). It is a box-car (25) shaped pulse with a specific duration such that one of the roots of its sinc-shaped frequency response matches the difference in frequency between the water and fat peaks (i.e, $\Delta\omega$). The carrier frequency can then be changed to either excite either water or fat. The duration (τ_{rect}) of the pulse, which produces this specific sinc response, is calculated using the following equation:

$$\tau_{rect} = \frac{\sqrt{(2\pi n)^2 - \alpha^2}}{2\pi\,|\Delta\omega|} \qquad [3]$$

where α is the FA in radians and *n* specifies the zero-crossing that should match Δω.

At the resonance frequency a constant RF pulse, such as the WE-rect, simply rotates the spins around the axis to which it is applied (Figure 10A). At an off-resonance frequency, the spins experience both B_1 and a residual of B_0, which can be calculated using the Larmor equation. Together these fields create the B_{eff} field, the effective B field. The off-resonance spins therefore rotate around B_{eff} (see Figure 10B). The spins that complete a full circle at the end of the pulse remain unexcited (i.e, a zero-crossing). The number of cycles in this circle then corresponds to *n* in Eq. [3].

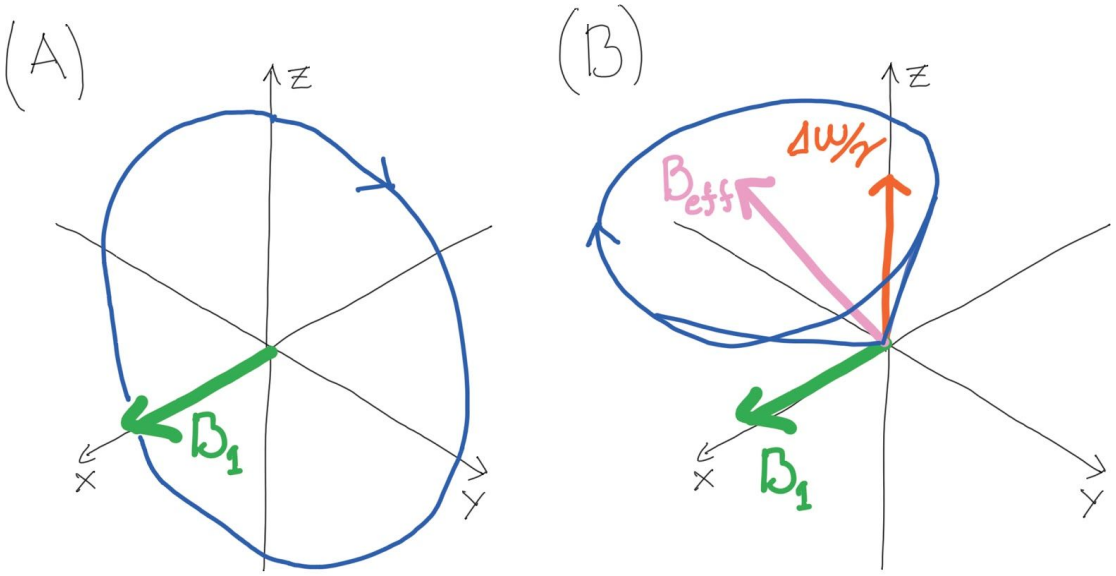

Figure 10. (A) *At resonance spins are flipped in a circle perpendicular to the applied B_1 field.* ***(B)*** *However, at off-resonance the spins two magnetic fields B_1 and a residual of B_0: Δω/γ, making the spins move in a circle perpendicular to the combination of these two fields B_{eff}.*

The WE-rect has a similar on-resonance frequency response as a binomial 1-1 pulse (i.e, they have comparable fat/water selectivity). However, it does not have the repeating pattern of the binomial pulse in the off-resonance regions, which leads to reduced off-resonance excitations and therefore reduced MT effects (26). The WE-rect also produces significantly low SAR values compared to a binomial 1-1 pulse.

Phase-modulated pulses

Two other WE pulses with similar properties compared to the WE-rect, are the BORR (Binomial Off-Resonant Rectangular) (27) and LIBRE (Lipid Insensitive Binomial Off-Resonant RF Excitation) (28) pulses. They also produce low SAR and reduced off-resonance excitations. Both pulses are applied at off-resonance (i.e, their carrier frequency is not the Larmour frequency). They are made up of two sub-pulses, with the same area, that are played back-to-back with a phase offset between them. For the BORR pulse this phase is always 180°, however, for the LIBRE pulse, it depends on the carrier frequency. A search or optimization has to be performed to find a proper combination of sub-pulse duration and carrier frequency. Regardless, the LIBRE pulses always produce a lower than intended FA at the center frequency; it therefore has to be scaled up to achieve the correct FA. The BORR pulse, however, can be designed in such a way that it achieves its peak amplitude at the center frequency. Examples of both pulses compared with the WE-rect and two binomial pulses are shown in Figure 11.

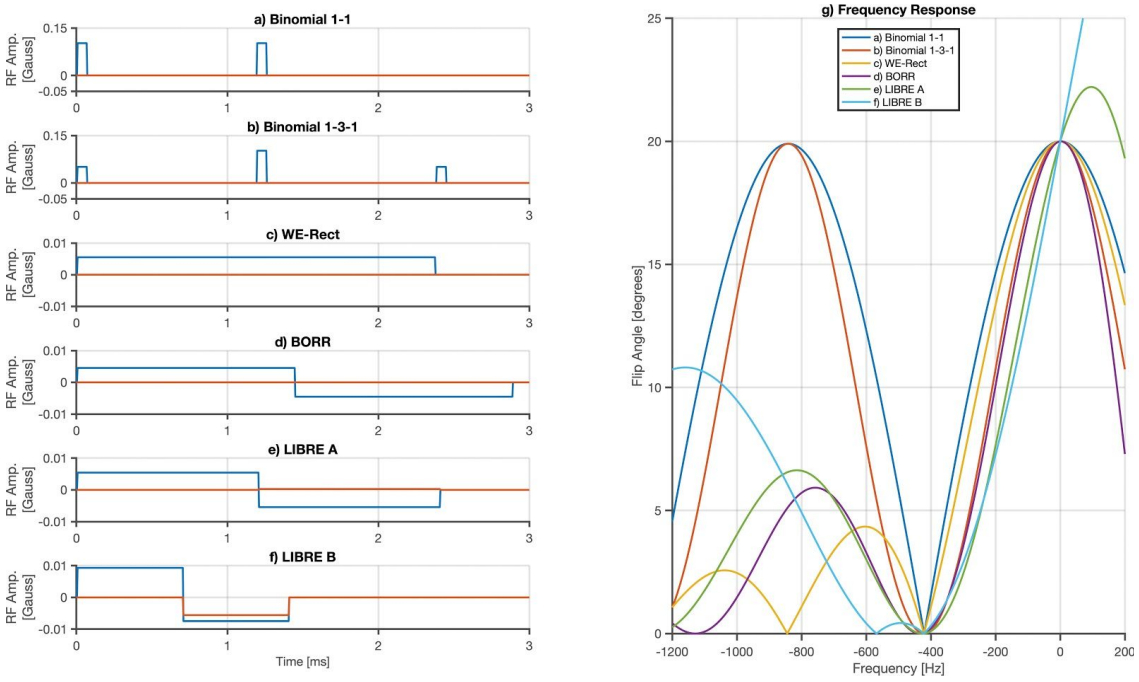

Figure 11. (a–f) *shows a range of spectrally selective RF pulses described in this section and* ***(g)*** *shows their corresponding frequency responses at 3 T.*

3.1.5 Spectral and spatial selectivity

Spectral spatial (SPSP) (29) RF pulses have both spectral and spatial selectivity and can therefore be used to excite both a slice and a specific frequency band containing, for example, only water. An SPSP pulse consists of several slice selective sub-pulses with weighted amplitudes, concatenated together to form a longer pulse, as shown in Figure 12A. The shape of the sub-pulses determines the slice profile, while the overall envelope, shown in cyan in Figure 12A, controls the spectral selectivity, similar to binomial pulses. Figure 12B and C show the excitation k-space interpretation of an SPSP pulse, where the repeating pattern of the frequency selectivity can be appreciated. This pattern can be explained by looking at the excitation k-space of Figure 12B. Any vertical line in excitation k-space consists of three points along the cyan envelope. Each line can be thought of as the envelope multiplied with a series of three Dirac's delta functions, or a Dirac-comb. If an RF pulse envelope is multiplied with a Dirac-comb, its frequency response is convolved with the Fourier transform of the Dirac-comb, which is another Dirac-comb. This creates multiples of the original frequency response.

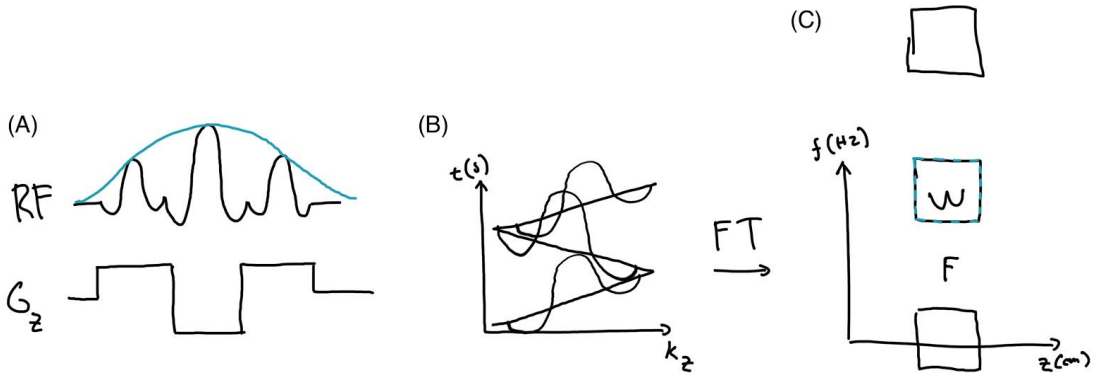

Figure 12. (A) *A SPSP pulse with three sub-pulses. The overall envelope is drawn in cyan;* ***(B)*** *The corresponding excitation k-space; and* ***(C)*** *the Fourier transform of* ***(B)*** *showing the spectrally and spatially selective features of the SPSP pulse.*

Both the overall envelope and the sub-pulse envelopes can be designed using the SLR transform. For example, a minimum-phase Parks-McClellan optimal equiripple FIR filter can be used to design both envelopes. This creates a SPSP pulse that can facilitate a low TE and be used in a slab selective manner, as shown in Figure 13.

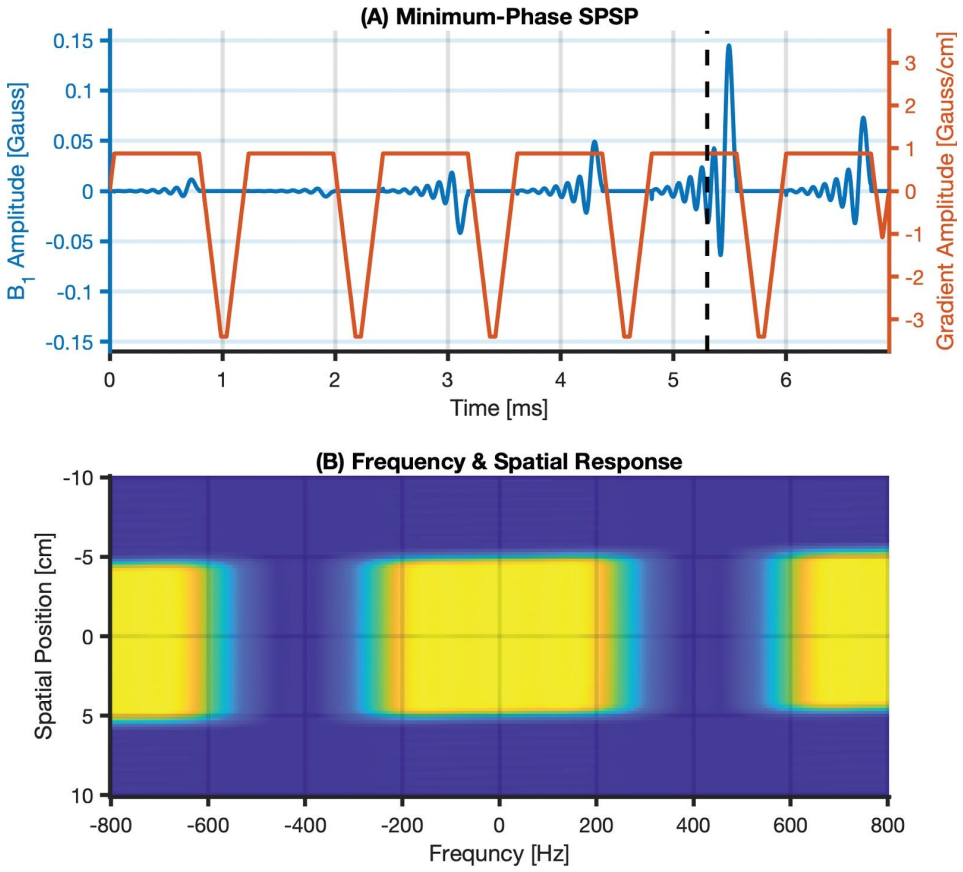

Figure 13. (A) *An SPSP pulse with both a minimum-phase envelope and minimum-phase sub-pulse envelopes. The black line marks the iso-center of the pulse, where the echo time starts.* ***(B)*** *A Bloch simulation of the SPSP pulse, showing its slab selective nature.*

3.1.6 Refocusing flip angles and extended phase graphs

To model the signal response of an arbitrary MRI sequence, the Bloch equations must be solved for each step. However, to accurately predict the effect of, for example, dephasing within a voxel, countless spins must be included in the calculation. To include this many spins in the calculations quickly becomes cumbersome. It turns out that the spins can be interpreted as a Fourier series if the gradients are assumed to be quantized and induce an integer number of phase cycles ($2\pi n$) across a voxel. As a result, the whole ensemble of spins can be represented by the coefficients in three Fourier series describing M_x, M_y and M_z. This is a much more compact way to represent many spins and the basis of the extended phase graphs (EPG) concept (30). EPG simulations are a powerful tool that can be used to predict the behaviour of many sequences, perhaps most notably bSSFP (Balanced Steady-State Free Precession) (30–32) and RARE (Rapid

Acquisition with Relaxation Enhancement) (33). In RARE sequences, the CPMG (Carr-Purcell-Meiboom-Gill) (34,35) condition makes it possible to use much lower refocusing FAs than 180°. Moreover, the EPG concept is useful for modeling the signal response of such a refocusing FA scheme.

Generally, refocusing pulses do three things: excite, refocus and restore/recall – how much of each depends mostly on the FA (36). *Restore* refers to the effect where transverse magnetization is flipped back to the longitudinal axis to be *stored,* and *recall* refers to the stored magnetization being flipped back down to the transverse plane. Tracking the spins' paths to form a signal creates so-called echo pathways in an EPG simulation. For example, spins restored by a refocusing pulse can be mixed in again at a later stage creating a *stimulated echo (37)*. The related signal evolution then comprises both spin echoes and stimulated echoes.

The stored magnetization of a soon-to-be stimulated echo decays only according to T1 relaxation contrary to the magnetization in the transverse plane, which is also subject also to T2 decay. A fraction of the magnetization contributing to the signal will, therefore, have a reduced T2 effect, thereby slowing down, or in some cases counteracting, the otherwise exponential T2 decay of the signal. This way one can, to some degree, control the signal evolution by combining high and low FAs .

Variable refocusing FA (VRFA) schemes have been used for a number of different applications. For example, the TRAPS (Smooth Transitions between Pseudo Steady States) method has been used to reduce the SAR of several different RARE sequences and contrasts (38–43). VRFA has also been used to extend the life of the signal during the very long echo trains of T2-weighted 3D RARE (44). Another notable use of VRFA is the reduction of blurring and contrast enchantment of T1-weighted 3D RARE (45), where the signal is kept constant near the center of k-space to reduce blurring from the T2 decay.

3.1.7 The transfer of magnetization

Hydrogen in the non-fatty tissues of the body reside in three so-called pools; the macromolecular, the bound, and the free water pool (46). The macromolecular pool are hydrogen atoms that are part of large molecules like proteins. The bound pool are water molecules that are closely associated with the macromolecules. Usually the expression *bound pool* also includes the macromolecular pool. The free pool consists of unrestricted rapidly tumbling water molecules. The free pool can

be used for imaging since its high tumbling rate causes long T2 relaxation. An excited bound pool, on the other hand, decays very quickly.

If the free pool is excited by an RF pulse it can transfer some of its magnetization to the bound pool, via dipole-dipole and chemical exchange interactions. This process is called MT. However, if the bound pool is excited, it can transfer magentzation to the free pool to cause signal attenuation as the free pool becomes saturated. This can be exploited for background suppression (47) and detection of myelin diseases (48).

The bound pool has a wide frequency range, due to its short T2, and can therefore be excited by off-resonance RF pulses. In regular imaging, most RF pulses excite the bound pool to some degree, leading to signal attenuation (49). The MT effects are also presumed to saturate the signal of white matter more than gray and therefore effectively reduce the GM/WM contrast in T1-weighted imaging (50).

3.2 Acceleration using Simultaneous Multi-Slice

One of the remaining drawbacks of MRI is that it is inherently slow, since physiological properties, such as relaxation times, tissue heating, and nerve stimulation, all limit the speed at which images can be acquired. Therefore, a significant amount of research is being undertaken to try and find new ways to get around these issues and thereby accelerate the image acquisition. One recent breakthrough is the SMS technique (51). With SMS, increased speed is accomplished by exciting and collecting information from several slices at the same time, unlike conventional 2D imaging where only one slice is imaged at a time.

The time gained when accelerating an acquisition with SMS comes from the ability to fit more slices into one TR or the consequent shortening of the TR (Figure 14b). An alternative use of SMS is to increase the number of slices to obtain the original TR (Figure 14c). These two options, can of course, be combined to acquire an increased number of slices in a slightly shorter amount of time.

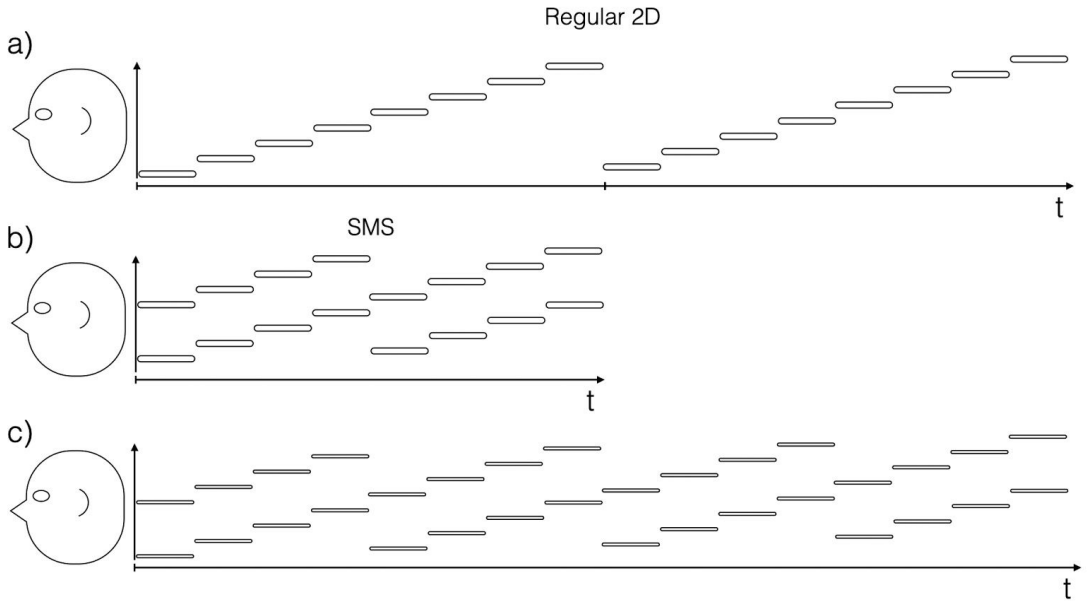

Figure 14. (a) *A regular 2D acquisition showing which slice positions are being acquired at time point. The positions are interleaved.* ***(b)*** *With an SMS acceleration factor of two, the acquisition time can be halved.* ***(c)*** *Alternatively the number of slices can be doubled.*

SMS accelerated imaging also has a significant SNR benefit over in-plane acceleration. In-plane acceleration effectively reduces the time spent receiving the signal, which incurs an intrinsic $\sqrt{R}$ SNR penalty. In contrast, SMS acceleration

records signal from protons of multiple slice positions without having to shorten the time spent listening to the signal.

Most of the papers being published on using SMS techniques are focusing on EPI based acquisitions, such as fMRI and diffusion (52–57), but also: perfusion (58,59), angiography (60) and fingerprinting (61). Using SMS with RARE sequences to acquire regular contrasts for structural imaging, which is of special interest for this thesis, have not been adopted as rapidly. However, there are a few examples. Norris et al. (68) acquired a whole brain with 1 mm in-plane resolution and 2-mm-thick slices in 2 min. Following this development, Gagoski et al. (69) have achieved 1 mm isotropic, so-called pseudo 3D (p3D), resolution RARE in 1 minute.

3.2.1 Multiband excitation

At the base of SMS is the ability to excite more than one slice using a single RF pulse, a multiband pulse. As the name implies it is a pulse that contains multiple excitation frequency bands. This section will overview several of the techniques making this possible.

The simplest and most common way of producing a multiband pulse is by combining two or more regular RF pulses, so-called sub-pulses. For example, taking two regular sinc-shaped RF pulses, applying a phase ramp to one of them, and then adding them together will excite one slice at the center frequency and one at an offset position corresponding to the applied phase ramp (62). This method is described in Figure 15.

One of the constraints when designing an RF pulse is the maximum peak power that the MR-system can put out; it is generally around 0.25 Gauss. Considering the typical shape of an RF pulse, with a peak lobe in the middle, a multiband pulse generated by addition will quickly reach the maximum allowed amplitude. There are a number of strategies to avoid this problem, several of which are outlined below.

The first strategy shifts the underlying pulses with respect to each other in time, so-called time-shifting (63). This puts additional limits on the slice selective gradients as they need to account for the difference in phase accumulation of the shifted underlying pulses.

Variable rate selective excitation (VERSE) (64) can also be used to reduce the peak amplitude of the multiband pulses. With VERSE, the bandwidth of the RF pulse is changed during the pulse. The amplitude of the peak can therefore be lowered if the gradient is lowered as well, to keep the slice profile intact. This is one of the more prevalent approaches; however, off-resonance spins can skew the slice profile.

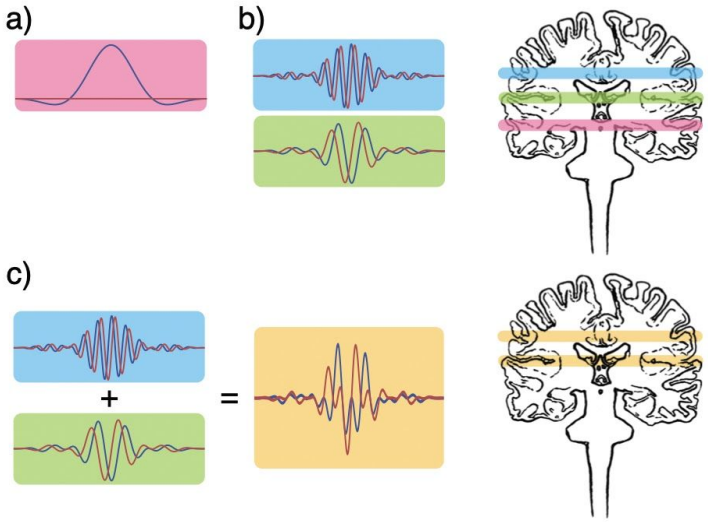

Figure *15.* ***(a)*** *A regular RF pulse that, together with a constant gradient, excites a slice at isocenter.* ***(b)*** *Two differently phase-modulated RF pulses, which excite two different offset slice locations.* ***(c)*** *When the pulses are summed together they form one single (multiband) pulse that excites both slice positions at the same time. The multiband pulse has double the amplitude compared to the single-band pulses.*

An extreme version of the VERSE approach can be achieved by using *optimal control* optimization (65), where the RF envelope, phase, and gradient is jointly optimized to produce a multiband pulse that lives up to certain quality criteria.

Optimized phases (66–68) use a look-up table with pre-calculated constant phase offsets for the individual sub-pulses, optimizing the destructive interference when the sub-pulses are added together.

Root-flipping (69) is a method where the shapes of the underlying pulses are optimized to destructively interfere with each other, similar to the optimized phases. The excitation pulse and the refocusing pulse needs to be jointly optimized to produce a usable phase across the slice.

A recent development in multiphoton MRI (70) has shown that a multiband adiabatic inversion pulse could be generated by simply oscillating the z-gradient

during the pulse. This is potentially very useful since it does not increase SAR for an otherwise high powered RF pulse.

One interesting way of exciting multiple slices without a large SAR increase is called PINS (power independent of number of slices) (71). PINS pulses are composite pulses, consisting of several hard pulses and are closely related to binomial pulses (used for spectral selection). One way of creating a PINS pulse is to simply multiply a regular RF pulse with a Dirac-comb. As described earlier, the multiplication will correspond to a convolution of the original RF pulse's slice profile with a Dirac-comb. The creation of a PINS pulse is depicted in Figure 16. A PINS pulse creates (in theory) endless multiples of the slice; this limits its use somewhat because the slice direction cannot be used as a cutoff for the FOV. Another downside is that PINS pulses have rather low bandwidths when compared to conventional multiband pulses, which make them more susceptible to slice profile distortions in the presence of B_0 inhomogeneities.

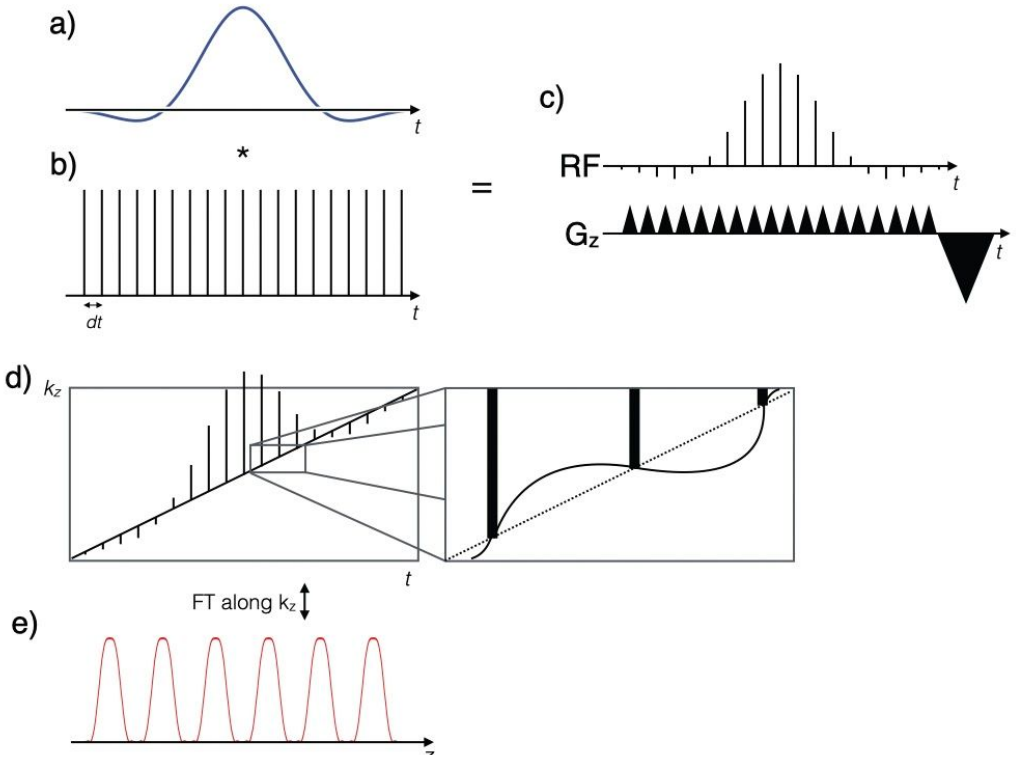

Figure *16.* *The creation of a PINS pulse* ***(c)****. When a regular RF pulse* ***(a)*** *is multiplied with a Dirac-comb* ***(b)*** *in the time domain, it corresponds to a convulsion in the frequency domain and the result is an "infinite" repetition of the original frequency response.* ***(d)*** *When gradients are placed between the sub-pulses, the k_z direction of excitation k-space is traversed.* ***(e)*** *This generates repetitions in the z-direction and multiple slices are simultaneously excited.*

An adiabatic inversion pulse can also be turned into a PINS pulse using the same principle (72). It is then called a PINS-DANTE pulse, since Delays Alternating with Nutation for Tailored Excitation (DANTE) (73) pulses, previously used for tagging, also use the same principle.

A second further development of the PINS pulse is the multi-PINS pulse (74). Here the PINS pulse is combined with a regular multiband pulse of the same duration by using VERSE to fit the multiband pulse to the gradient blips of the PINS pulse. The RF area can then be spread out and the peak power be reduced.

3.2.2 Reconstruction methods

When multiple slices are excited at the same time, signal from all slices end up overlayed in the same k-space. There are a number of different reconstruction methods to separate the slices. Most of them build on already existing theories coming from reconstruction techniques for undersampling in 1D and 2D, for example, SENSE (Sensitivity Encoding) (75) and GRAPPA (Generalized Autocalibrating Partial Parallel Acquisition) (76).

Any GRAPPA based algorithm synthesizes k-space points from a weighted combination of neighboring points. The combining of points assumes that the points in k-space are somehow related, which they are due to the use of multiple receiver coils, where each coil picks up signal from one small part of the object. k-Space is thereby convolved with the Fourier transform of the coil sensitivity, which introduces a relationship between neighboring points. This effect of the coil sensitivities make them important for the quality of the reconstruction. If the coil sensitivities are distinctly different from each other the weights corresponding to each coil will then also become more distinct, and signal from different positions can be teased apart. With SMS acceleration, the reconstruction quality will to a large degree depend on how different the coil sensitivities are between the slices.

Most SMS data reconstructions require some sort of calibration or reference data that is fully sampled in the slice direction (i.e. all the slices are imaged separately). The calibration data is then used as prior information about how the points in k-space are related at each slice position and its specific coil sensitivities.

The main artifact of SMS acceleration is residual signal from the other simultaneously excited slices, which is usually called slice-leakage. It is analogous to the residual ghosting that can appear with in-plane undersampling. The quality of a parallel imaging reconstruction can be measured using the g-factor (short for

geometry factor) (75). Each pixel has a g-factor that describes the reconstruction methods ability, with the used coil configuration, to separate aliased pixels.

The first GRAPPA based algorithm that could reconstruct SMS data is the so-called SENSE/GRAPPA hybrid (77), originally developed for accelerated 3D datasets. It artificially generates reference data in an extended FOV that contains all the slices. Using this reference, regular 1D GRAPPA weights can be estimated and used to reconstruct SMS data (as depicted in Figure 17). The SENSE/GRAPPA method is fairly simple to implement and can be used to reconstruct both in-plane undersampling and slice accelerated data in a single step (78,79).

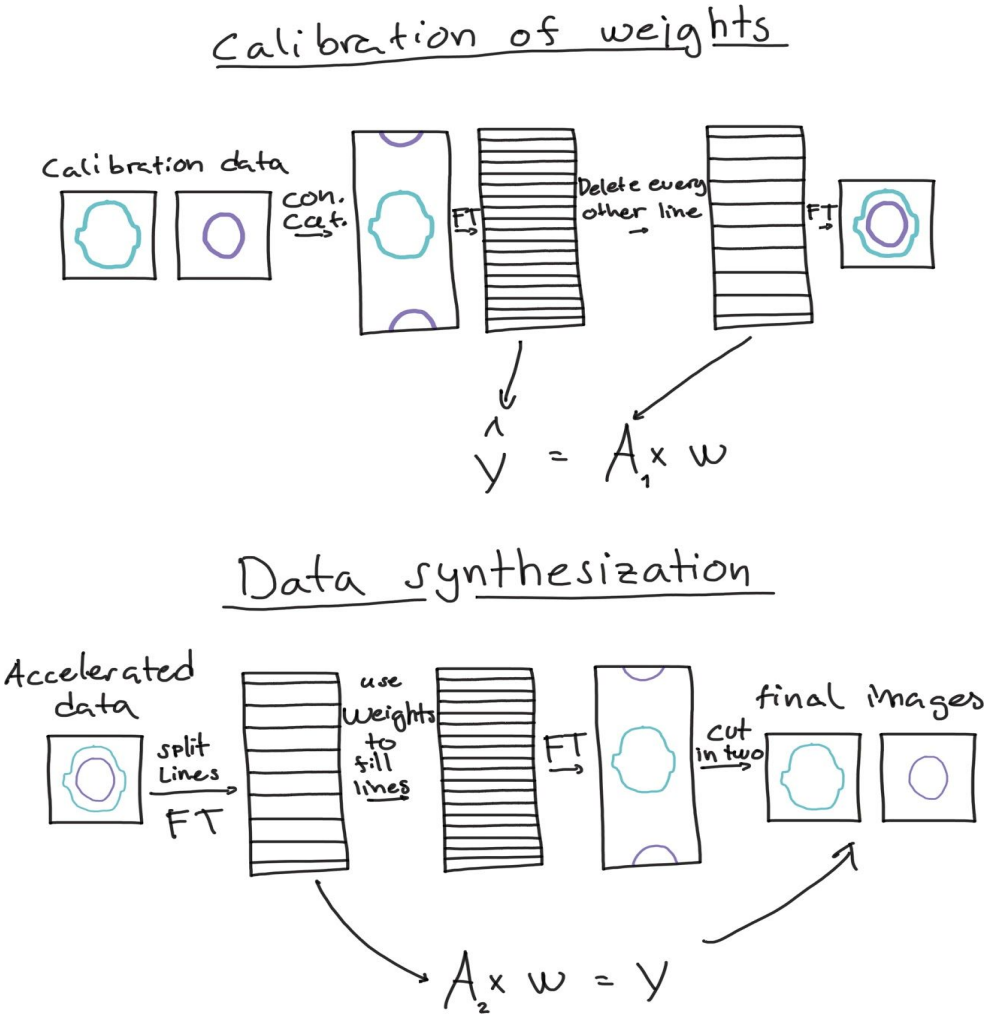

Figure 17. *SENSE/GRAPPA hybrid reconstruction. In the calibration step, the calibration data is placed in a large FOV that is used as the wanted outcome (ŷ) in the first equation. Then every other line is removed, which effectively mimics an SMS acquisition; this is used in the model matrix (A_1). From this, the GRAPPA weights can be calculated. In the data synthesization step, the acquired SMS accelerated data is split up to create gaps in k-space, which can be synthesized using the previously calculated weights. Then the resulting large FOV can be cut into the resulting separated slices.*

Another method to reconstruct SMS data is called slice-GRAPPA (80). It uses slice-specific GRAPPA weights that extracts one slice at a time from the accelerated data (shown in Figure 18). Any additional in-plane undersampling has to be reconstructed in a separate step afterward. The use of two steps adds some flexibility and each of the steps can be tailored individually to the specific needs of the application. In addition, the slice-GRAPPA has been further developed with an added constraint that aims to "block" slice-leakage, known as split-slice-GRAPPA (81).

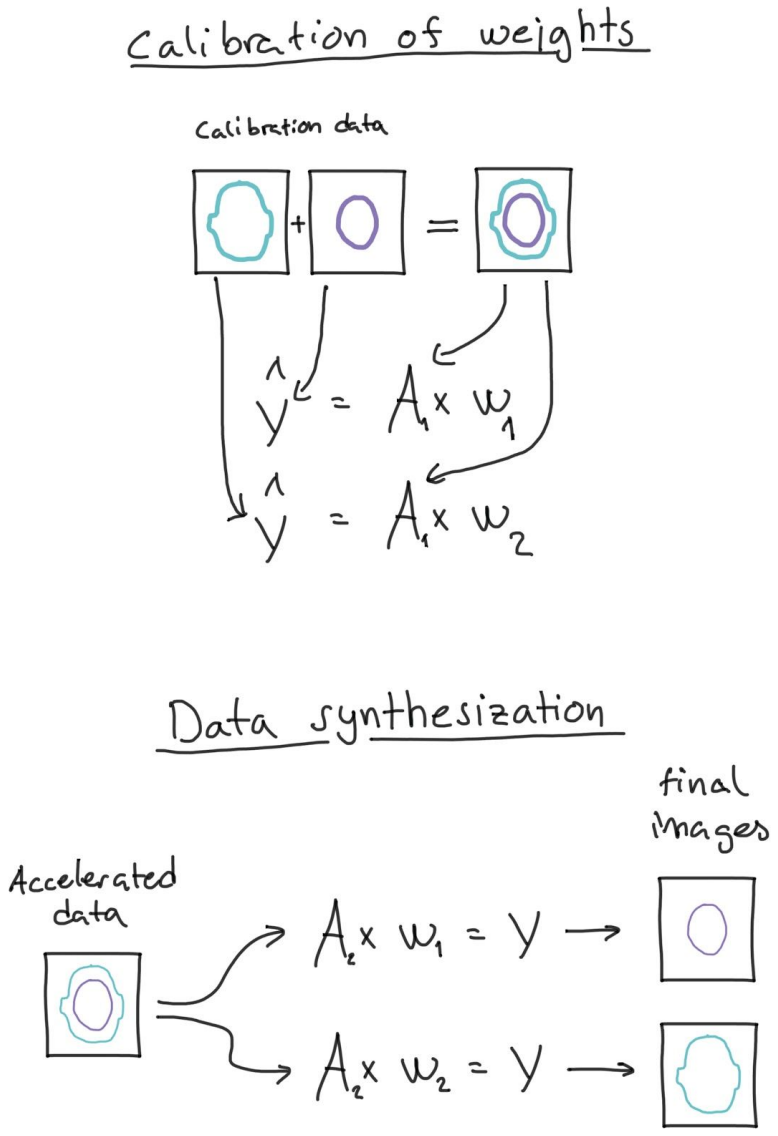

Figure 18. *The slice-GRAPPA reconstruction starts with the calibration of two sets of weights (w_1 and w_2). Using the separately acquired calibration slices, with one slice for each set of weights, as the goal ($\hat{y}$) and the sum of the slices as the model matrix (A_1). In the data synthesization step, the weights are applied to the accelerated SMS data to create entirely new synthesized k-spaces.*

3.2.3 CAIPIRINHA

The CAIPIRINHA (82) method was proposed to prevent artifacts and increase reconstruction quality. With this method, the simultaneously excited slices are deliberately shifted relative to each other in the phase-encoding direction. This effectively makes the apparent coil sensitivity profiles more unique between the superimposed slices.

According to the Fourier shift theorem (83), an object can be shifted in the FOV along the phase-encoding direction through the application of a phase ramp in k-space. For example, to shift the object half of the FOV, each line in k-space has to have a π phase difference between them. This can be achieved by creating RF pulses that result in corresponding phases and cycling through them as the phase-encoding direction of k-space is traversed (84). For multiband excitations, the individual phase cycling patterns of each slice can be achieved by modifying the underlying base RF pulses. This means that the pulse sequence designer must generate a number of different RF pulses and switch between them in real-time. The total number of multiband RF pulses necessary will depend on the number of simultaneously excited slices and the shifts between them.

Another way to realize the phase ramps needed is to insert small gradient blips in the z-direction before each readout (Figure 19). This is called blipped-CAIPIRINHA (80) and was originally invented for EPI, where it is not possible to use the original RF phase implementation. However, blipped-CAIPIRINHA is more simple to implement for most sequences; making it the most prevalent method.

One further development of the CAIPIRINHA technique is the wave-CAIPIRINHA (85), where, in addition to shifting the slices, all voxels are spread out in all three dimensions. Oscillating y and z gradients are played out during the readout, creating a corkscrew trajectory. This results in significant reconstruction quality improvements compared to conventional CAIPIRINHA at high acceleration factors, at the cost of complicated reconstruction and acquisition.

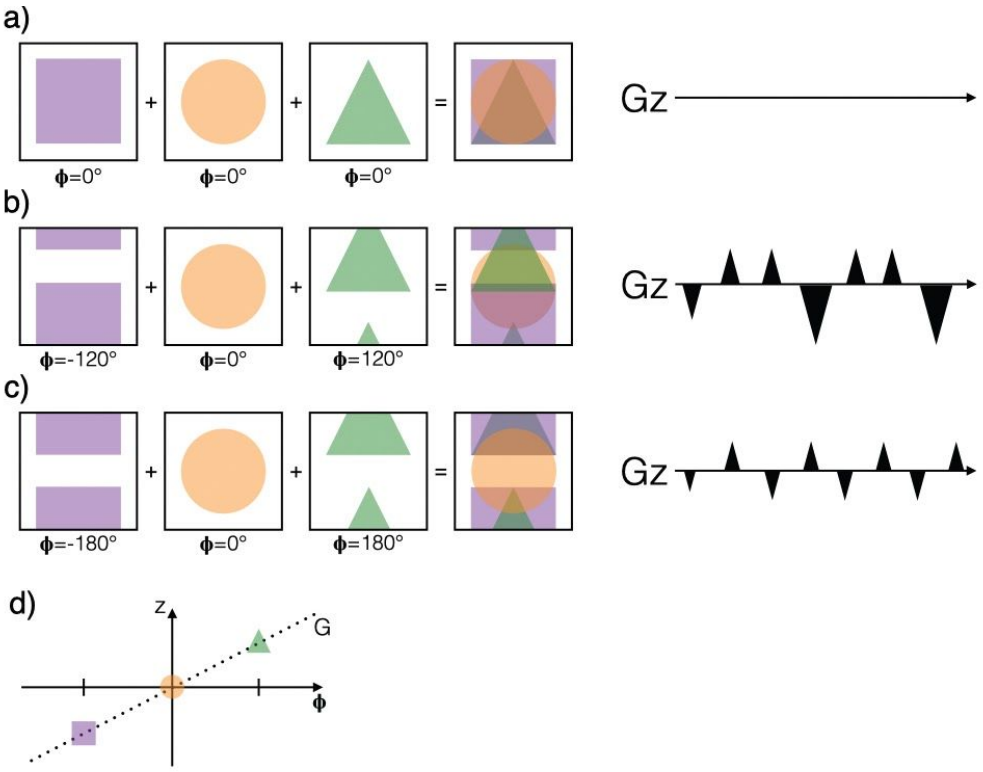

Figure *19.* *The figure shows how gradient blips can create phase ramps in k-space in order to achieve different shifts in the FOV. Φ denotes the relative phase between two k-space lines.* ***(a)*** *A standard SMS acquisition where the slices end up on top of each other.* ***(b)*** *A FOV/3 CAIPI-shifted acquisition, where the blips, displayed on the right, induce a 2π/3 phase difference between k-space lines.* ***(c)*** *A FOV/3 CAIPI-shifted acquisition. Note that the square and the triangle end up in the same position in the FOV.* ***(d)*** *Graph showing the relationship between the gradient blips applied and relative phases. The same FOV shifts can be accomplished by using RF pulses that excite slices with different phases.*

3.3 Motion Correction

3.3.1 Motion artifacts

As previously discussed, MRI is inherently slow and therefore sensitive to motion because the data is gathered over time under the assumption that the imaged object is perfectly still. When this assumption is violated, it causes inconsistencies in the data that, in turn, causes artifacts in the image. These artifacts make it more difficult for the radiologist to interpret the images. When an image is sufficiently corrupted, it needs to be re-acquired and the patient has to spend more time in the scanner, which can cause stress for both the patient and the operator of the scanner. In the worst case scenario the patient has to leave the hospital without a complete exam.

Motion can cause a range of artifacts that have very different impacts and effects depending on the sequence used. The following outlines examples of the most common issues.

In the frequency-encoding direction, data acquisition is extremely rapid, thus motion is essentially *frozen* for this time. Consequently, inconsistencies that arise in k-space due to motion occur only in the phase-encoding direction, between lines. These inconsistencies may cause ghosting or blurring. These image artifacts occur in the direction that correspond to the phase-encoding direction.

Since a rotation in image space is a rotation in k-space, rotations of the body can produce gaps in k-space that cause streaks in the image.

Another source of error, specific to 2D imaging, is a mismatch between excited, refocused, or inverted slices, the so-called spin history effects. This disrupts the contrast mechanisms and can cause inaccurate contrast and signal loss. For example, overlapping slices can result in an erroneous TR.

When a body part is moved the effect it has on the B_0 field changes and when the body's position relative to the receive and transmit coils change, the coil sensitivities and the B_1 field is affected. Depending on the sequence used, these changes can have a significant impact on the image quality. For example, susceptibility or T2* weighted imaging is particularly sensitive to changes in the B_0 field (86).

3.3.2 Retrospective and prospective motion correction

Motion artifacts can be avoided or corrected through a variety of different methods. They can be categorized into two groups: retrospective and prospective.

Retrospective motion correction (RMC) methods attempt to reorganize the data in the postprocessing step to increase consistency and minimize artifacts (see Figure 20). They are typically iterative, minimizing a measure of artifacts, such as entropy, or maximizing data consistency (87–89). Self-navigation is possible for some encoding trajectories, for example the PROPELLER (Periodically Rotated Overlapping Parallel Lines with Enhanced Reconstruction) (90) that will be discussed in detail in the next section.

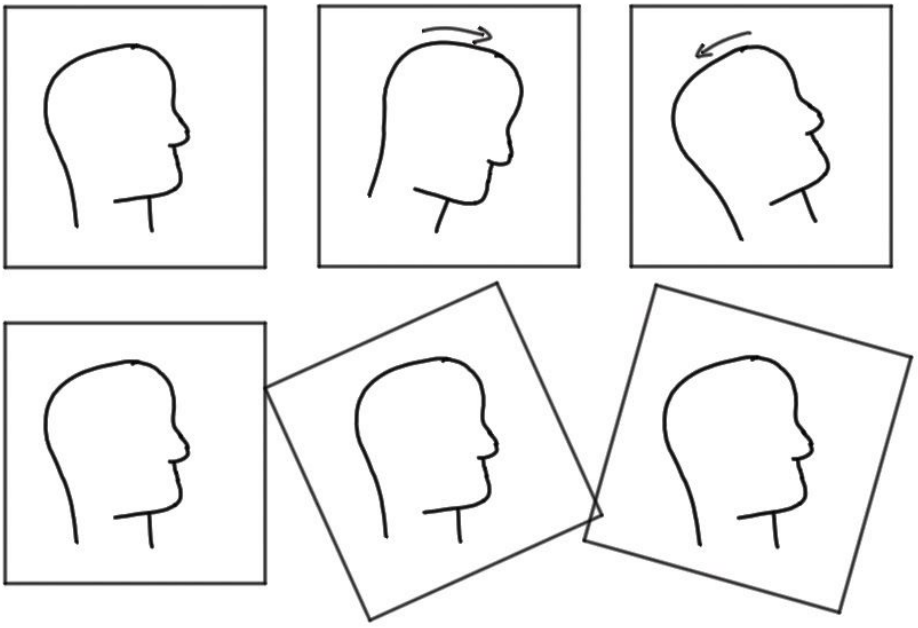

Figure 20. Top row: *Three images acquired at different time points and different head positions.* ***Bottom row:*** *The retrospectively corrected versions where the images have been rotated to accommodate the movements that occurred during the acquisition.*

Prospective motion correction (PMC) methods, on the other hand, try to compensate for motion in real-time by updating the FOV, as in Figure 21. This requires that the encoding gradients, RF transmit, and receive-frequency and -phase, are changed during the acquisition to follow any rigid body movement (91). The motion has to be traced in order to update the sequence. There are mainly two categories of correction methods: navigators and external devices.

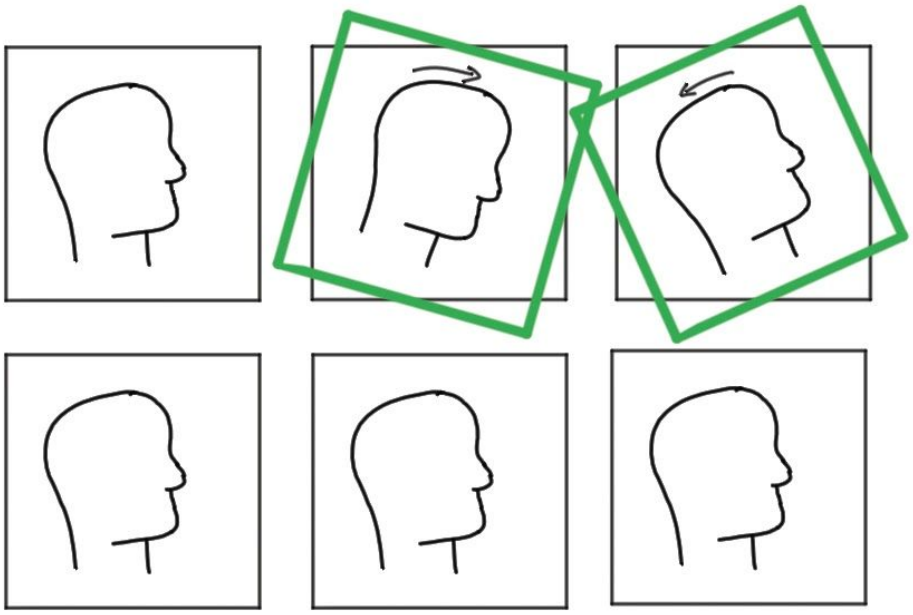

Figure 21. Top row: *Three images acquired at different time points and different head positions. The FOV is prospectively updated (in green) to keep the head in the same orientation as the first image.* ***Bottom row:*** *The final images appear as if no motion occurred.*

A navigator uses the MR-signal to obtain information about the position of th imaged object. For example, the PROMO (Prospective Motion Correction) method uses multiple orthogonal spiral read-outs to acquire a snapshot of the head in three planes (92).

The second category of PMC methods, external devices, refers to additional hardware used to track motion. Examples include; cameras tracking markers fastened to subject (93), miniature RF probes tracking field changes (94), and infrared cameras tracking facial features (95).

3.3.3 PROPELLER

One of the most widely used retrospectively motion-corrected sequences is probably the PROPELLER, first proposed by Pipe (90) and made popular by its ability to reduce motion and flow artifacts. It is a hybrid between a cartesian and a radial trajectory, whereby k-space is segmented into cartesian strips, or blades, that are rotated to fill the entire k-space, as depicted in Figure 22a. The blades then

contain images that have a full resolution in their frequency-encoding direction and a low resolution in their phase-encoding direction. By regridding all the k-space pixels, from all blades, on the same cartesian grid a full resolution image can be formed.

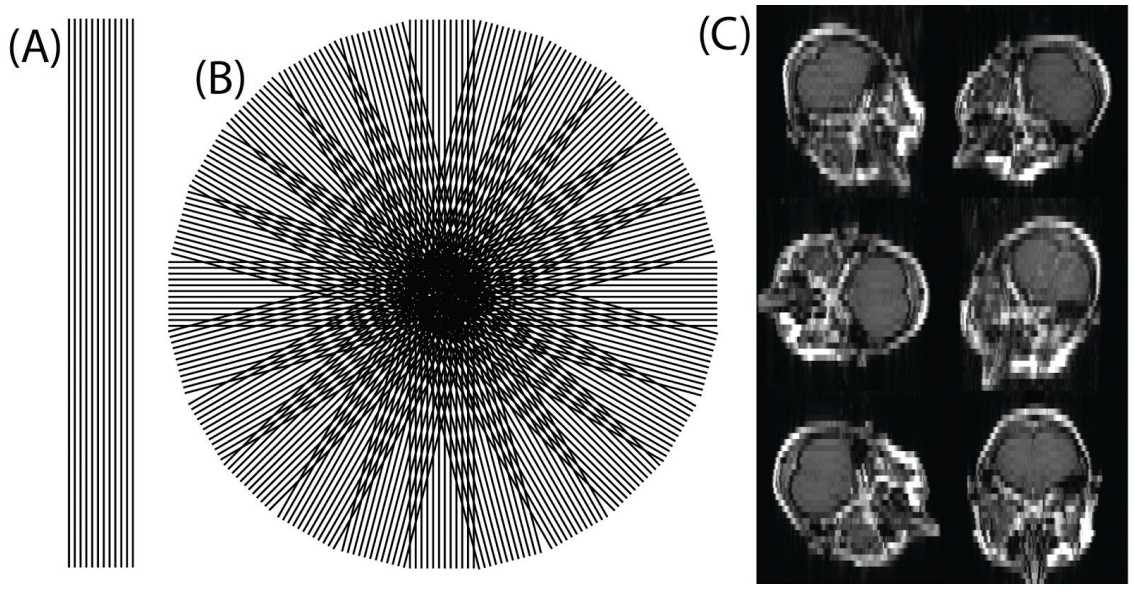

Figure 22. (A) *A PROPELLER blade in k-space.* ***(B)*** *A complete PROPELLER trajectory, consisting of 12 blades.* ***(C)*** *Example of blades in image space, which are of low resolution in their phase-encoding direction and of high resolution in their frequency-encoding direction.*

Since each blade contains the center of k-space, they can be registered to each other before the final regridding to correct for rigid body motion. In the original PROPELLER implementation, the motion between blades was found by maximizing the correlation of the central k-space region of each blade with the mean of all blades. Translations and rotations are found separately. The k-space needs to be inversely scaled so that the central region and edges of k-space have a similar amplitude. Otherwise, the k-space peak dominates the correlation measure and rotations, in particular, become harder to find.

Before the blades can be subjected to motion correction and gridding, they are phase corrected. This centers each blade exactly on the k-space origin by removing slowly varying phase ramps from image space. This is accomplished by windowing each blade, in k-space, with a pyramid-shaped filter and removing the phase of this windowed data from the blade in image space.

The main drawback of the PROPELLER is the increased scan time, compared to a cartesian acquisition, due to the repeated acquisition of the central k-space. The PROPELLER trajectory takes $\pi/2$ times longer than a conventional scan. The large difference in SNR between the central k-space and the edges of k-space represents another disadvantage. It leads to colored noise as the image noise distribution is skewed away from white (96,97). A third downside is the effect of chemical shift between fat and water. Each blade experiences a shift of the fat signal in its unique frequency-encoding direction. When the blades are combined to form the final image, the fat ends up being dispersed and blurred. This limits the PROPELLER to higher receiver bandwidths in order to mitigate this effect. If the PROPELLER is combined with a fat-water separation technique (i.e. Dixon imaging (98)), where the fat and water signals are separated for each blade, the chemical shift can be corrected (99,100). The motion correction is also affected by the fact that the blades have a uniquely shifted fat signal (100).

PROPELLER scans can be accelerated by in-plane parallel imaging methods such as GRAPPA (101). Using extra auto-calibrating signal lines (ACS lines) in the center of the undersampled blade allows each blade to be auto-calibrated. The GRAPPA weights are then determined from the center lines and can be applied to synthesize the missing lines at the edges of each blade. Given the relatively low number of k-space lines per blade, the ACS lines reduce the effective net acceleration significantly unlike regular Cartesian scans. ACS lines can, however, be avoided by using a mutual blade calibration GRAPPA technique, where pairs of orthogonal undersampled PROPELLER blades are calibrated jointly (102). The blade angles are then set up in a way that two orthogonal, or perpendicular, blades are rotated to several positions, spanning the k-space. This makes it possible for a pair of orthogonal blades to act as each other's calibration data, since they are fully sampled in each other's undersampled directions. Alternatively, an angularly continuous GRAPPA kernel could be used (103). Another option to avoid ACS lines in PROPELLER is to use an external calibration scan. This can be one fully sampled PROPELLER blade as proposed by Holmes et al. (104). Holmes et al. used such a blade as calibration for all accelerated blades with the APPEAR (Anti-aliasing Partially Parallel Encoded Acquisition Reconstruction) method (105), which utilizes interpolation in k-space.

3.3.4 The WRAD

An example of an external device used for prospective head motion tracking is the wireless radio frequency triggered acquisition device (WRAD) (106,107). It is a small apparatus that can be attached to the subject, from where it wirelessly transmits its position and orientation to the scanner.

The WRAD combines three orthogonal pickup coils that determine the rate of change of the magnetic fields in the scanner. A key feature of the WRAD is that it measures these fields as vectors and can therefore make use of an additional dimension of spatial encoding (from gradient magnetic field components perpendicular to the static magnetic field). These fields are typically not accessible to MR based methods. The interpretation of these vectors is, however, challenging because the orientation of the pickup coils with respect to the gradient coils is unknown. The WRAD solves this problem by introducing an additional sensor: a 3D hall-effect magnetometer. This magnetometer measures the direction of the static magnetic field, which has a direction that is known in the gradient frame, and can therefore be used to interpret the pickup coil voltages. By playing a navigator consisting of at least two unique sinusoidal gradients, preferably on the principal axes, the WARD can calculate both its position and orientation.

There are advantages and disadvantages for each of the PMC technologies. In a review article on prospective motion correction Maclaren et al. suggests three main criteria for an ideal PMC method (108):

- ❏ High accuracy and precision
- ❏ No patient interaction
- ❏ Sequence independence

Evaluating the WARD on Maclaren's terms for an ideal PMC method, the WRAD has very high accuracy and precision. It does, however, require patient interaction since it has to be attached to the head. When it comes to sequence independence, the WRAD requires the incorporation of navigators into the sequence. However, these navigators are short enough, below 5 ms, to be inserted into most sequences without significant disturbance.

A significant advantage of the WARD is that it requires no cross-calibration (109) procedure. Cross-calibration is a term used for finding the relationship between the device's coordinate system and the scanner's coordinate system. It is a significant

source of error for most external devices. The WRAD does not require one because it senses the same gradients fields used for image encoding to encode its pose.

4 Methodological Considerations

This chapter introduces the three projects that are the basis for this thesis and provides the motivation for several of the methodological choices made, adding extra information not included in the constituent papers, and referring back to the previous chapter. For a complete review of the methods and techniques used in these works please see the papers, which the author recommends should be read first.

4.1 Project I: SMS Accelerated PROPELLER

4.1.1 The aim of Project I

The first project's aim was to combine SMS acceleration with the PROPELLER trajectory. The hypothesis was that this novel acceleration method would unlock new degrees of freedom for the PROPELLER sequence.

4.1.2 Short summary of the work

A PROPELLER sequence with support for SMS acceleration, including multi-band RF pulses and CAIPIRINHA, was developed. Efficient acquisition of the calibration data was enabled by calibrating the PI on a single fully sampled PROPELLER blade. Consequently, the acquisition involved one fully sampled blade, and the remainder of the blades accelerated without additional lines. The SMS accelerated PROPELLER sequence was used to acquire T1-weighted, T2-weighted, and T1-FLAIR images. The SMS acceleration was also used to acquire many thin slices, creating motion-corrected reformattable image volumes.

4.1.3 Choosing the RF pulse

The multi-band RF pulses described in the background and theory chapter were evaluated to determine which method would work best for the SMS and PROPELLER combination. A method that could produce short RF pulses along with significant peak power reductions was sought after because it facilitates a low

echo spacing. This, in turn, speeds up the acquisition and reduces blurring from T2-decay and low peak amplitude to stay within the hardware limitations.

The following methods were evaluated as possible candidates:

- ❏ VERSE
- ❏ Optimal Control
- ❏ Time-Shifting
- ❏ Root-Flipping
- ❏ PINS
- ❏ multiPINS
- ❏ Optimized Phases

The VERSE approach could be a good choice. However, it creates pulses that are sensitive to imperfections and the performance of the gradient system, especially at off-center positions.

The optimal control approach can produce impressively compressed RF pulses and was the winner of the 2015 ISMRM RF Pulse Design Challenge. However, as it is based on VERSE it shares its sensitivities. Another drawback of the optimal control approach is that it cannot be generated in the pulse sequence since each SMS factor, slice gap, and slice thickness combination poses a new optimization problem that cannot be solved fast enough. Therefore, the optimal control method was deemed too unreliable and impractical for the task at hand.

Time-shifting and root-flipping share the same problem. Neither can be used with RARE without breaking the CPMG conditions. Either because signals of different slices will refocus either at different time points or incompatible requirements on gradient amplitudes. Both methods were developed to be used for diffusion applications, where these problems are not as detrimental. The root-flipping method also requires significant computation time.

PINS and multiPINS pulses work best if the acceleration factor is high or slices are thick relative to the gap in between the slices; otherwise, they become too long to be useful in a RARE sequence. The SMS acceleration factors (2-5) used in this work were in general too low for PINS pulses to be effectively used as excitation or refocusing pulses. However, for the inversion pulses, the PINS pulse was used or, more specifically the adiabatic DANTE pulse. This multiband inversion pulse was based on a hyperbolic-secant (110) pulse and is shown in Figure 23. The slice thickness of the inversion is typically wider than the imaged slice (111), creating a more beneficial situation for the PINS pulse.

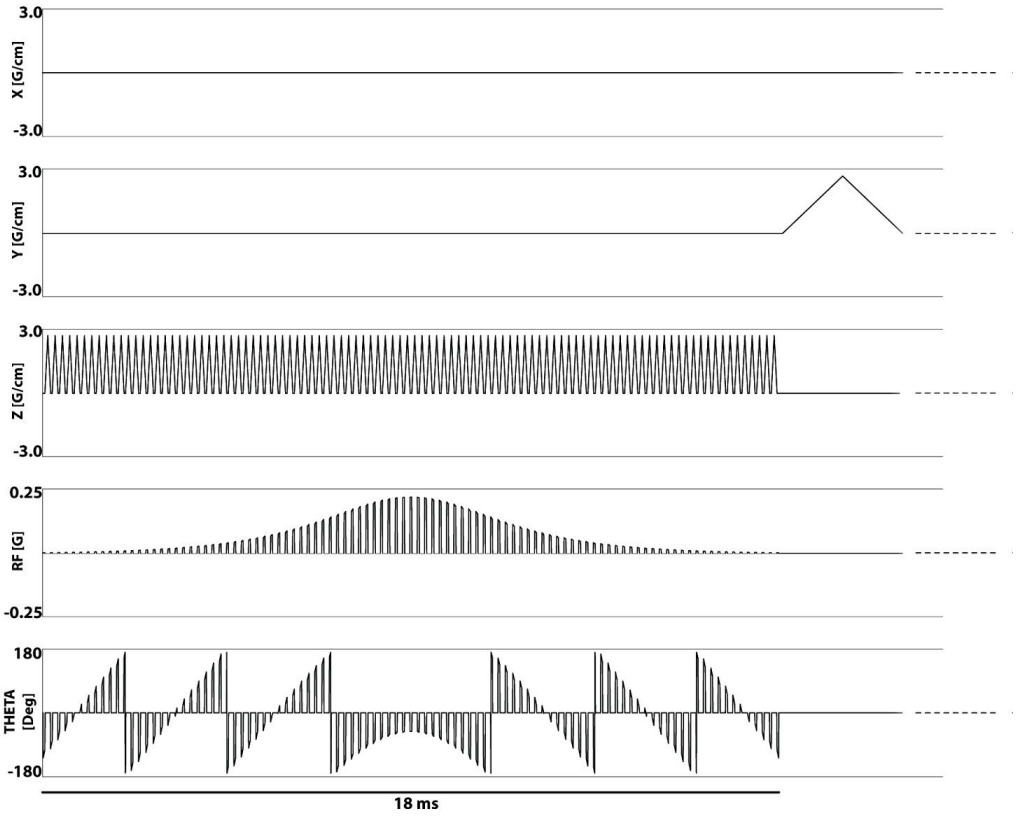

Figure 23. *A PINS-DANTE inversion pulse based on a hyperbolic-secant pulse.*

The multiphoton multiband adiabatic RF described in Ref. (70) could have been an interesting alternative to the DANTE pulse, however, the paper had not yet been published when this work was performed.

Finally, the optimized phases method was deemed the most suitable for the purposes of this project. Of all the methods, it provides the smallest reductions in peak amplitude. However, it is simple and practical, and it facilitates the online generation of multiband pulses in the pulse sequence. It also produces pulses that work with the CPMG conditions. Since this method cannot provide as large of reductions of peak amplitude, gaussian shaped pulses were used to help minimize the amplitudes.

4.1.4 CAIPIRINHA

The CAIPIRINHA scheme was used to increase the slice separation performance in the parallel imaging reconstruction. The phase ramps of CAIPIRINHA can either be realized with gradient blips before and after each readout or by changing the underlying phases of the RF pulses used to create the multiband pulses. Since a

RARE and not an EPI sequence was used, it was possible to use the RF version. However, the gradient blips were easier to implement and therefore more flexible to use. The slight dephasing at the edges of the slice profile was considered insignificant. The blipped-CAIPIRINHA is also the method that has found the most widespread use.

In order to avoid an increase of the echo spacing when adding CAIPIRINHA blips, a novel solution was developed. This was achieved by an implementation detail, where the necessary phase ramps were produced by altering the area of the crusher gradients (see Figure 24b) instead of adding gradient blips (Figure 24c).

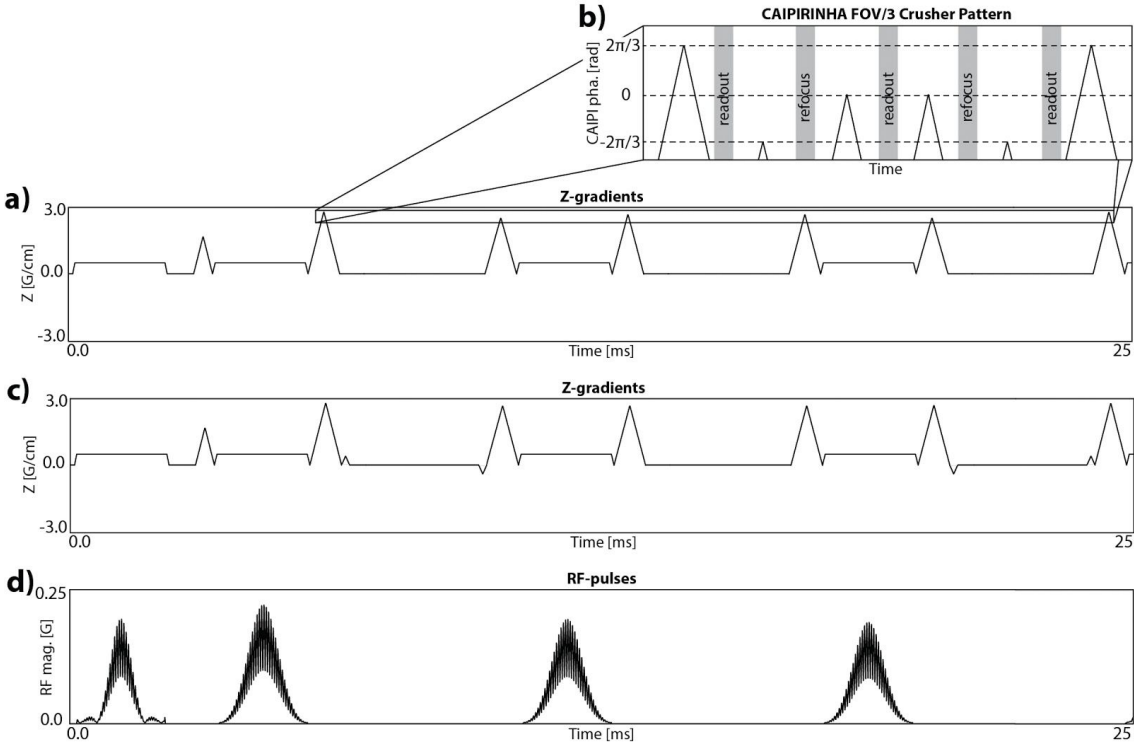

Figure 24. *Pulse sequence diagram showing a case of SMS acceleration 3 and CAIPIRINHA FOV/3. Panel* ***(a)*** *shows how the CAIPIRINHA shift was accomplished using the crusher gradients;* ***(c)*** *shows how the same CAIPIRINHA shift can be accomplished using the gradient blips; and* ***(d)*** *shows the RF magnitude. In* ***(b)*** *a schematic view of how the crusher gradients are scaled to create the desired CAIPIRINHA-pattern is shown.*

Further developments of the CAIPIRINHA concept, such as wave-CAIPIRINHA, do not improve the reconstruction quality at the rather low acceleration factors used in this work. They also increase the complexity of the reconstruction.

4.1.5 Parallel imaging

The slice-GRAPPA method was used to reconstruct the SMS accelerated PROPELLER data, because, at the time it was considered the best and most developed method (with the split-slice-GRAPPA extension). GRAPPA was therefore chosen as the method to reconstruct the accompanied in-plane acceleration.

When accelerating an acquisition with SMS, embedded ACS lines cannot be used as slice-GRAPPA calibration since this calibration requires separate information about the otherwise simultaneously excited slices. A separate set of calibration data is needed, where the slices are acquired independently. To avoid acquiring calibration data for each blade angle, a single data set was used for all blade angles, as illustrated in Figure 25.

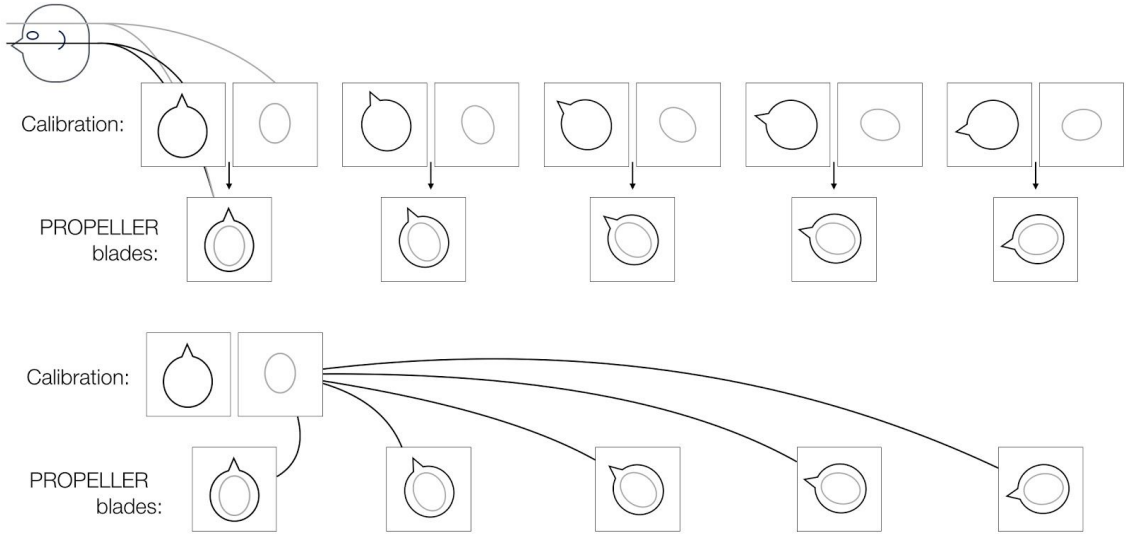

Figure 25. Top: *Showing that each SMS accelerated PROPELLER blade needs its own calibration data at the correct angle.* ***Bottom:*** *With rotated and interpolated GRAPPA kernels the same calibration data can be used for all blades, and, consequently, significantly less calibration data has to be acquired.*

It was possible to use calibration data acquired at a different angle than the accelerated data through the development of rotating GRAPPA kernels. The method is based on the fact that when the image of a PROPELLER blade is rotated to a specific angle the coil sensitivities are also rotated. Consequently, the influence of the coil sensitivities on how k-space pixels are related is also rotated. Therefore, the GRAPPA weights of an arbitrarily rotated k-space acquired with the same set of coils (i.e., the same slice position) could be found by counter-rotating the kernels and interpolating their source points. This process is described in Figure 26. The

rotation of GRAPPA kernels was inspired by the work done with APPEAR by Holmes et al. (104).

A fully sampled first blade was used as calibration data for the PROPELLER implementation. The calibration data could have come from a separate gradient echo or FLEET (fast low-angle excitation echo-planar technique) sequence (112). However, a fully sampled PROPELLER blade presented a simpler way to create a standalone sequence. All raw data came in one package and only one scan has to be prescribed, making it easier to implement in the clinical workflow.

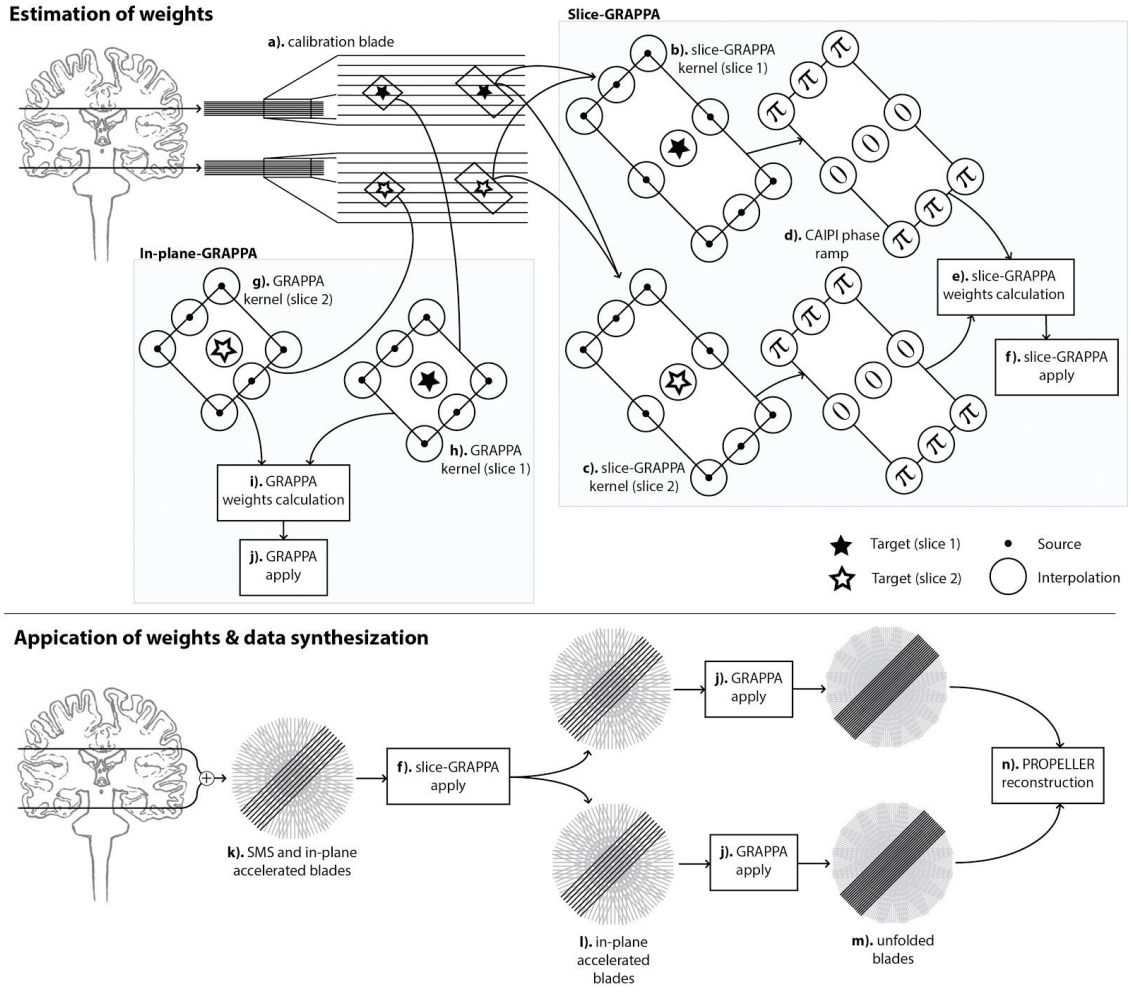

Figure 26. *To unfold the accelerated PROPELLER data (k), GRAPPA and split-slice-GRAPPA were used. The kernels (b,c,g,h) were rotated and interpolated in the calibration blade volume's (a) k-space to calculate weights for the other blade volumes. For CAIPIRINHA, a rotated phase ramp (d) was applied to the calibration data after interpolation. Since the split-slice-GRAPPA kernels (b,c) were trained on fully sampled data and applied to in-plane undersampled data (l), the kernels have the same phase-encoding undersampling pattern. Unfolded data (m) were passed along to an in-house developed PROPELLER reconstruction (n). Reproduced with permission from Paper I.*

Since the SMS accelerated data is acquired with CAIPIRINHA FOV-shifts, corresponding phase ramps were added to the calibration data in the reconstruction. The CAIPIRINHA phase ramp direction follows the unique phase-encoding direction of each blade angle; therefore, the CAIPIRINHA phase ramp added to the calibration had to match the angle of each accelerated target blade, thereby creating an angled FOV shift in the calibration image. However, the interpolation of the kernels in k-space does not represent the sharp transitions of the phase ramps, which caused blurred final images of shifted slices. Therefore, the phase ramps were applied in the kernel after the interpolation., ensuring that phase difference between k-space lines became correct and produced sharp images. An example of this is shown in Figure 27, where SMS accelerated PROPELLER data was artificially generated and reconstructed with phase ramps applied in the calibration data (Figure 27a) and with phase ramps applied in the kernels (Figure 27b).

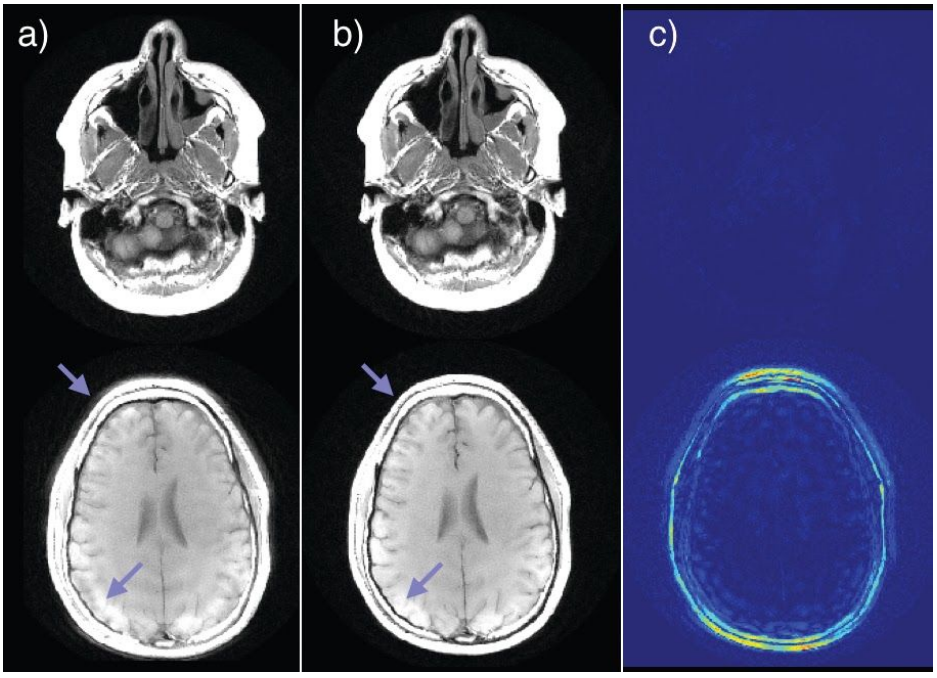

Figure 27. Top row: *A slice position not affected by any CAIPIRINHA FOV-shift. Bottom row: A slice position where a CAIPIRINHA FOV-shift was created.* ***(a)*** *The CAIPIRINHA phase ramps were applied at the correct angle, to the calibration data. Arrows point to the resulting blurring.* ***(b)*** *Here the CAIPIRINHA phase ramps were directly applied in the slice-GRAPPA kernel.* ***(c)*** *The difference between* ***(a)*** *and* ***(b)*** *clearly shows that only the shifted slices are affected by the blurring.*

A similar issue arises when SMS and in-plane acceleration are used at the same time. Since the slice-GRAPPA was applied before the in-plane GRAPPA the

slice-GRAPPA was trained to tease apart in-plane undersampled data. This can be done, similar to the previous example with the phase ramps, simply by removing lines from the calibration data. However, lines would have to be removed at the correct angle to match the target blade, which would obstruct the interpolation. It made more sense, therefore, to also incorporate the undersampling into the kernel. This is why the slice-GRAPPA kernels in Figure 28 are rectangles with gaps between the source points.

4.1.6 3D motion correction with PROPELLER

As described in the background and theory chapter, the original and conventional implementations of PROPELLER motion correction is performed within each slice with 2D motion estimation between blade angles in k-space. A remaining issue for PROPELLER motion correction is how to handle out-of-plane motion. The original method used weights to suppress the contribution of blades that are deemed corrupted by out-of-plane motion. However, this is not effective if there were multiple out-of-plane head-poses during the acquisition. Therefore, each slice-stack (for one blade angle) was treated as a "brick" and 3D rigid body motion correction was performed between the bricks and a reference brick (see Figure 28). Treating the bricks as one time-point requires that all slices are acquired within the same TR. It is not possible to do 3D motion correction in a set of 2D k-spaces; therefore, the correction was performed in the image domain.

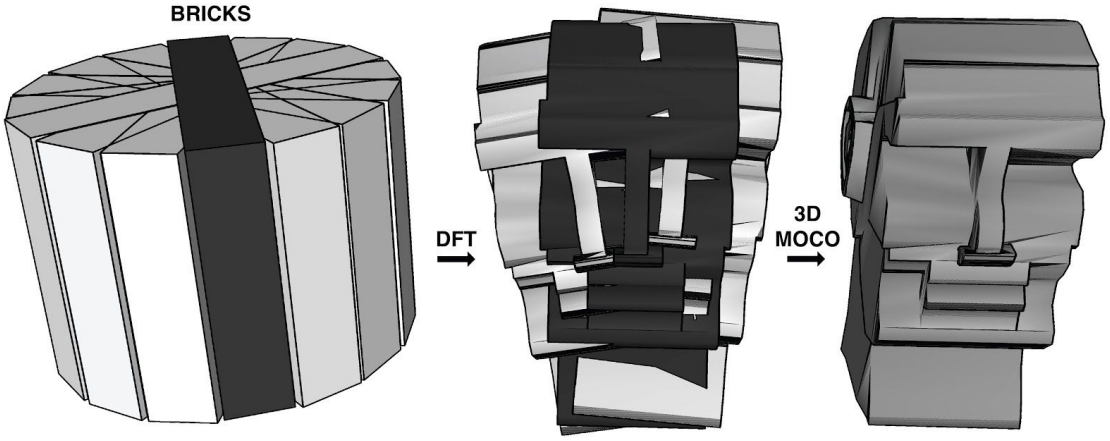

Figure 28. *A PROPELLER data set in k-space and image space. 3D motion correction is performed by aligning each brick in image space to a reference (dark gray).*

A bootstrapping approach was used to find the reference brick. First, all bricks were scored according to their deviation from the mean of all bricks. Then the brick with the most deviation was disposed of and the remaining bricks were scored again, relative to their mean. This process was repeated until only one brick remained, which, consequently, was chosen as the reference.

4.1.7 Finding applications

The first image contrast acquired with the SMS PROPELLER sequence was a T1-weighted SE. The T1-weighted SE sequence is, in the brain, limited to a TR of 400-600 ms; therefore, SMS cannot be used to directly shorten the TR. It was, however, possible to drastically shorten the scan time by reducing the number of acquisitions if many slices were to be acquired (see Figure 29).

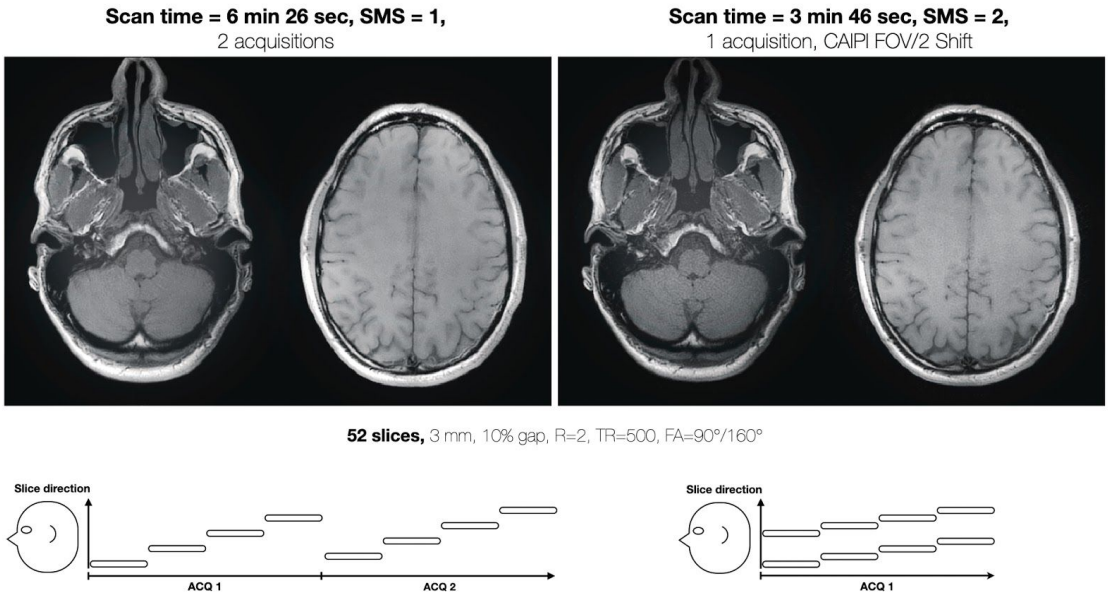

Figure 29. Left: *Two slices of a T1-weighted PROPELLER scan divided into two acquisitions to keep the TR around 500 ms.* ***Right:*** *Two simultaneously excited slices of a SMS accelerated T1-weighted PROPELLER scan that now could be acquired in one acquisition.*

Unfortunately, the increased MT effects of the multiband pulses and loss of the slice gap when acquired in a single acquisition were detrimental to the GM/WM contrast, as previously discussed in the background and theory chapter. An attempt to use a short RARE train (i.e., low echo train length (ETL)) together with the driven equilibrium method (113) was also explored (see Figure 30). However, the same conclusion was drawn here, and both paths of the project were abandoned.

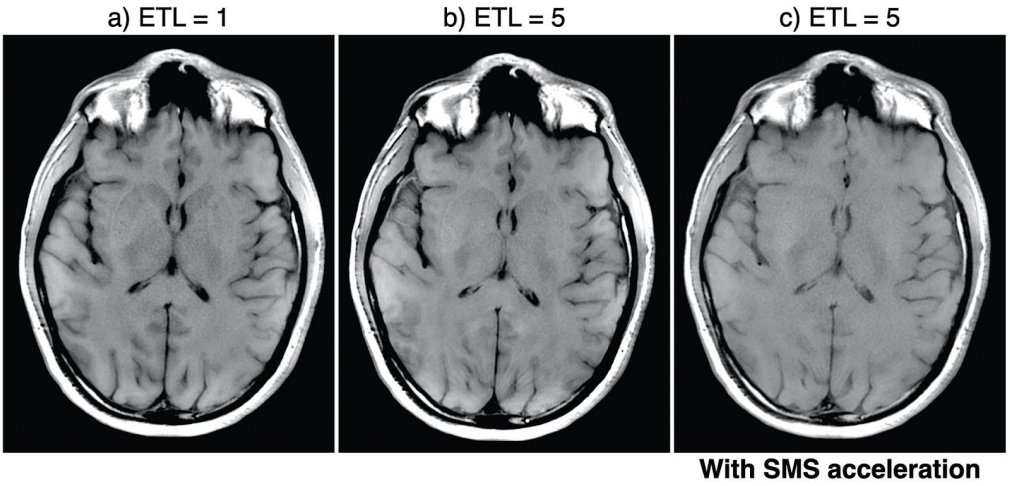

Figure 30. (a) *A T1-weighted PROPELLER scan acquired with ETL = 1.* ***(b)*** *A T1-weighted PROPELLER scan acquired with ETL = 5, significantly increasing the efficiency of the acquisition.* ***(c)*** *A T1-weighted PROPELLER scan acquired with ETL = 5 and accelerated with a SMS factor of two. In this case the GM/WM contrast is almost none, due to MT effects.*

In order to overcome the rigid TR and MT effects, but still produce T1-weighted images, T1-FLAIR images were acquired. For T1-FLAIR, the TR can be 1500-3000 ms, and since the inversion boosts the GM/WM contrast, it is possible to obtain a sufficient T1-weighting.

Next, the SMS accelerated propeller sequence was used to acquire T2-weighted images. T2-weighted RARE acquisitions are more flexible when it comes to the choice of TR and since the GM/WM contrast is reversed, compared to T1-weighted images, any increase in MT effects would not be as damaging. The images are presented in the results and discussion chapter.

4.2 Project II: T1-weighted 3D EPI

4.2.1 The aim of Project II

The aim of Project II was to develop excitation pulses for T1-weighted 3D EPI sequence. The RF pulses, therefore, needed to produce adequate fat suppression while keeping the TE short in order to avoid chemical shift artifacts and generate a good T1-weighting.

4.2.2 Short Summary of the Work

A 3D EPI sequence was used to rapidly acquire T1-weighted isotropic volumes with low geometric distortions. The TE was kept low by using brief excitation RF pulses, with a short EPI train, and partial-Fourier. The choice of the RF pulse was based on the quality of fat suppression and measured GM/WM contrast. Binomial RF pulses were compared to water exciting rectangular RF pulses and an SLR pulse.

4.2.3 Choosing the RF pulses

The excitation RF pulse used in the T1-weighted 3D EPI sequence needed to provide sufficient fat suppression and a short TE. A short TE can either be accomplished by an overall short duration or a minimum-phase pulse, where the magnetic moment starts late in the pulse. Furthermore, acquiring the 3D EPI with the frequency-encoding in the S/I direction avoids the need for spatial selectivity.

Of the pulses covered in the section on water exciting pulses, the most interesting was the WE-rect since it could provide a reduction of MT effects as well as fat suppression in a relatively short duration. A weakness of the WE-rect is its narrow stopband. Therefore, a new pulse was conceived, which can be seen as an extension of the WE-rect. Binomial pulses can achieve wider stopbands; however, they have repeating off-resonance passbands that cause MT-effect. In fact, they have been suggested as MT pulses for MT imaging sequences (116,117). These off-resonance passbands were, in this work, suppressed by convolving a binomial pulse with the WE-rect, which, under the small FA approximation is equivalent to a multiplication of the two pulses' frequency responses.

The convolution of a Binomial 1-1 pulse with the WE-rect results in a 1-2-1 shaped pulse, here termed a WE-rect 1-2-1. Consequently, the convolution of a Binomial 1-2-1 pulse leads to a WE-rect 1-3-3-1, and so on. Examples of these pulses can be

found in Figure 31. The on- and off-resonance trajectories of the WE-rect 1-3-3-1 compared to the WE-rect are shown in Figure 31f. The extended WE-rect pulses produced wider stopbands and reduced off-center excitations, at the cost of longer durations. However, the gain in stopband width quickly diminished, with respect to the increase of duration.

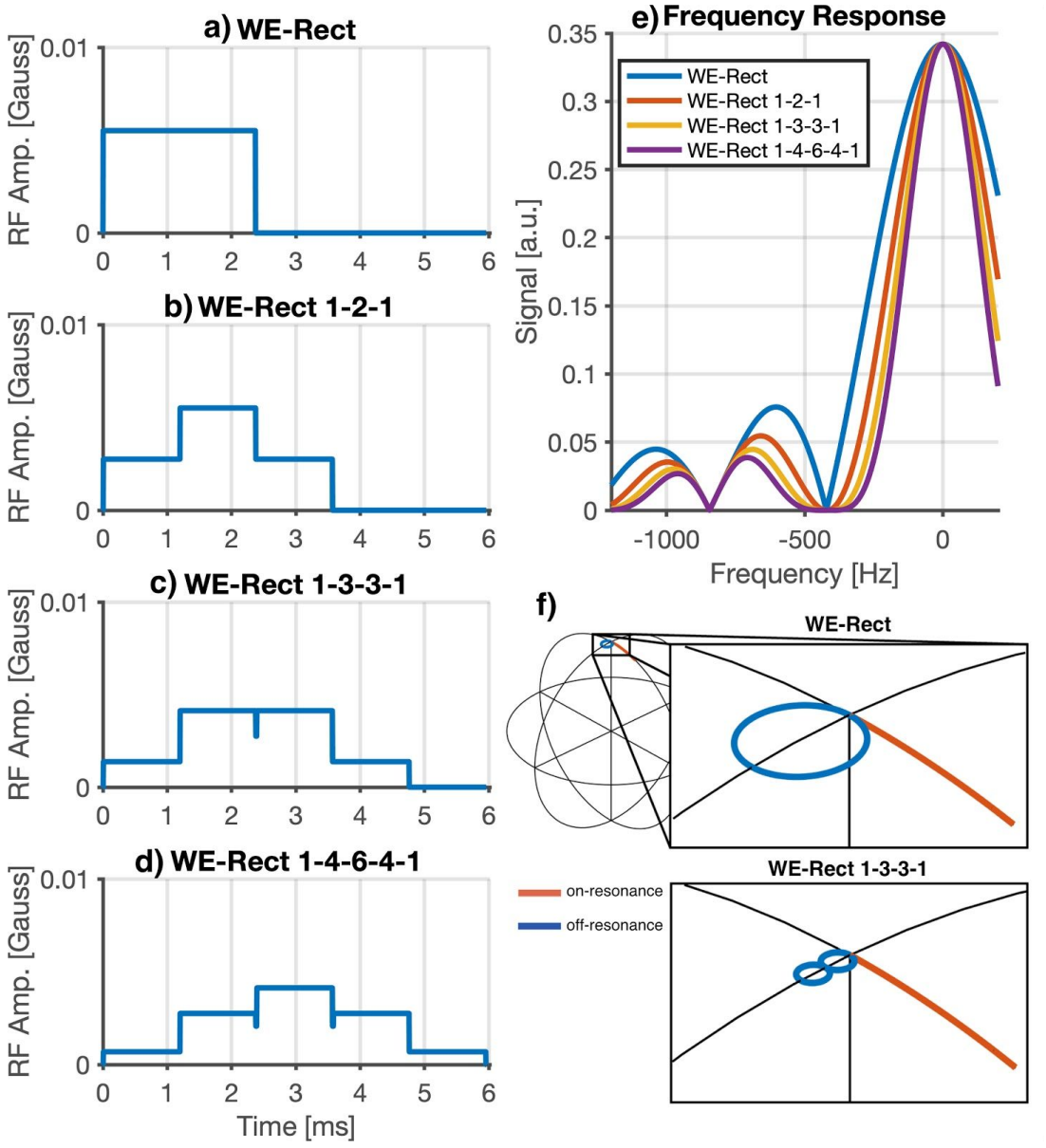

Figure 31. (a–d) *WE-rect pulses with increasing number of sub-pulses.* ***(e)*** *Bloch simulated frequency responses of pulses in (a–d).* ***(f)*** *The trajectories at on-resonance and at the off-resonance position of fat at 3 T for the WE-rect and the WE-rect 1-3-3-1.*

Since the extended WE-rect pulses are based on the small FA approximation, their performance is dependent on the flip angle. Figure 32c shows that at FAs above

40° the FA at the frequency of fat starts to increase. However, this can be remedied by heuristically adjusting the amplitude of the central plateau in the WE-rect 1-2-1 pulse. By increasing its amplitude by only 2% the pulse can be used for FAs up to 90°, as demonstrated in Figures 32b and d.

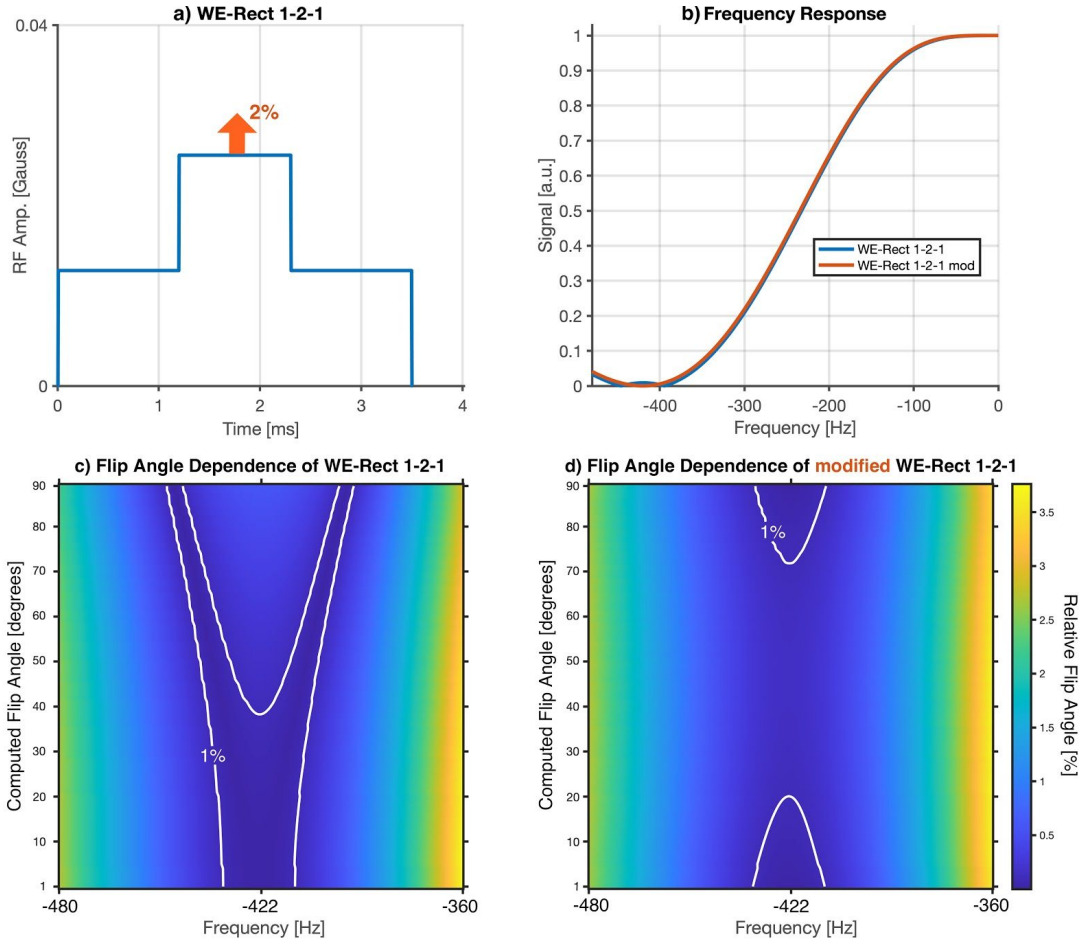

Figure 32. *Demonstrating that the WE-rect 1-2-1 FA dependence can be mitigated by simply increasing the amplitude of the center sub-pulse by 2%.* ***(a)*** *The WE-rect 1-2-1.* ***(b)*** *The frequency response of both the modified and the original pulse at 90° flip angle. A slight "bump" can be seen at the frequency of fat (422 Hz).* ***(c)*** *The FA dependence of the WE-rect 1-2-1, showing Bloch simulations of FAs ranging from 1 ° to 90 °. The horizontal axis shows a frequency band centered around the principal fat frequency. The color map corresponds to the relative FA of each computed pulse, at on-resonance, scaled to the flip angle.* ***(d)*** *The FA dependence of the modified WE-rect 1-2-1. The "bump" around 422 Hz is eliminated.*

The LIBRE pulse was excluded because it excites a slope of FAs across the water peak. Which is not suitable for T1-weighting when the GM/WM contrast is dependent on the flip angle. The BORR pulse, on the other hand, could have been

included. However, the author was not aware that the BORR pulse could avoid the FA slope of the LIBRE pulse.

A water exciting SLR (WE-SLR) pulse was also created in order to demonstrate that the rectangular pulses can achieve water excitation with shorter pulse durations. It should also have minimum MT effects as it excites only the water peak. Figure 33 shows the 3 T WE-SLR pulse used in Paper II and a 1.5 T example. The 1.5 T pulse required more than double the duration in order to produce a similar frequency response.

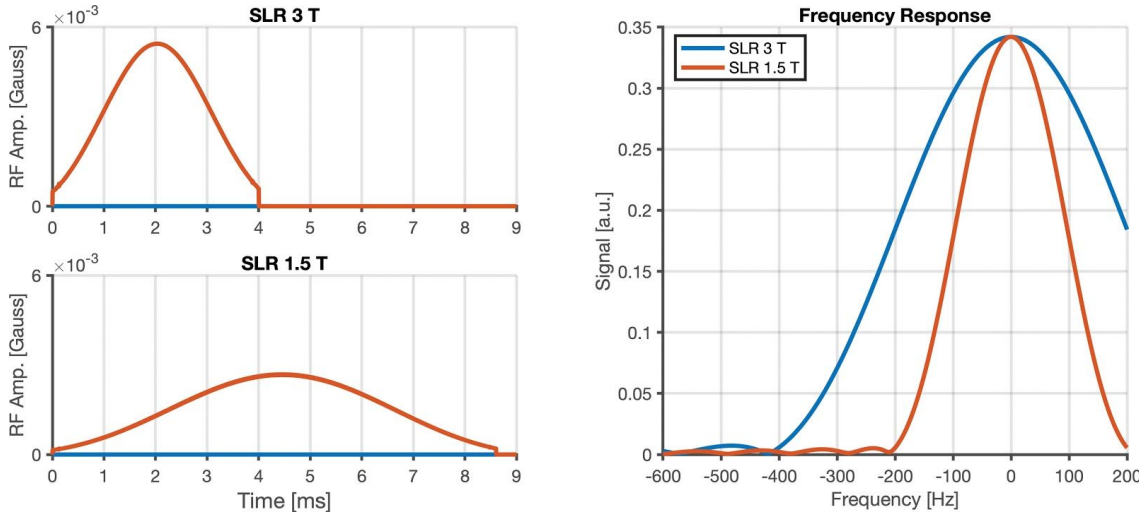

Figure 33. (a-b) *WE-SLR pulses designed for 3 T and 1.5 T respectively.* ***(c)*** *Bloch simulated frequency responses of the pulses.*

4.3 Project III: T1-FLAIR PROPELLER & PMC

4.3.1 The aim of Project III

T1-FLAIR is one of the key contrasts in any neurological protocol. Therefore, as part of a bigger project to create a fully motion-corrected neurological exam protocol, here aimed at creating a T1-FLAIR sequence that could handle very large head movements occurring continuously throughout the scan.

4.3.2 Short Summary of the Work

The PROPELLER trajectory's robustness to movement artefacts and retrospective motion correction features was paired with prospective motion correction using the WRAD. Three approaches were tested to integrate the marker-navigator into the PROPELLER sequence. The SAR of the T1-weighted FLAIR PROPELLER sequence, and resultant scan time, were lessened using a VRFA scheme. Motion correction performance assessments were conducted for four participants and three forms of head motion.

4.3.3 SAR and TRAPS

The T1-FLAIR PROPELLER sequence is an interleaved inversion recovery sequence (114) with adiabatic inversion pulses and acquired with a RARE train. This causes a high SAR because many high power RF pulses are generated back to back. To limit the heating of the patient, dead-times are inserted, which significantly increases the total scan time.

To avoid this scan time penalty, lower refocusing FAs can be used. The TRAPS method was chosen since it preserves SNR while providing large SAR reductions. Specifically, the sineTRAPS (42) was used because it enables even lower FAs than the original TRAPS (see Figure 34). Another benefit of the sineTRAPS scheme is that it produces a smoother signal evolution, which should cause narrower point-spread function PSF (i.e., less blurring).

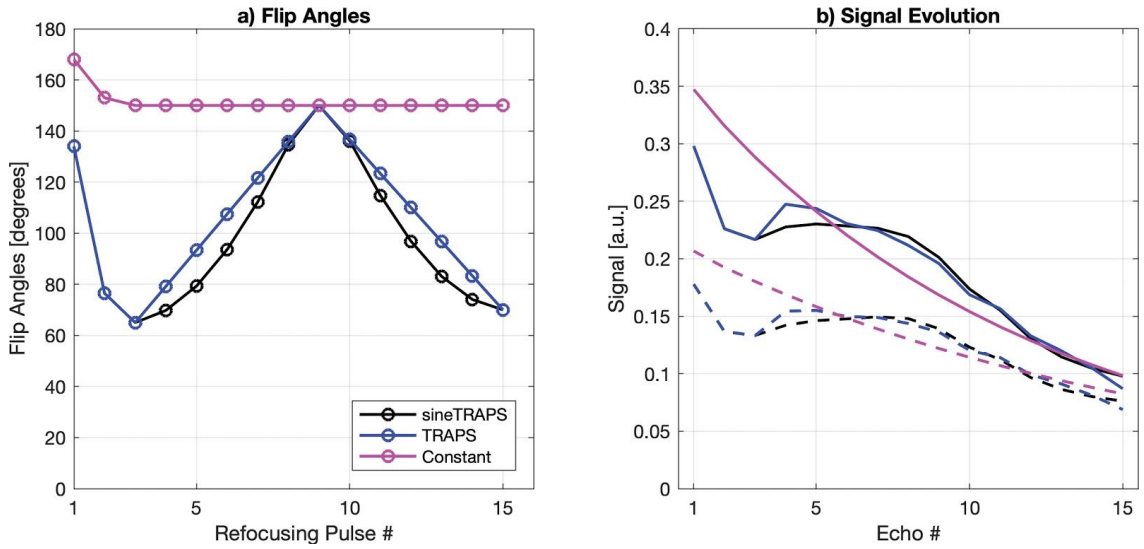

Figure 34. (a) *Three VRFA schemes; 150 ° constant FAs in pink, TRAPS FAs in blue; and black sineTRAPS scheme. The relative SAR values are 0.71, 0.38 and 0.34, respectively.* ***(b)*** *The resulting EPG simulation of the three schemes for gray (--) and white (–) matter.*

The VRFA schemes used for 3D sequences where a portion of the signal amplitude is kept constant for a portion of the echo train was excluded because it requires a long echo train.

The sineTRAPS scheme was compared to a constant FA train with the same SAR and one with higher FAs, 82°, and 120° respectively. The three schemes are presented in Figure 42. Using these three refocusing FA schemes, three T1-FLAIR PROPELLER data sets were acquired, using the same TI, TR, and TE. The constant 120° scheme required dead-time to be added after each readout to keep within SAR limitations. The same dead-time was subsequently added to the two acquisitions using the constant 82° and TRAPS schemes in order to produce comparable image quality. To evaluate the effect of the TRAPS scheme, the following method was used to measure GM/WM contrast, CNR, and SNR.

Noise maps were estimated using method number three described in Ref. (115), where the readout bandwidth is doubled, effectively doubling the image FOV in the readout direction. In the reconstruction, two k-spaces with the correct FOV were then formed by picking out every other sample, creating one k-space containing all odd samples and one k-space containing all even samples. A third k-space was produced by gridding all samples down to the originally prescribed matrix and FOV using a sinc-kernel (116). All three k-spaces were subsequently run through the PROPELLER recon, except for the motion correction part. After coil-combination and before gridding the blades, a noise k-space was calculated by subtracting the odd sample k-space from the even sample k-space and dividing by

the square root of 2. The gridding procedure, therefore, yielded one signal and one noise map.

To measure GM/WM-CNR, GM and WM were segmented using SPM12 (117). The resulting probability maps for GM and WM were used to create binary masks containing only pixels with a probability score higher than 98%. To avoid coil sensitivity effects, the image volumes were divided into 48x48 pixel (34x34 mm) sized region of interest (ROI) segments. Only ROIs containing more than (48x48)/5 pixels of both binary masks were included in order to ensure reliable measurements, resulting in 34 ROIs throughout the image volume. The contrast was calculated as the difference between the mean GM compartment and the mean WM compartment within each ROI. The noise in each ROI was estimated by taking the standard deviation of the noise in both compartments. Finally, the CNR was calculated by dividing the contrast measurements by the corresponding noise measurement. The SNR was measured by dividing the mean signal of both compartments by the corresponding noise estimate. The measurement results are presented in Figure 43.

The contrast-equivalent TE for the center echo of each scheme was calculated using the method described in Ref. (118).

4.3.4 2D motion correction for PROPELLER

A T2-weighted PROPELLER can be acquired in a way that all the slices are acquired within the same TR. However, FLAIR PROPELLER works best if each blade is acquired during several different TRs because the inversion slice thickness can be increased with respect to the imaged slice. This way, uninverted cerebrospinal fluid is less likely to flow into the imaged slice. Therefore, the 3D motion correction described in Project I cannot be used since slices within one brick were acquired at least half of the total scan time from each other and cannot be treated as one time point. Thus, the motion algorithm was limited to 2D and applied for each slice separately.

One benefit of a 2D correction is that as long as the slices within a blade angle, which are acquired in about 100-200 ms, can be aligned as long as they are not corrupted by motion. In contrast, the 3D correction requires the whole brick, which is acquired in 2–3 s, to be somewhat consistent. This makes the 2D more suitable for the rapid head movements that this project is aimed to correct. However, out-of-plane movements cannot be corrected. Therefore, they are expected to be corrected by the PMC.

4.4 Ethical Considerations

During the development of any new MRI technique, it is tested many times and refined on healthy volunteers. The healthy volunteers are usually the physicists themselves because it is more convenient. Later, when and if the technique is deemed ready, it sometimes needs to be tested on patients. In this process, two main ethical issues arise: incidental findings in volunteers and implications for patients.

4.4.1 Incidental findings in volunteers

A meta-analysis from 2009 by Morris et al. (119) states that: "The crude prevalence of incidental findings on brain MRI is 2.7%, or one for every 37 neurologically asymptomatic people scanned". There is therefore a considerable risk that something wrong is accidentally found whenever a new volunteer is imaged.

At the neuroradiology department, it is policy to always have a radiologist review the images acquired for research purposes and inform the volunteers if there is a clinically relevant finding. It is one of the recommended approaches, according to Illes et al. (120), for research that is performed in connection to a hospital where specific expertise (radiologists in this case) is available.

It is impossible, however, to have a radiologist check all the images that the physicists take themselves on a weekly basis. Furthermore, the images that are produced are not always of clinical quality and are typically of one specific image contrast. This makes it more unlikely to find something. Therefore, should there be a different approach when the physicists are the volunteers? One possible solution would be to have a radiologist check an optional clinically viable examination that is performed every once in a while. If an incidental finding is made, the following discussion is easier to have in private and under controlled circumstances.

4.4.2 Informed consent

With the current procedure, the patient learns about the study after they have been called in from the waiting room, after which they give their consent to the nurse performing the examination. When the patient is called their condition is known and it is possible to exclude, for example, patients with dementia, in order to

protect their autonomy. Furthermore, nurses can also evaluate whether the patient is fit for inclusion upon meeting the patient.

It is difficult to convey adequate and understandable information about the physics and technical details involved in the research to the volunteers. However, the patient only needs to consent to add the additional time (usually under 10 minutes) to their examination and to the use of the resulting images in publications.

When it comes to ethical considerations the research performed here the considerations are rather simple. MRI is quite safe when operated correctly, and as long as the extra time spent in the scanner does not bother the patient, there are no real drawbacks to consenting to the study.

5 Results and Discussion

This chapter will discuss material not covered in the papers and some new results that have been produced in the wake of the papers. The author will also expand on future developments, and the limitations of the projects and papers.

5.1 Project I: SMS Accelerated PROPELLER

The major findings of Project I:

1. A PROPELLER acquisition could be efficiently accelerated using SMS, with one fully sampled blade as calibration data for a slice-GRAPPA algorithm employing rotated and interpolated kernels.

2. This SMS accelerated PROPELLER sequence could be used to acquire p3D volumes that could provide motion robust reformattable volumes.

5.1.1 SMS acceleration

This project has shown that T2-weighted and T1-FLAIR images can be successfully acquired with an SMS accelerated PROPELLER sequence. Example images are shown in Figure 35 and Figure 36. The combination has the following synergistic advantages: (1) it improves the 3D RMC due to shorter TR, and (2) it enabled the acquisition of motion corrected p3D PROPELLER volumes, and (3) it spreads out slice-leakage artifacts across the FOV because of the unique phase-encoding direction of each blade and CAIPIRINHA.

Following Paper I, the SMS accelerated PROPELLER sequence was used to acquire p3D T1-FLAIR volumes (121). The resulting images and reformats are shown in Figure 35. The SMS accelerated PROPELLER sequence was also used to rapidly acquire regular T2-weighted images, as shown in Ref. (122). Here, 34 4 mm slices were acquired in 32 s using an in-plane acceleration factor of 2 and an SMS acceleration factor of 2. Two of the 34 slices are shown in Figure 36. This rapid acquisition is potentially useful for imaging uncooperative patients since it is both quick and motion-corrected.

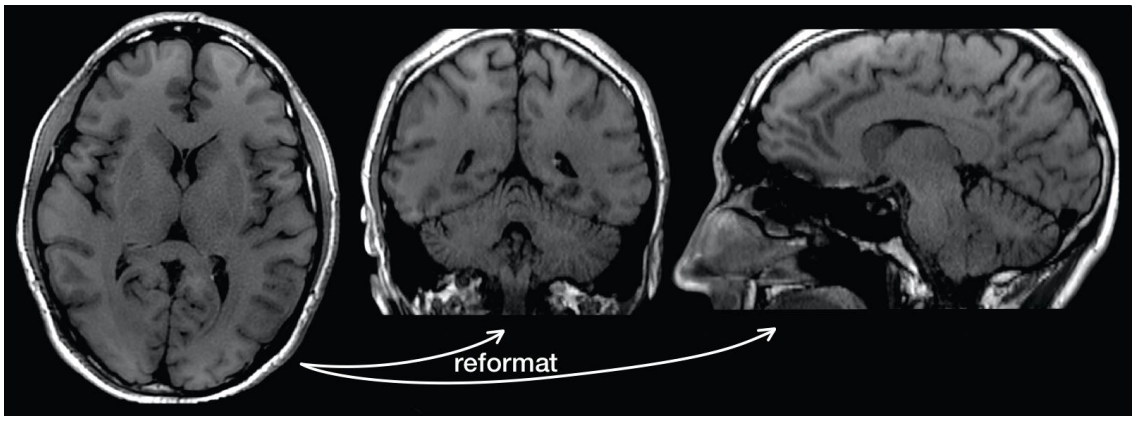

Figure 35. *T1-FLAIR SMS accelerated PROPELLER. Axial slices and reformatted sagittal and coronal views. Scan parameters were as follows: R = 2, SMS = 2, FOV = 240×240 mm², matrix = 240×40, slice thickness = 1.5 mm, 100 slices, exc./ref. FA = 90°/111°, RBW = ±50 kHz/FOV, TE/TR = 13/1993 ms, ETL = 10, two acquisitions and a scan time of 3 min.*

PROPELLER is an important technique in the clinical setting, due to its robustness against motion and flow artifacts (123–129). Therefore, it is of value to keep developing the technique in order to take advantage of the latest advancements in the MRI field. In the field of acceleration, the SMS technique has had a significant impact on how diffusion and fMRI images are acquired. It is, therefore, potentially valuable to add this feature to the PROPELLER sequence.

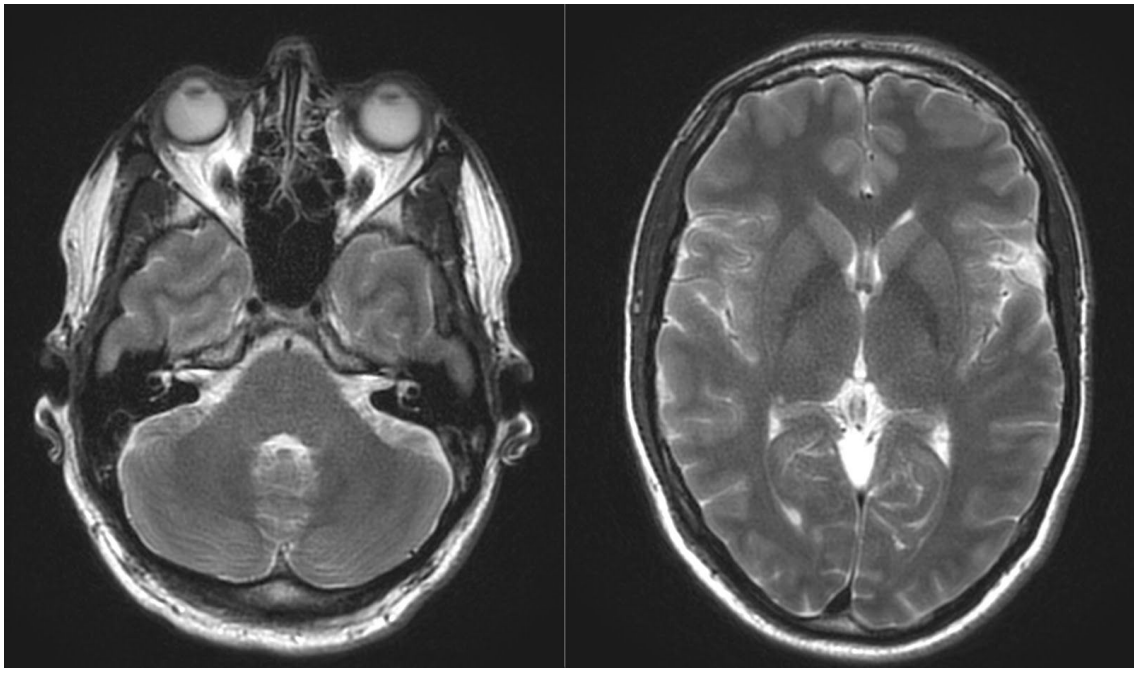

Figure 36. *Two slices of an SMS and in-plane accelerated T2-weighted PROPELLER, with an acquisition time of 32 seconds.*

5.1.2 Pseudo 3D

As mentioned in the background and theory chapter, the SMS acceleration is less adopted in RARE imaging than with diffusion and fMRI. The main problem with combining SMS and RARE is the relatively high energy requirement of the MB RF pulses, thereby leading to increased SAR when, as in RARE, many high FA RF pulses are generated back to back. Another contributing factor could be that the field of MRI has been pushing for 3D acquisitions of regular contrasts, such as T1- and T2-weighted images. However, a p3D volume can be acquired with many thin 2D slices (130,131).

Comparing a p3D volume with 1 mm thick slices to a regular 2D image with 3-4 mm thick slices, the thinner slices come with the benefits of reformability and higher resolution; however, a drawback is reduced SNR. A more interesting comparison is to compare the p3D to a real 3D acquisition.

In order for a T2-weighted 3D RARE to be efficiently acquired, it needs a very long echo-train, with ETLs of around 80. This is because it excites the whole volume with each excitation, while the TR is limited to be at least 3 s. To make the best use of those 3 seconds, as much of k-space as possible must be acquired. This long echo-train causes image blurring, since the signal amplitude changes throughout the train. While VRFAs are used to mitigate this effect (118), the blurring is still significant. This blurring is avoided in a p3D PROPELLER acquisition, since the ETL is much lower, around 25. Even though PROPELLER acquisition is inherently blurred by the oversampling of the k-space center the p3D PROPELLER images appear significantly less blurry than a 3D RARE acquired at with the same voxel size, as can be seen in Figure 37, which shows results from Ref. (132).

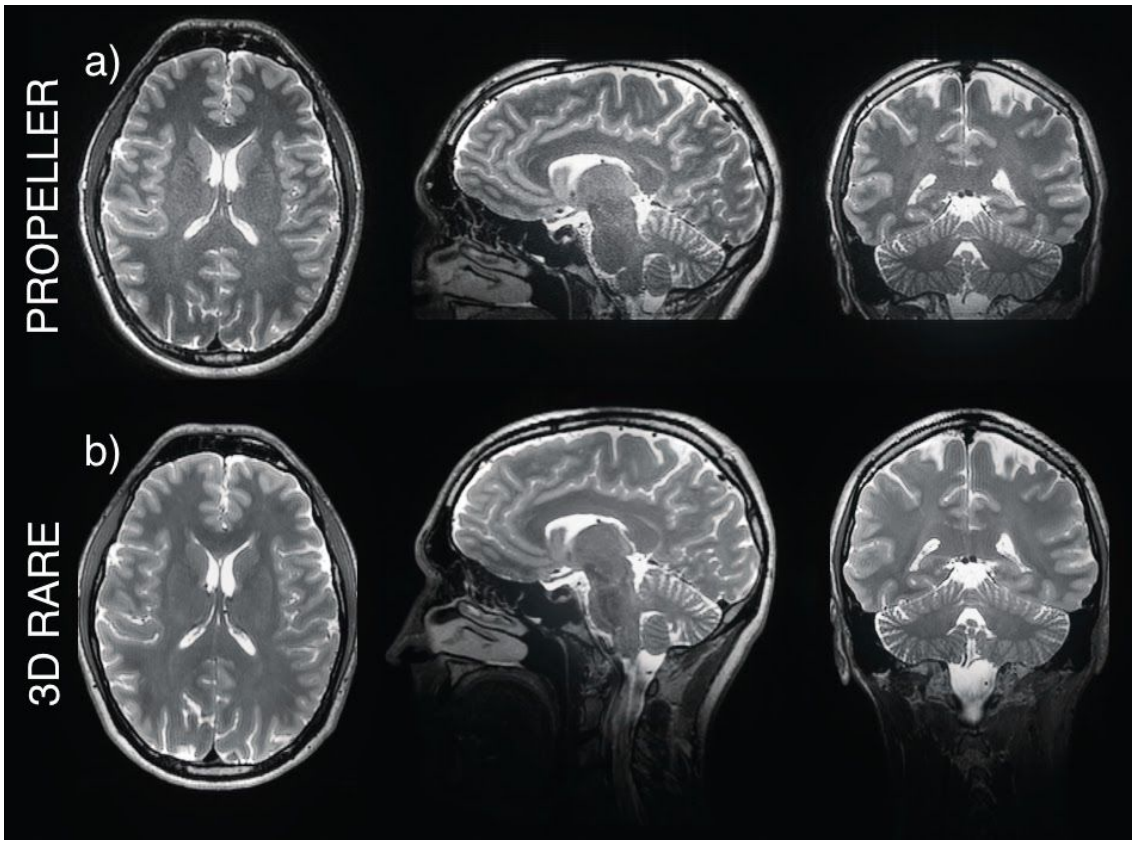

Figure 37. *Volunteer imaged with T2-w SMS PROPELLER* ***(a)*** *and with a T2-w 3D RARE* ***(b)****, both with a voxel size of 1.0×1.0×1.0 mm3. The scan time was 2:30 min for the PROPELLER acquisition, and 3:15 min for the 3D RARE acquisition. The PROPELLER data was acquired with axial slice orientation, the sagittal and coronal views being reformats from the axial data. The 3D RARE data was acquired in the sagittal plane, the axial and coronal views being reformats from the sagittal volume. The reformats of the PROPELLER data have clear anatomical structures and no slice cross-talk, as well as higher effective resolution compared to the 3D RARE images.*
Reproduced with permission from Paper I.

Going to higher resolutions than 1 mm^3 voxels is straightforward with the 3D RARE, however, the p3D RARE starts to run into problems with the size of the slice selection gradients. Larger gradients need more time to ramp up and down, adversely affecting the echo-spacing. However, a large slice selection gradient will reduce the needed crusher area, which could remove some of the added echo spacing. This was not done in the current study but will be explored in the future. The large gradients can also cause significant eddy-currents, which would change the k-space trajectory at the edges of k-space. Furthermore, in the context of SMS, the CAIPIRINHA blips are potentially adversely affected by such eddy-currents. This has not yet been investigated and needs to be looked at in the future.

When it comes to sensitivity to head motion, the 3D is significantly more sensitive since it has longer echo trains and a reduced ability to retrospectively correct the data. As mentioned in the background and theory chapter, there are methods that try to replace lines or segments of k-space data using parallel imaging. However, they were deemed out-of-scope for the evaluations performed in this work.

The T2-weighted p3D PROPELLER was pitted against the 3D RARE with PMC using the PROMO technique. The results are shown in Figure 38. Here the reduced sensitivity to the motion of the PROPELLER is clearly seen. However, the success of PROMO and the 3D PROPELLER RMC largely depends on when the motion occurs.

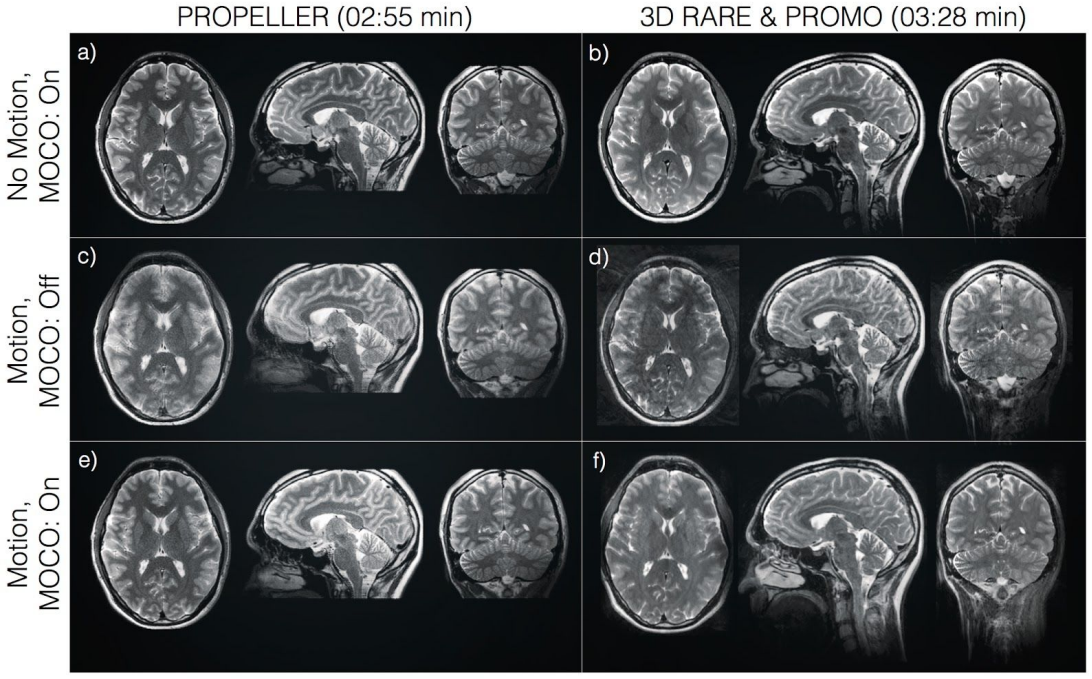

Figure 38. *Acquisitions with SMS PROPELLER and 3D RARE with and without motion. The PROPELLER images (left column) show axial slices with sagittal and coronal reformats. The 3D RARE images (right column) show a sagittal segment with axial and coronal reformats.* ***(a)*** *SMS PROPELLER acquisition without motion, with motion correction.* ***(b)*** *3D RARE without motion, with PROMO motion updates on.* ***(c)*** *SMS PROPELLER acquisition with motion, without motion correction.* ***(d)*** *3D RARE with motion, with PROMO motion updates off.* ***(e)*** *PROPELLER acquisition with motion and motion correction.* ***(f)*** *3D RARE with motion and PROMO motion updates on.*

For PROMO, if a sudden motion occurs in the pause, before the navigators, it is able to address it. On the other hand, if it occurs anytime between from after the end of the navigator and the end of the echo train, the PMC is rendered relatively useless. The same goes for continuous motion, since PROMO can only correct for a small portion of the motion. The PROPELLER has similar limitations since it has a

temporal footprint of a few seconds (the TR) and can only correct for inter-brick movements, whereas intra-brick movements cannot be corrected and hamper the inter-brick correction.

The stepwise motion pattern performed in the PROPELLER versus PROMO experiment had a pacing that was asynchronous with the TR of both the PROMO and the PROPELLER acquisition. This was done in an attempt to create a motion pattern that was equally challenging for both sequences. The resulting patterns are shown in Figure 39.

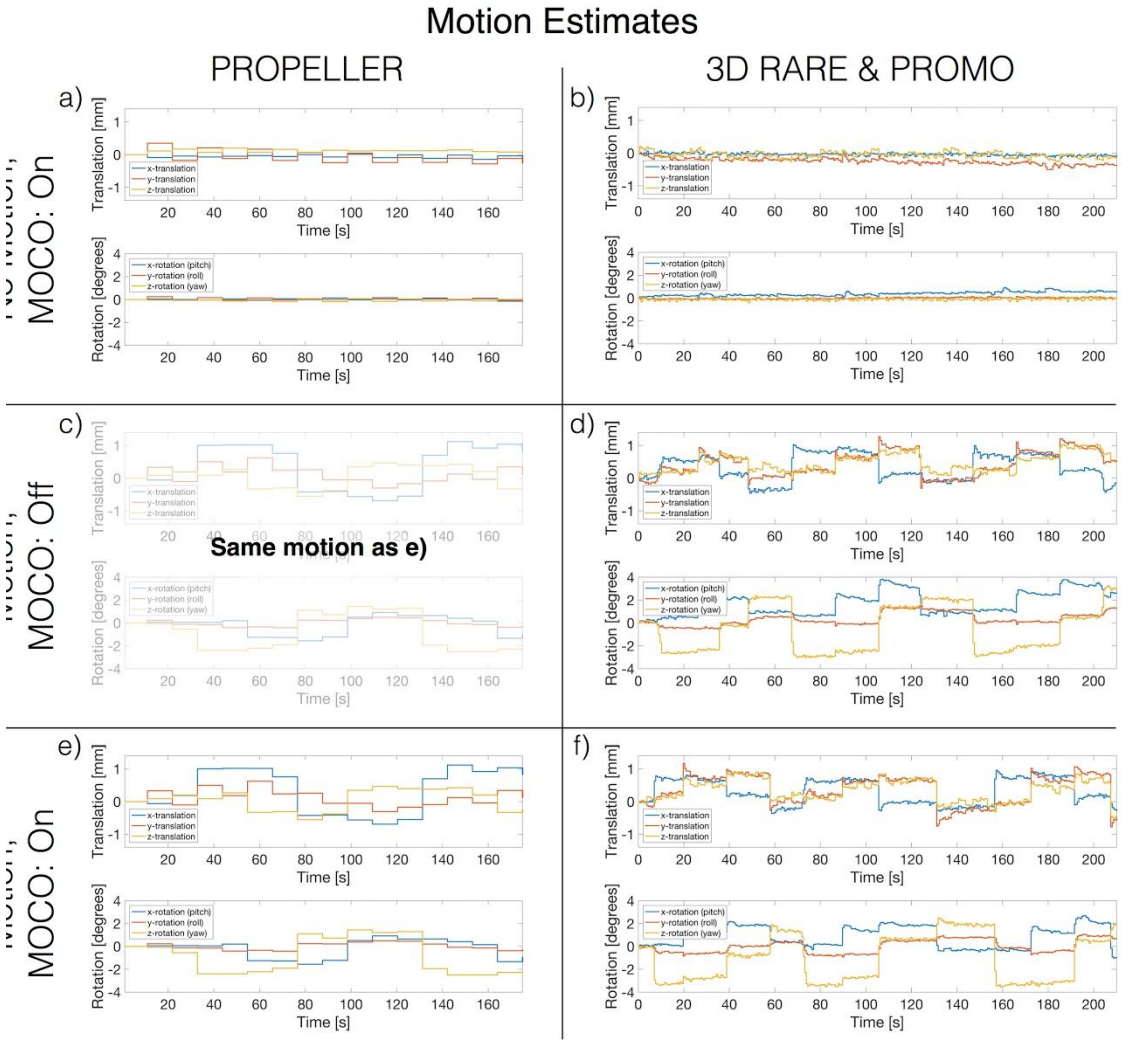

Figure 39. *Motion estimates from the acquisitions in Figure 38.*

One advantage of PROMO, in this case, is that it is possible to detect and reacquire data collected during a large movement, which cannot be done with the current PROPELLER implementation.

An advantage of 3D acquisitions over 2D acquisitions, in the context of motion, is that 3D imaging is less sensitive to spin-history effects and miss-match of slices since the whole volume is excited and refocused every time.

Even though the noise amplification of SMS acceleration is low, the SNR of very thin slices is low to begin with. This limits the usefulness of higher acceleration factors. In the PROPELLER case, the TR can be reduced with SMS, which improves the motion correction and the lost SNR could be regained to some degree by increasing the number of blades. By adding more blades the motion correction also improves, since a potentially corrupt blade is averaged out. However, this could increase the colored noise that comes from the oversampling of the k-space center.

5.1.3 Limitations of Project I

Limitations of the current implementation of the SMS accelerated PROPELLER include an increase in RF power. This caused an increase in echo spacing by about 30%, which, in turn, increased the TR. This is the opposite of the goal of SMS and is therefore the most important issue to address in future work. The most obvious approach would be to use the VRFA scheme from Project III.

The evaluations of image quality in Paper I would have benefited from a quantitative measurement, for example, SNR, g-factor maps, or the linear system leakage approach (81). Such a measurement was not included because the images showed the effects of acceleration.

A more rigorous investigation into the effect of the interpolation of the GRAPPA kernels on the data synteziations would have been useful. For example, when the original MATLAB code was reimplemented in C++, it was discovered that whether the coordinates of the kernel hit the center of each pixel or somewhere between pixels significantly impacted the image quality. The reconstruction produced less slice leakage artifacts when the interpolation points were between original grid points.

Many GRAPPA variations have examined the effect of the contributions of the center of k-space on the reconstruction quality (133). This would have been interesting to explore in the context of slice-GRAPPA and this case where the interpolation makes the choice of interpolation points more flexible.

5.2 Project II: T1-Weighted 3D EPI

The major findings of Project II:

1. The reduced MT effects of the WE-rect pulses leads to a significant increase in GM/WM contrast.
2. A T1-weighted 3D EPI volume with isotropic voxels and low distortions could be acquired rapidly.

5.2.1 RF-pulses

All experiments in Project II were performed at 3 T. If the sequence were to be used at 1.5 T, then all RF pulses need to be about twice as long in order to suppress the fat signal and even longer for the SLR pulse shown in Figure 33. In terms of acquisition efficiency, this only leaves the shortest original WE-rect as a viable option. On the other hand, at 7 T the pulse durations become less than half as long than at 3 T. Their short duration and very low SAR make them well suited for use at high field strengths. On the one hand, high field strengths have increasing issues with B_1 homogeneity, which could have adverse effects, as mentioned in Paper II. The FA of the WE-rect pulses impacts the nulling frequency (i.e., the quality of the fat suppression), making the pulses somewhat sensitive to B_1 inhomogeneity. However, the effect is negligible at the FAs used in Paper II (9–18°). In Ref. (26), they show that the nulling frequency of a WE-rect generated for an FA of 20° is unaffected even if the achieved FA is off by more than 20°.

A drawback of using spectrally selective water exciting pulses is that they tend to be sensitive to B_0 inhomogeneity, which effectively shifts the fat and water peaks. The impact of this on the fat suppression is discussed in Paper II; however, the FA at the water peak changes as well. With the pulses used in this study, any shift of the water peak will lower the achieved flip angle. For the T1-weighted 3D EPI, this means that the SNR will become higher, as long as the FAs stay above the Ernst angle (134). However, the GM/WM contrast will decrease. Fortunately, for brain imaging the B_0 variations, even at 3T, are generally low. However, signal drop-out can be observed in areas close to air-to-tissue boundaries. These are also the regions where the EPI distortions are most prominent, making it less of a problem since the signal would have been corrupted anyway.

One possibility to further improve the pulses used for the T1-weighted 3D EPI is to treat it as an optimization problem and use, for example, *optimal control* that has been successfully applied to create multi-band RF pulses, as discussed in previous

sections. This could, for example, utilize the fact that, since the main fat peak resides on only one side of the water peak, the frequency response could be asymmetrical.

5.2.2 Potential uses for the MT-reducing RF pulses

In addition to the increased GM/WM contrast shown in this work, the WE-rect pulse has been shown to increase the tSNR of fMRI (26). A similar approach has been proposed to decrease the MT effects in bSSFP (135) by increasing the duration of the hard RF pulses and thereby narrowing the spectral selectivity. This result implies that there is a possibility to increase the GM/WM contrast and SNR of T1-weighted 3D RARE acquisitions by stretching the hard refocusing pulses. Consequently, this would come at the cost of increased echo spacing. However, it would be interesting to explore how long the RF pulses need to be in order to have an effect on the MT. A similar argument could be made for the MP-RAGE (magnetization prepared – rapid gradient echo) (136) sequence; however, since the GM/WM contrast is already boosted by the inversion preparation, the MT reduction might have a negligible effect.

Finally, the WE-rect pulse could be used with a regular SPGR sequence, thereby increasing the time penalty since it requires one excitation per readout. In the example shown in Figure 40, the scan time was almost doubled. However, it comes with several benefits in addition to the GM/WM contrast increase and low SAR. The fat suppression makes the image easier to interpret, especially if the images are acquired post gadolinium enhancement, since the fat can obscure contrast uptake. Without signal from fat, the choice of TE becomes more flexible, since phase cancellations in voxels containing both fat and water are no longer an issue. Another benefit of suppressing the fat signal is that it can avoid Gibbs-ringing from the fat surrounding the head; this can be seen in the frontal most part of the brain in Figure 40. Furthermore, the SNR increase due to both the MT reduction and the longer TR could be used to accelerate even more and potentially regain some of the lost scan time.

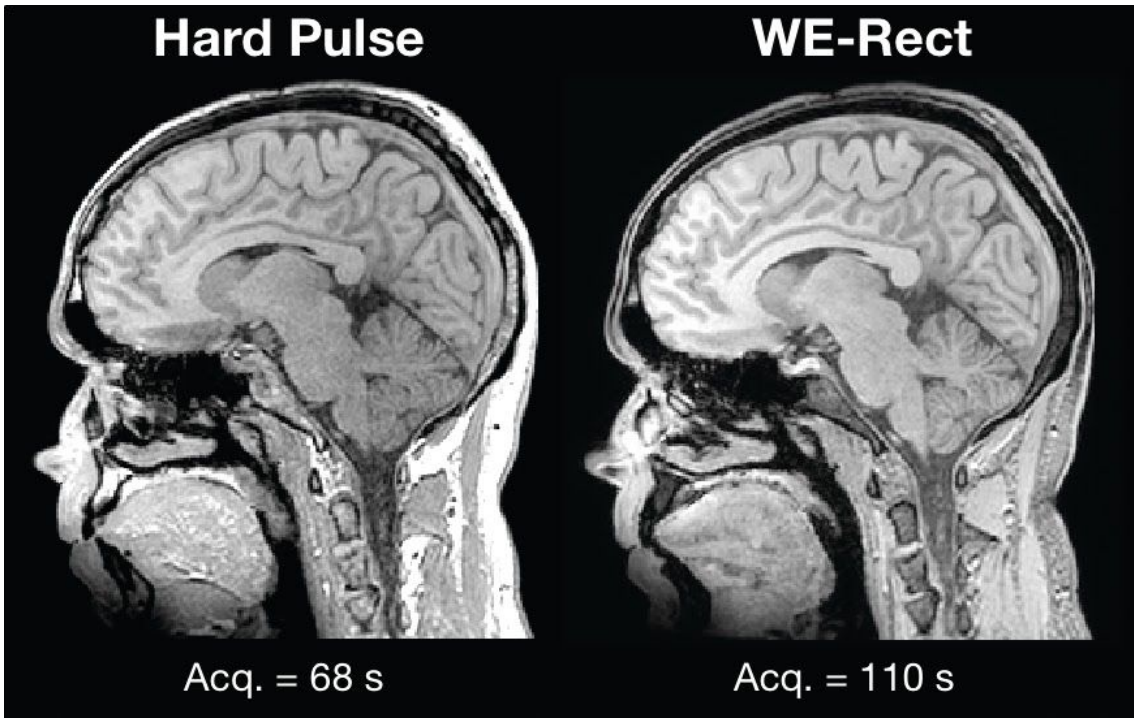

Figure 40. *Two T1-weighted SPGR acquisitions where the left uses a short hard pulse and the right uses a WE-rect.*

5.2.3 The T1-weighted 3D EPI sequence

The 3D EPI images were acquired with the frequency-encoding direction in the superior-inferior direction to suppress signal from blood flowing into the brain. Since EPI is generally acquired at high bandwidths, the FOV can be increased in the frequency-encoding direction without a significant scan time increase. For the 3D EPI, this enables simultaneous imaging of both the brain and spine. Examples of such images are shown in Figure 41. To avoid fold-in artifacts from the shoulders, the SPSP pulses described in the background and theory chapter can be used (Figure 41c). The sensitivity of the frequency selective pulses to B0 fluctuations is clearly demonstrated, as the fat suppression fails at the upper back in Figure 41b and c. Furthermore, breathing causes shot-to-shot phase variations that produce incoherent ghosting in the neck, as can be seen in Figure 41a, b, and c. The possibility of larger FOVs and quick acquisition times makes the 3D viable for use as a scout, or localizer.

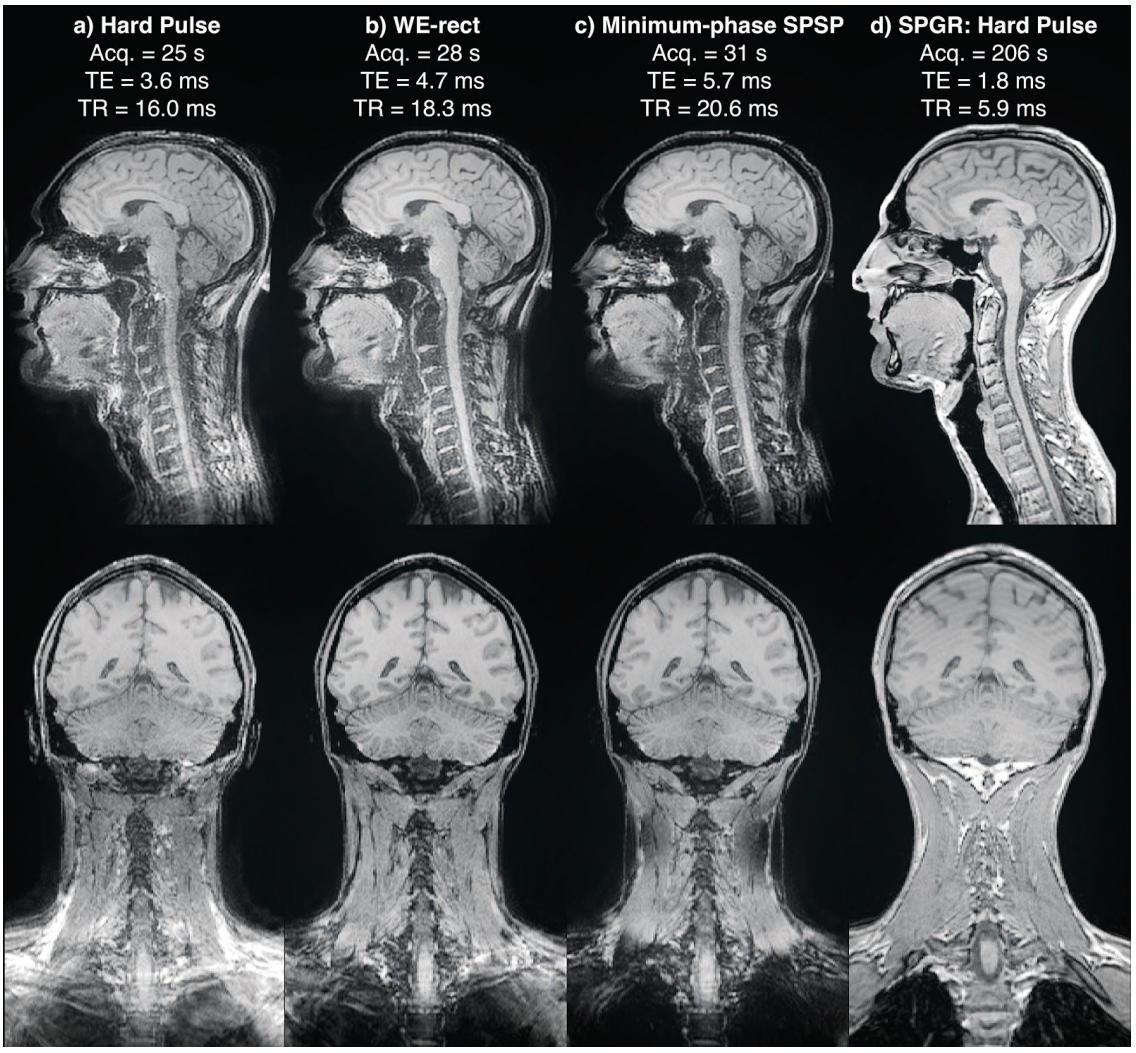

Figure 41. (a–c) *Three 3D EPI acquisitions with a large FOV, employing different excitation pulses:* ***(a)*** *a short hard pulse,* ***(b)*** *the WE-rect, and* ***(c)*** *a minimum-phase SPSP.* ***(d)*** *An SPGR acquisition that can be viewed as a reference.* ***Top row:*** *Sagittal images.* ***Bottom row:*** *Coronal reformats.*

The 3D EPI sequence could also be used to acquire quantitative T1 maps using a variable FA method (137). The low MT effects could be useful in this case since it can affect the T1 values, as demonstrated in Ref. (138).

5.2.4 Limitations of Project II

The GM/WM contrast was measured as the ratio between the mean of the whole GM and WM compartments divided by the sum of both compartments. However, this might not have been the best choice of contrast definition since it weights the contrast with the overall signal strength. The WE-rect pulses are expected to

increase the signal strength, and therefore this contrast definition might have deemphasized the effect they have on the GM/WM contrast. Defining contrast simply as the ratio between the mean of the whole GM and WM compartments could have been a better choice.

It would have also been possible to perform an SNR measurement and calculate the CNR. However, for this study the GM/WM contrast was the most important feature to measure since that is what the sequence needs inorder for it to compete with an 3D IR-SPGR (136).

Since the GM/WM contrast depends on the FA, a map of the actually achieved FAs would have been useful to fully characterize the RF pulses.

5.3 Project III: T1-FLAIR PROPELLER and PMC

The major findings of Project III:

1. The WRAD and PROPELLER combinations enable imaging during continuous very large and rapid head moments.
2. The TRAPS VRFA scheme could significantly decrease the SAR of the T1-FLAIR PROPELLER sequence without any SNR or image quality loss.

5.3.1 TRAPS

While acquiring the three data sets with the three refocusing FA schemes shown in Figure 42a, the 120° scheme led to a scan time of 03:50 min, a 59% increase due to SAR penalties, compared to the 82° and the TRAPS that avoided SAR penalties. In the EPG simulation, the TRAPS scheme produced higher signal amplitudes around the central echoes than both constant schemes (Figure 42b). This resulted in a mean SNR increase of 2% compared to the 120° scheme and a 12% increase compared to the 82° scheme. Furthermore, the signal modulation produced no visible blurring in the images displayed in Figure 43.

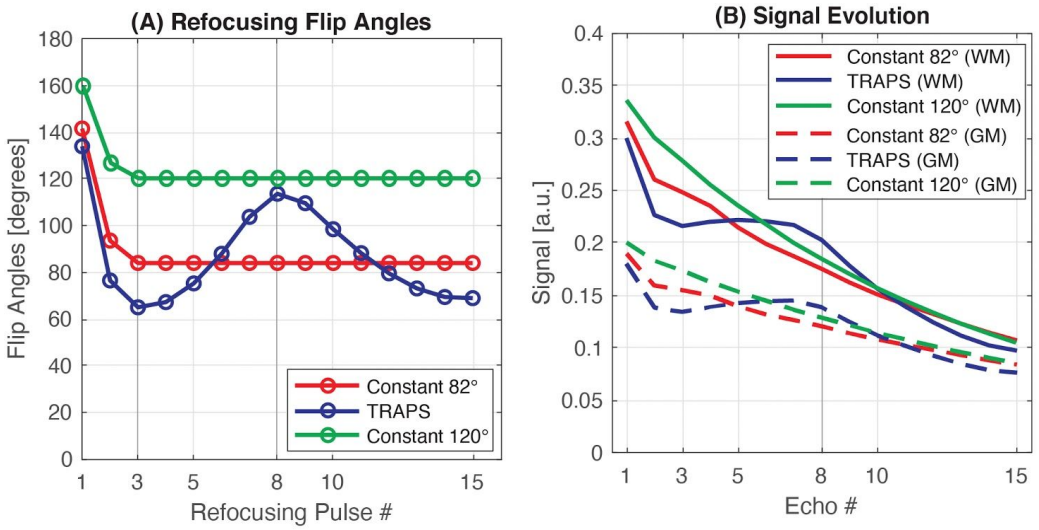

Figure 42. (A) *Three refocusing FA schemes: constant FAs of 120° in green, constant FAs of 82° in red, and the TRAPS scheme in blue. The constant FA scheme of 82° and the TRAPS scheme have the same estimated SAR.* ***(B)*** *Resulting EPG simulation of the three schemes for gray and white matter. Reproduced from Paper III.*

With an echo spacing of 7.4 ms, the TE at the center echo was 51.8 ms. However, the contrast-equivalent TE was 46.5 ms for the 120° scheme, 38.5 ms for the 82°

scheme, and 35.3 ms for the TRAPS scheme. Nonetheless, there was no significant difference in either contrast or CNR between the images.

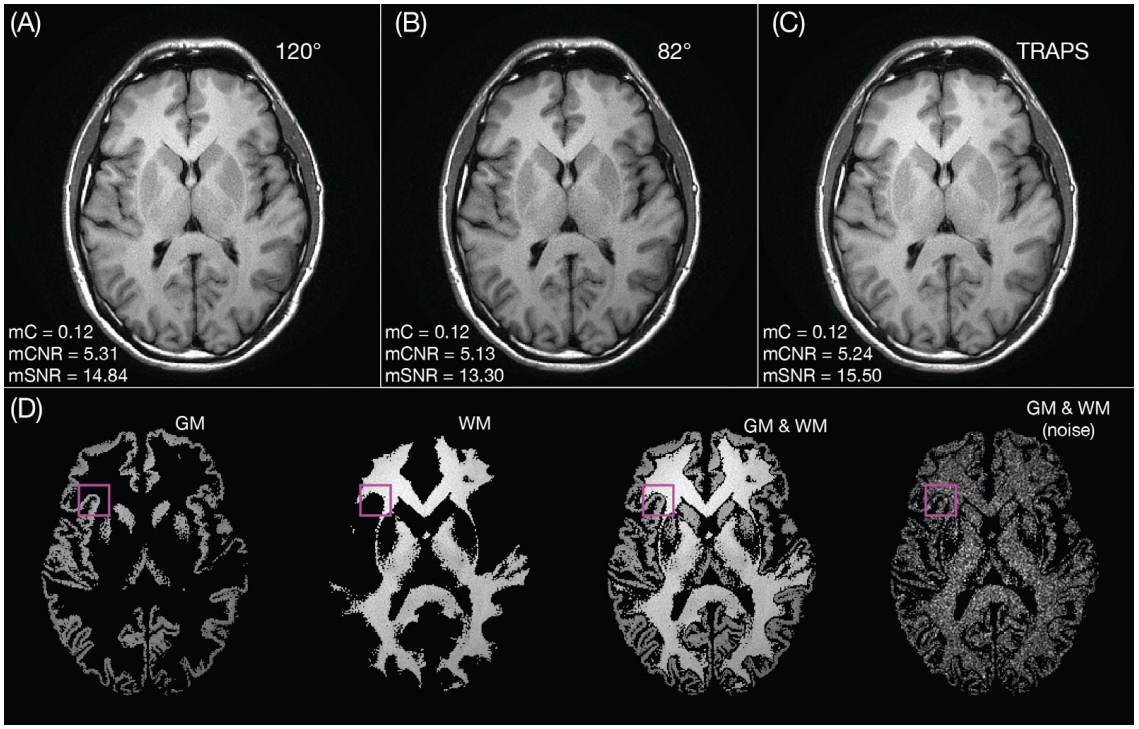

Figure 43. *Results from the evaluation of the refocusing FA schemes.* ***(A), (B)*** *and* ***(C)*** *show images acquired with the constant 120°, constant 82°, and TRAPS scheme. Included are the mean of the contrast, CNR, and SNR measurements.* ***(D)*** *shows one of the GM and WM segmentations (only including pixels with a probability score higher than 98%), and corresponding noise map. The pink square represents an example of one of the ROIs used for the SNR and CNR calculations.*

The TRAPS scheme effectively modulates the signal amplitude across the phase-encoding direction of each blade, which could negatively affect the point-spread function and cause blurring. However, no additional blurring was observed here, which is in agreement with previous studies (139). The author hypothesize that since the signal modulation is moderate, the main contributor to a widening of the point-spread function could be the oversampling of the k-space center due to the overlapping PROPELLER blades.

An added benefit of using low FAs is the shortened contrast-equivalent TE, which could generate a greater T1-w. However, in a PROPELLER trajectory, a majority of the phase-encoding lines contribute to the image contrast since all blades span the center of k-space. This could explain why no significant increase of GM/WM contrast was established. The T1-w could also be improved by using low FAs since it causes less MT effects (43,140), as previously discussed. It was found, however,

that this effect was not large enough to influence the image contrast in this case, likely due to the significant impact of the high power adiabatic IR pulse on the MT effects.

An alternative way of reducing the RF power of the T1-FLAIR sequence could be to modify the adiabatic inversion RF pulse used by the sequence. A less sharp inversion slice profile can reduce the peak power of a hyperbolic secant pulse and thereby the produced SAR. The SAR produced by the inversion pulse could then possibly be balanced with the SAR produced by the refocusing pulses to achieve a slightly higher SNR.

5.3.2 SNR loss

In the results of Paper III, the fastest motion pattern resulted in PI artifacts. These can be seen in Figure 44A as low-intensity streaks around the head. Furthermore, PI fold-in artifacts are typically accompanied by noise amplification. To mitigate this effect, the author proposed a simple solution based on the assumption that if the coil sensitivities have moved away from the slice position that is being reconstructed, a neighboring slice position might have a more similar arrangement of coil sensitivities. To find this better-suited slice, the GRAPPA weights were calibrated on a range of neighboring slices in the orthogonal blade and were, one by one, used to synthesize the missing data. The one that produced the image with the lowest entropy was then picked. Entropy was suggested as a quality metric for motion correction by Atkinson et al. (87,88). It can be used to find the image where the information is contained in the least amount of pixels (i.e., the image least affected by blurring or ghosting due to motion). The results presented in Figure 45 show that, in this case, these PI artifacts could be somewhat mitigated with this method.

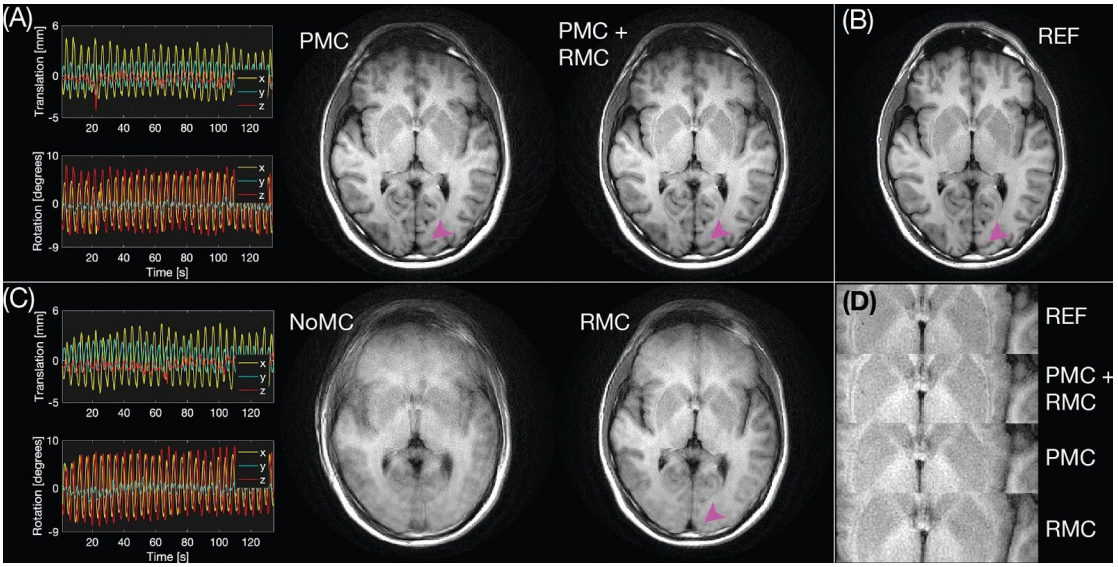

Figure 44. *Results from the circular motion scans.* ***(A)*** *Images acquired with PMC updates (with and without RMC) and the motion estimates.* ***(B)*** *Reference image acquired when the subject remained still.* ***(C)*** *Images acquired without PMC updates (with and without RMC) and the corresponding motion estimates.* ***(D)*** *Enlarged images, showing the external capsule. The pink arrows point to a loss of gray-white matter contrast in the RMC-only image. Note that the sudden drop in z translation in* ***(A)*** *at 20 s is due to the subject swallowing. Reproduced from Paper III.*

This modification of the reconstruction works because GRAPPA utilizes the effect of the coil sensitivities on k-space to fill in the missing lines, and these are not dependent on the anatomy depicted in the image.

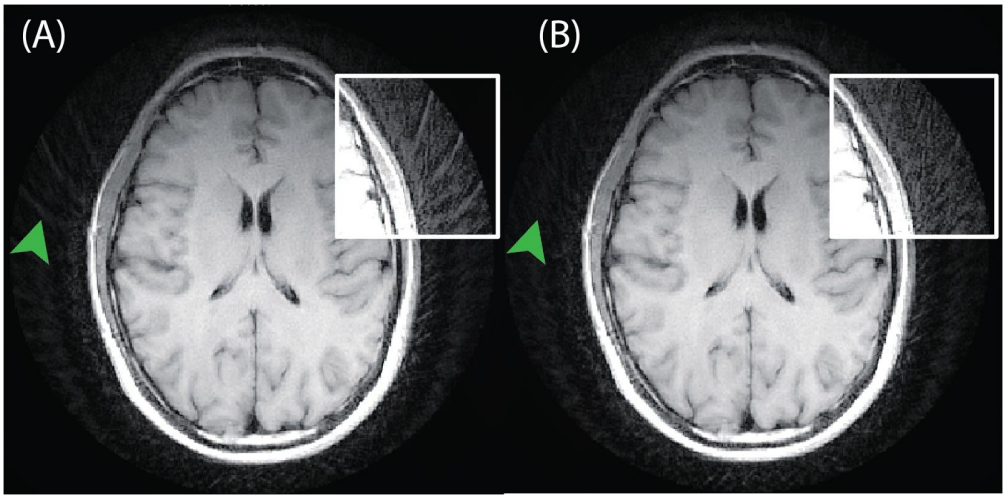

Figure 45. *The same PMC corrected T1-FLAIR PROPELLER data was reconstructed using both the standard orthogonal blade GRAPPA* ***(A)*** *method and the proposed PMC adapted version* ***(B)****. The reduction of PI artifacts can be seen on both sides of the head in the up-scaled square and as pointed out by the green arrows.*

This approach could also be combined with the rotated and interpolated GRAPPA kernels of Project I to increase the search space and the chance of finding matching coil sensitivities. The motion estimates from the WRAD could also be used to find when matching coil sensitivities could appear. This shows that the oversampled nature of a PROPELLER dataset can be utilized in yet another way in order to mitigate the artifacts seen in Figure 44.

P3D volumes could also be acquired with the PMC corrected PROPELLER sequence. However, for the very fast movements performed here, the signal loss, most clearly visible in the last experiment of Paper III, is expected to be greater with thin slices.

5.3.3 Data rejection

Rejection of blade-slices was performed in Paper III in an attempt to mitigate non-correctable out-of-plane motions as well as corruption from spin-history effects. A variation of this is described in the original PROPELLER paper (90), where the blades making up a slice are weighted depending on their data quality. However, no reference could be found where the efficiency of the data weighting or rejection was shown. While it might seem like a reasonable approach when, for example, all but one blade are uncorrupted, a single blade is already such a small contribution to the final image that rejecting it or weighing it down makes only a small difference. With the large and continuous movement patterns performed in Paper III it becomes exceedingly difficult to separate the corrupted blades from the uncorrupted ones, since all blades are more or less affected by the head motions.

5.3.4 Limitations of Project III

The hypothesis that the PROPELLER RMC would correct any residual motion missed by the PMC was not clearly demonstrated. There are two reasons for this. First, the PMC updates provided by the WRAD had such a high precision that there was little left for the RMC to correct. Second, the PROPELLER trajectory by itself is quite forgiving to motion artifacts, similar to a radial trajectory, thereby making the additional improvements of the RMC hard to distinguish in the images, such as, for example, the comparison of PMC with PMC+RMC in Figure 46A. This could have been shown by including cartesian acquisitions to compare against.

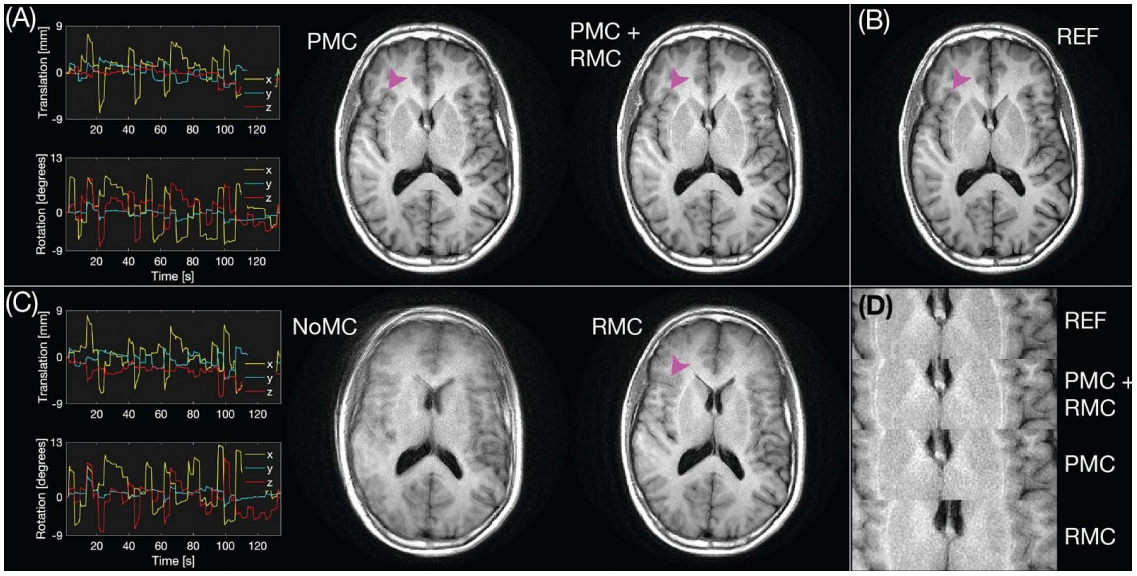

Figure 46. *Results from the stepwise motion scans.* ***(A)*** *Images acquired with PMC updates (with and without RMC) and the motion estimates to the left.* ***(B)*** *Reference image acquired when the subject remained still.* ***(C)*** *Images acquired without PMC updates (with and without RMC) and the corresponding motion estimates.* ***(D)*** *Enlarged images, showing the external capsule. The pink arrows point to anatomical differences between the RMC-only image and the rest. Reproduced from Paper III.*

The motion patterns were designed to challenge the proposed method; however, they are not based on realistic patient motions. Therefore, one could argue that clinical applicability is still to be proven. However, the motion patterns were extreme enough to hopefully encapsulate a majority of the possible patient motions.

6 Acknowledgments

Först vill jag tacka min handledare **Stefan Skare** för att han gav mig möjligheten och uppmuntrade mig att börja doktorera. Du sa en gång att du i rollen som handledare försöker vara "något mellan en blåslampa och en vän". Jag tycker att du har lyckats vara både och.

Jag vill rikta ett varmt tack till min bi-handledare och kollega **Enrico Avventi** för hjälp och stöd under processens gång. Inte minst är jag tacksam för att du alltid haft tid att sätta sig in i mina problem och lotsa mig rätt.

Mathias Engström! Utan dina visdomsord, både de seriösa och oseriösa, hade det inte varit lika roligt att doktorera. Du introducerade MR för mig på ett personligt och roligt sätt som fick mig att fastna för ämnet.

Om man kan säga att Stefan är pappa i forskningsgruppen så är **Henric Rydén** min doktorandbror**.** Utan dig hade det varit mycket svårare att färdigställa avhandlingen, då du har hjälp mig med både praktiska och teoretiska bekymmer. Samtidigt har det varit mycket värdefullt för mig att kunna dela den här resan med någon i samma situation.

I would like to extend my gratitude to **Tim Sprenger** and say thanks for all the fun and for bestowing so much knowledge on me. Your former supervisor told me once that you were his brightest and most creative student. After working with you for a couple of years, I can see why he said that.

Jag vill också visa uppskattning till min skugghandledare **Johan Berglund.** Du har varit en verklig förebild när det gäller vetenskapligt skrivande och tänkande.

I am also grateful for having **Adam van Niekerk** as a colleague. Your ingenuity and kindness really helped me get through this last year.

Yords Österman är en annan person jag vill tacka. Du bjöd tidigt in mig till att hjälpa till med undervisning – något jag lärt mig mycket av.

Axel “Angel Boy” Hartwig: Tack för att du bytte jobb så att det blev en ledig plats åt mig. Jag minns särskilt ditt varma välkomnande till gruppen när jag var ny exjobbare.

Tack **Magnus Mårtensson** för att du, när jag var ny, hjälpte mig att komma igång på ett engagerat vis.

Alla **kollegor på Karolinska** är värda ett stort tack – för att ni finns och för att ni gör neuroröntgen till en så rolig arbetsplats.

Jag vill tacka de chefer jag haft under tiden som doktorand: **Eva-Lena Zachrisson**, **Magnus Kaiser** och **Olof Flodmark.** För att ni har gett mig möjligheten att utvecklas i en fri forskningsmiljö och visat förtroende.

I'm grateful to **Kawin Setsompop** for agreeing to be my mentor and for lending me some confidence.

Tack **André**, **Arvid**, **Petter**, **Ludde** och **Frej** för er vänskap och ert stöd.

Tack till min otroliga lilla familj **Maria**, **Nell** och **Cosmo** för att ni hjälpt mig att glömma alla bekymmer jag haft med den här avhandlingen.

Min mamma **Ann Skillö:** Tack för att du alltid stöttar och tror på mig. Jag är också väldigt tacksam för resten av Skillö-släkten (inklusive **Stefan**!); mina mostrar **Helen** och **Kersti**, och min kusin **Li** som hejat på under de här åren.

7 References

1. Rabi II, Zacharias JR, Millman S, Kusch P. A New Method of Measuring Nuclear Magnetic Moment. Phys. Rev. 1938;53:318–318.

2. Bloch F, Hansen WW, Packard M. Nuclear Induction. Phys. Rev. 1946;69:127–127.

3. Purcell EM, Torrey HC, Pound RV. Resonance Absorption by Nuclear Magnetic Moments in a Solid. Phys. Rev. 1946;69:37–38.

4. Rigden JS. Quantum states and precession: The two discoveries of NMR. Rev. Mod. Phys. 1986;58:433–448.

5. Bloch F. Nuclear Induction. Physical Review 1946;70.

6. Hanson LG. Is quantum mechanics necessary for understanding magnetic resonance? Concepts Magn. Reson. 2008;32A:329–340.

7. Bernstein M, King K, Zhou X. Handbook of MRI Pulse Sequences. ELSEVIER SCIENCE; 2004.

8. Hoult DI. The solution of the bloch equations in the presence of a varying B1 field—An approach to selective pulse analysis. J. Magn. Reson. 1979;35:69–86.

9. Pauly J, Nishimura D, Macovski A. A k-Space Analysis of Small-Tip-Angle Excitation. Journal of Magnetic Resonance 1988;81.

10. Twieg DB. The k-trajectory formulation of the NMR imaging process with applications in analysis and synthesis of imaging methods. Med. Phys. 1983;10:610–621.

11. Ljunggren S. A simple graphical representation of fourier-based imaging methods. J. Magn. Reson. 1983;54:338–343.

12. Feinberg DA, Hoenninger JC, Crooks LE, Kaufman L, Watts JC, Arakawa M. Inner volume MR imaging: technical concepts and their application. Radiology 1985;156:743–747.

13. Bottomley PA, Hardy CJ. Two-dimensional spatially selective spin inversion and spin-echo refocusing with a single nuclear magnetic resonance pulse. J. Appl. Phys. 1987;62:4284–4290.

14. Shinnar M, Eleff S, Subramanian H, Leigh JS. The synthesis of pulse sequences yielding arbitrary magnetization vectors. Magn. Reson. Med. 1989;12:74–80.

15. Shinnar M, Bolinger L, Leigh JS. The use of finite impulse response filters in pulse design. Magn. Reson. Med. 1989;12:81–87.

16. Le Roux P. Exact synthesis of radio frequency waveforms. In: Proc. 7th SMRM,

Aug. 1988, p. 1049. ; 1988.

17. Pauly J, Le Roux P, Nishimura D, Macovski A. Parameter Relations for the Shinnar-Le Roux Selective Excitation Pulse Design Algorithm. IEEE 1991.

18. Haase A, Frahm J, Hänicke W, Matthaei D. 1H NMR chemical shift selective (CHESS) imaging. Phys. Med. Biol. 1985;30:341–344.

19. Hore PJ. Solvent suppression in fourier transform nuclear magnetic resonance. J. Magn. Reson. 1983;55:283–300.

20. Borwein J, Bailey D. Pascal's Triangle. In: Mathematics by Experiment: Plausible Reasoning in the 21st Century. A K Peters; 2003. pp. 45–48.

21. Ren J, Dimitrov I, Sherry AD, Malloy CR. Composition of adipose tissue and marrow fat in humans by 1H NMR at 7 Tesla. J. Lipid Res. 2008;49:2055–2062.

22. Alexander S. Spin-Echo Method for Measuring Relaxation Times in Two-Line NMR Spectra. Rev. Sci. Instrum. 1961;32:1066–1067.

23. Redfield AG, Gupta RK. Pulsed Fourier-Transform NMR Spectrometer for Use with H2O Solutions. J. Chem. Phys. 1971;54:1418–1419.

24. Keller PJ, Hunter WW Jr, Schmalbrock P. Multisection fat-water imaging with chemical shift selective presaturation. Radiology 1987;164:539–541.

25. Karl JH. An Introduction to Digital Signal Processing. Elsevier; 2012 p. 110.

26. Stirnberg R, Brenner D, Stöcker T, Shah NJ. Rapid fat suppression for three-dimensional echo planar imaging with minimized specific absorption rate. Magn. Reson. Med. 2015 doi: 10.1002/mrm.26063.

27. Ye Y, Hu J, Haacke EM. Robust selective signal suppression using binomial off-resonant rectangular (BORR) pulses. J. Magn. Reson. Imaging 2014;39:195–202.

28. Bastiaansen JAM, Stuber M. Flexible water excitation for fat-free MRI at 3T using lipid insensitive binomial off-resonant RF excitation (LIBRE) pulses. Magn. Reson. Med. 2017 doi: 10.1002/mrm.26965.

29. Meyer CH, Pauly JM, Macovski A, Nishimura DG. Simultaneous spatial and spectral selective excitation. Magn. Reson. Med. 1990;15:287–304.

30. Scheffler K. A pictorial description of steady-states in rapid magnetic resonance imaging. Concepts Magn. Reson. 1999;11:291–304.

31. Carr HY. Steady-State Free Precession in Nuclear Magnetic Resonance. Phys. Rev. 1958;112:1693–1701.

32. Scheffler K, Lehnhardt S. Principles and applications of balanced SSFP techniques. Eur. Radiol. 2003;13:2409–2418.

33. Hennig J, Nauerth A, Friedburg H. RARE imaging: a fast imaging method for clinical MR. Magn. Reson. Med. 1986;3:823–833.

34. Carr HY, Purcell EM. Effects of Diffusion on Free Precession in Nuclear Magnetic Resonance Experiments. Phys. Rev. 1954;94:630–638.

35. Meiboom S, Gill D. Modified Spin-Echo Method for Measuring Nuclear Relaxation Times. Rev. Sci. Instrum. 1958;29:688.

36. Mugler JP 3rd. Optimized three-dimensional fast-spin-echo MRI. J. Magn. Reson. Imaging 2014;39:745–767.

37. Hahn EL. Spin Echoes. Phys. Rev. 1950;80:580–594.

38. Hennig J, Weigel M, Scheffler K. Multiecho sequences with variable refocusing flip angles: optimization of signal behavior using smooth transitions between pseudo steady states (TRAPS). Magn. Reson. Med. 2003;49:527–535.

39. Hennig J, Weigel M, Scheffler K. Calculation of flip angles for echo trains with predefined amplitudes with the extended phase graph (EPG)-algorithm: principles and applications to hyperecho and TRAPS sequences. Magn. Reson. Med. 2004;51:68–80.

40. Weigel M, Hennig J. Contrast behavior and relaxation effects of conventional and hyperecho-turbo spin echo sequences at 1.5 and 3 T. Magn. Reson. Med. 2006;55:826–835.

41. Weigel M, Zaitsev M, Hennig J. Inversion recovery prepared turbo spin echo sequences with reduced SAR using smooth transitions between pseudo steady states. Magn. Reson. Med. 2007;57:631–637.

42. Weigel M, Hennig J. Development and optimization of T2 weighted methods with reduced RF power deposition (Hyperecho-TSE) for magnetic resonance imaging. Z. Med. Phys. 2008;18:151–161.

43. Weigel M, Helms G, Hennig J. Investigation and modeling of magnetization transfer effects in two-dimensional multislice turbo spin echo sequences with low constant or variable flip angles at 3 T. Magn. Reson. Med. 2010;63:230–234.

44. Busse RF, Brau ACS, Vu A, et al. Effects of refocusing flip angle modulation and view ordering in 3D fast spin echo. Magn. Reson. Med. 2008;60:640–649.

45. Park J, Mugler JP 3rd, Horger W, Kiefer B. Optimized T1-weighted contrast for single-slab 3D turbo spin-echo imaging with long echo trains: application to whole-brain imaging. Magn. Reson. Med. 2007;58:982–992.

46. Henkelman RM, Stanisz GJ, Graham SJ. Magnetization transfer in MRI: a review. NMR Biomed. 2001;14:57–64.

47. Parker DL, Buswell HR, Goodrich KC, Alexander AL, Keck N, Tsuruda JS. The application of magnetization transfer to MR angiography with reduced total power. Magn. Reson. Med. 1995;34:283–286.

48. Petrella JR, Grossman RI, McGowan JC, Campbell G, Cohen JA. Multiple sclerosis lesions: relationship between MR enhancement pattern and magnetization transfer effect. AJNR Am. J. Neuroradiol. 1996;17:1041–1049.

49. Dixon WT, Engels H, Castillo M, Sardashti M. Incidental magnetization transfer contrast in standard multislice imaging. Magn. Reson. Imaging 1990;8:417–422.

50. Melki PS, Mulkern RV. Magnetization transfer effects in multislice RARE sequences. Magn. Reson. Med. 1992;24:189–195.

51. Larkman DJ, Hajnal JV, Herlihy AH, Coutts GA, Young IR, Ehnholm G. Use of multicoil arrays for separation of signal from multiple slices simultaneously excited. J. Magn. Reson. Imaging 2001;13:313–317.

52. Moeller S, Yacoub E, Olman CA, et al. Multiband multislice GE-EPI at 7 tesla, with 16-fold acceleration using partial parallel imaging with application to high spatial and temporal whole-brain fMRI. Magn. Reson. Med. 2010;63:1144–1153.

53. Koopmans PJ, Boyacioğlu R, Barth M, Norris DG. Whole brain, high resolution spin-echo resting state fMRI using PINS multiplexing at 7 T. Neuroimage 2012;62:1939–1946.

54. Eichner C, Setsompop K, Koopmans PJ, et al. Slice accelerated diffusion-weighted imaging at ultra-high field strength. Magn. Reson. Med. 2014;71:1518–1525.

55. Dai E, Ma X, Zhang Z, Yuan C, Guo H. Simultaneous multislice accelerated interleaved EPI DWI using generalized blipped-CAIPI acquisition and 3D K-space reconstruction. Magn. Reson. Med. 2016 doi: 10.1002/mrm.26249.

56. Ivanov D, Poser BA, Huber L, Pfeuffer J, Uludağ K. Optimization of simultaneous multislice EPI for concurrent functional perfusion and BOLD signal measurements at 7T. Magn. Reson. Med. 2016 doi: 10.1002/mrm.26351.

57. Marami B, Scherrer B, Khan S, et al. Motion-robust diffusion compartment imaging using simultaneous multi-slice acquisition. Magn. Reson. Med. 2018 doi: 10.1002/mrm.27613.

58. Feinberg DA, Beckett A, Chen L. Arterial spin labeling with simultaneous multi-slice echo planar imaging. Magn. Reson. Med. 2013;70:1500–1506.

59. Eichner C, Jafari-Khouzani K, Cauley S, et al. Slice accelerated gradient-echo spin-echo dynamic susceptibility contrast imaging with blipped CAIPI for increased slice coverage. Magn. Reson. Med. 2014;72:770–778.

60. Schulz J, Boyacioğlu R, Norris DG. Multiband multislab 3D time-of-flight magnetic resonance angiography for reduced acquisition time and improved sensitivity. Magn. Reson. Med. 2016;75:1662–1668.

61. Ye H, Cauley SF, Gagoski B, et al. Simultaneous multislice magnetic resonance fingerprinting (SMS-MRF) with direct-spiral slice-GRAPPA (ds-SG) reconstruction. Magn. Reson. Med. 2016 doi: 10.1002/mrm.26271.

62. Müller S. Multifrequency selective rf pulses for multislice MR imaging. Magn. Reson. Med. 1988;6:364–371.

63. Auerbach EJ, Xu J, Yacoub E, Moeller S, Uğurbil K. Multiband accelerated spin-echo echo planar imaging with reduced peak RF power using time-shifted RF pulses. Magn. Reson. Med. 2013;69:1261–1267.

64. Conolly S, Nishimura D, Macovski A, Glover G. Variable-rate selective excitation. J. Magn. Reson. 1988;78:440–458.

65. Aigner CS, Clason C, Rund A, Stollberger R. Efficient high-resolution RF pulse design applied to simultaneous multi-slice excitation. J. Magn. Reson. 2016;263:33–44.

66. Goelman G. Two methods for peak RF power minimization of multiple inversion-band pulses. Magn. Reson. Med. 1997;37:658–665.

67. Wong E. Optimized phase schedules for minimizing peak RF power in simultaneous multi-slice RF excitation pulses. In: Proceedings of the 20th Annual Meeting of ISMRM, Melbourne, Victoria, Australia. ; 2012. p. 2209.

68. Abo Seada S, Price AN, Hajnal JV, Malik SJ. Optimized amplitude modulated multiband RF pulse design. Magn. Reson. Med. 2017;78:2185–2193.

69. Sharma A, Lustig M, Grissom WA. Root-flipped multiband refocusing pulses. Magn. Reson. Med. 2016;75:227–237.

70. Han V, Liu C. Multiphoton magnetic resonance in imaging: A classical description and implementation. Magn. Reson. Med. 2020;84:1184–1197.

71. Norris DG, Koopmans PJ, Boyacioğlu R, Barth M. Power Independent of Number of Slices (PINS) radiofrequency pulses for low-power simultaneous multislice excitation. Magn. Reson. Med. 2011;66:1234–1240.

72. Koopmans PJ, Boyacioğlu R, Barth M, Norris DG. Simultaneous multislice inversion contrast imaging using power independent of the number of slices (PINS) and delays alternating with nutation for tailored excitation (DANTE) radio frequency pulses. Magn. Reson. Med. 2013;69:1670–1676.

73. Bodenhausen G, Freeman R, Morris GA. A simple pulse sequence for selective excitation in Fourier transform NMR. J. Magn. Reson. 1976;23:171–175.

74. Eichner C, Wald LL, Setsompop K. A low power radiofrequency pulse for simultaneous multislice excitation and refocusing. Magn. Reson. Med. 2014;72:949–958.

75. Pruessmann KP, Weiger M, Scheidegger MB, Boesiger P. SENSE: sensitivity encoding for fast MRI. Magn. Reson. Med. 1999;42:952–962.

76. Griswold MA, Jakob PM, Heidemann RM, et al. Generalized autocalibrating partially parallel acquisitions (GRAPPA). Magn. Reson. Med. 2002;47:1202–1210.

77. Blaimer M, Breuer FA, Seiberlich N, et al. Accelerated volumetric MRI with a SENSE/GRAPPA combination. J. Magn. Reson. Imaging 2006;24:444–450.

78. Blaimer M, Choli M, Jakob PM, Griswold MA, Breuer FA. Multiband phase-constrained parallel MRI. Magn. Reson. Med. 2013;69:974–980.

79. Stäb D, Ritter CO, Breuer FA, Weng AM, Hahn D, Köstler H. CAIPIRINHA accelerated SSFP imaging. Magn. Reson. Med. 2011;65:157–164.

80. Setsompop K, Gagoski BA, Polimeni JR, Witzel T, Wedeen VJ, Wald LL. Blipped-controlled aliasing in parallel imaging for simultaneous multislice echo planar imaging with reduced g-factor penalty. Magn. Reson. Med. 2012;67:1210–1224.

81. Cauley SF, Polimeni JR, Bhat H, Wald LL, Setsompop K. Interslice leakage artifact reduction technique for simultaneous multislice acquisitions. Magn. Reson. Med. 2014;72:93–102.

82. Breuer FA, Blaimer M, Heidemann RM, Mueller MF, Griswold MA, Jakob PM.

Controlled aliasing in parallel imaging results in higher acceleration (CAIPIRINHA) for multi-slice imaging. Magn. Reson. Med. 2005;53:684–691.

83. Pinsky M. Introduction to Fourier Analysis and Wavelets. Brooks/Cole; 2002.

84. Glover GH. Phase-Offset Multiplanar (POMP) Volume Imaging: A New Technique. JMRI 1991.

85. Bilgic B, Gagoski BA, Cauley SF, et al. Wave-CAIPI for highly accelerated 3D imaging. Magn. Reson. Med. 2015;73:2152–2162.

86. Gretsch F, Marques JP, Gallichan D. Investigating the accuracy of FatNav-derived estimates of temporal B0 changes and their application to retrospective correction of high-resolution 3D GRE of the human brain at 7T. Magn. Reson. Med. 2018;80:585–597.

87. Atkinson D, Hill DL, Stoyle PN, Summers PE, Keevil SF. Automatic correction of motion artifacts in magnetic resonance images using an entropy focus criterion. IEEE Trans. Med. Imaging 1997;16:903–910.

88. Atkinson D, Hill DL, Stoyle PN, et al. Automatic compensation of motion artifacts in MRI. Magn. Reson. Med. 1999;41:163–170.

89. Haskell MW, Cauley SF, Wald LL. TArgeted Motion Estimation and Reduction (TAMER): Data Consistency Based Motion Mitigation for MRI Using a Reduced Model Joint Optimization. IEEE Trans. Med. Imaging 2018;37:1253–1265.

90. Pipe JG. Motion Correction With PROPELLER MRI: Application to Head Motion and Free-Breathing Cardiac Imaging. Magn. Reson. Med. 1999;42:963–969.

91. Nehrke K, Börnert P. Prospective correction of affine motion for arbitrary MR sequences on a clinical scanner. Magn. Reson. Med. 2005;54:1130–1138.

92. White N, Roddey C, Shankaranarayanan A, et al. PROMO: Real-time prospective motion correction in MRI using image-based tracking. Magn. Reson. Med. 2010;63:91–105.

93. Maclaren J, Armstrong BSR, Barrows RT, et al. Measurement and correction of microscopic head motion during magnetic resonance imaging of the brain. PLoS One 2012;7:e48088.

94. Sengupta S, Tadanki S, Gore JC, Welch EB. Prospective real-time head motion correction using inductively coupled wireless NMR probes. Magn. Reson. Med. 2014;72:971–985.

95. Olesen OV, Paulsen RR, Højgaard L, Roed B, Larsen R. Motion tracking for medical imaging: a nonvisible structured light tracking approach. IEEE Trans. Med. Imaging 2012;31:79–87.

96. Newbould R, Liu C, Bammer R. Colored noise and effective resolution: data considerations for non-uniform k-space sampling reconstructions. In: Proceedings of the international society of magnetic resonance in medicine. Vol. 14. ; 2006. p. 2939.

97. Tamhane AA, Anastasio MA, Arfanakis K. Image Noise Considerations for PROPELLER k-space Sampling. Proc. Intl. Soc. Mag. Reson. Med. 2006;14:1025.

98. Dixon WT. Simple proton spectroscopic imaging. Radiology 1984;153:189–194.

99. Schär M, Eggers H, Zwart NR, Chang Y, Bakhru A, Pipe JG. Dixon water-fat separation in PROPELLER MRI acquired with two interleaved echoes. Magn. Reson. Med. 2016;75:718–728.

100. Rydén H, Berglund J, Norbeck O, Avventi E, Skare S. T1 weighted fat/water separated PROPELLER acquired with dual bandwidths. Magn. Reson. Med. 2018 doi: 10.1002/mrm.27228.

101. Arfanakis K, Tamhane AA, Pipe JG, Anastasio MA. k-space undersampling in PROPELLER imaging. Magn. Reson. Med. 2005;53:675–683.

102. Li Z, Pipe JG, Aboussouan E, Karis JP, Huo D. A parallel imaging technique using mutual calibration for split-blade diffusion-weighted PROPELLER. Magn. Reson. Med. 2011;65:638–644.

103. Skare S, Newbould RD, Nordell A, Holdsworth SJ, Bammer R. An auto-calibrated, angularly continuous, two-dimensional GRAPPA kernel for propeller trajectories. Magn. Reson. Med. 2008;60:1457–1465.

104. Holmes JH, Beatty PJ, Rowley HA, et al. Improved motion correction capabilities for fast spin echo T1 FLAIR propeller using non-Cartesian external calibration data driven parallel imaging. Magn. Reson. Med. 2012;68:1856–1865.

105. Beatty PJ, Hargreaves BA, Gurney PT, Nishimura DG. A method for non-Cartesian parallel imaging reconstruction with improved calibration. In: Proc 15th Annual Meeting ISMRM, Berlin. ; 2007. p. 335.

106. van Niekerk A, Meintjes E, van der Kouwe A. A Wireless Radio Frequency Triggered Acquisition Device (WRAD) for Self-Synchronised Measurements of the Rate of Change of the MRI Gradient Vector Field for Motion Tracking. IEEE Trans. Med. Imaging 2019;38:1610–1621.

107. van Niekerk A, van der Kouwe A, Meintjes E. Toward “plug and play” prospective motion correction for MRI by combining observations of the time varying gradient and static vector fields. Magn. Reson. Med. 2019;82:1214–1228.

108. Maclaren J, Herbst M, Speck O, Zaitsev M. Prospective motion correction in brain imaging: a review. Magn. Reson. Med. 2013;69:621–636.

109. Maclaren J, Aksoy M, Ooi MB, Zahneisen B, Bammer R. Prospective motion correction using coil-mounted cameras: Cross-calibration considerations. Magn. Reson. Med. 2018;79:1911–1921.

110. Silver MS, Joseph RI, Chen CN, Sank VJ, Hoult DI. Selective population inversion in NMR. Nature 1984;310:681–683.

111. De Coene B, Hajnal JV, Gatehouse P, et al. MR of the brain using fluid-attenuated inversion recovery (FLAIR) pulse sequences. AJNR Am. J. Neuroradiol. 1992;13:1555–1564.

112. Polimeni JR, Bhat H, Witzel T, et al. Reducing sensitivity losses due to respiration and motion in accelerated echo planar imaging by reordering the autocalibration data acquisition. Magn. Reson. Med. 2016;75:665–679.

113. Pipe JG. Motion Corrected T1-Weighted PROPELLER FSE. Proc. Intl. Soc. Mag. Reson. Med. 2005;13:2236.

114. Listerud J, Mitchell J, Bagley L, Grossman R. OIL FLAIR: optimized interleaved fluid-attenuated inversion recovery in 2D fast spin echo. Magn. Reson. Med. 1996;36:320–325.

115. NEMA. Determination of Signal-to-Noise Ratio (SNR) in Diagnostic Magnetic Resonance Imaging.

116. O'Sullivan JD. A fast sinc function gridding algorithm for fourier inversion in computer tomography. IEEE Trans. Med. Imaging 1985;4:200–207.

117. Ashburner J, Friston KJ. Unified segmentation. Neuroimage 2005;26:839–851.

118. Busse RF, Hariharan H, Vu A, Brittain JH. Fast spin echo sequences with very long echo trains: design of variable refocusing flip angle schedules and generation of clinical T2 contrast. Magn. Reson. Med. 2006;55:1030–1037.

119. Morris Z, Whiteley WN, Longstreth WT Jr, et al. Incidental findings on brain magnetic resonance imaging: systematic review and meta-analysis. BMJ 2009;339:b3016.

120. Illes J, Kirschen MP, Edwards E, et al. Practical approaches to incidental findings in brain imaging research. Neurology 2008;70:384–390.

121. Norbeck O, Avventi E, Rydén H, Skare S. Inversion Recovery with SMS PROPELLER. In: Proc. Intl. Soc. Mag. Reson. Med. 25 (2017). ; 2017. p. 1487.

122. Sprenger T, Norbeck O, Berglund J, Rydén H, Avventi E, Skare S. EPIMix 3.0. In: Proceedings of the 27st Annual Meeting of ISMRM, Montréal, QC, Canada. ; 2019. p. 1190.

123. Wintersperger BJ, Runge VM, Biswas J, et al. Brain magnetic resonance imaging at 3 Tesla using BLADE compared with standard rectilinear data sampling. Invest. Radiol. 2006;41:586–592.

124. Alibek S, Adamietz B, Cavallaro A, et al. Contrast-enhanced T1-weighted fluid-attenuated inversion-recovery BLADE magnetic resonance imaging of the brain: an alternative to spin-echo technique for detection of brain lesions in the unsedated pediatric patient? Acad. Radiol. 2008;15:986–995.

125. Naganawa S, Satake H, Iwano S, et al. Contrast-enhanced MR imaging of the brain using T1-weighted FLAIR with BLADE compared with a conventional spin-echo sequence. Eur. Radiol. 2008;18:337–342.

126. Attenberger UI, Runge VM, Williams KD, et al. T1-weighted brain imaging with a 32-channel coil at 3T using TurboFLASH BLADE compared with standard cartesian k-space sampling. Invest. Radiol. 2009;44:177–183.

127. Alkan O, Kizilkiliç O, Yildirim T, Alibek S. Comparison of contrast-enhanced T1-weighted FLAIR with BLADE, and spin-echo T1-weighted sequences in intracranial MRI. Diagn. Interv. Radiol. 2009;15:75–80.

128. Kwag E, Lim SM, Park JE, Chae IH. Arterial hyperintensity on BLADE fluid-attenuated inversion recovery images (FLAIR) in hyperacute territorial

infarction: comparison with conventional FLAIR. Eur. Radiol. 2014;24:2045–2051.

129. Jiang H, Wang S, Xian J, Chen Q, Wei W. Efficacy of PROPELLER in reducing ocular motion artefacts and improving image quality of orbital MRI at 3 T using an eye surface coil. Clin. Radiol. 2019;74:734.e7–734.e12.

130. Feinberg DA, Setsompop K. Ultra-fast MRI of the human brain with simultaneous multi-slice imaging. J. Magn. Reson. 2013;229:90–100.

131. Gagoski BA, Bilgic B, Eichner C, et al. RARE/turbo spin echo imaging with Simultaneous Multislice Wave-CAIPI. Magn. Reson. Med. 2015;73:929–938.

132. Norbeck O, Avventi E, Ryden H, Berglund J, Sprenger T, Skare S. Pseudo-3D PROPELLER. In: Proc. Intl. Soc. Mag. Reson. Med. 26 (2018). ; 2018. p. 2659.

133. Madhusoodhanan S, Paul JS. A quantitative survey of GRAPPA reconstruction in parallel MRI: impact on noise reduction and aliasing. Concepts Magn. Reson. 2015;44A:287–305.

134. Ernst RR, Anderson WA. Application of Fourier Transform Spectroscopy to Magnetic Resonance. Rev. Sci. Instrum. 1966;37:93–102.

135. Crooijmans HJA, Gloor M, Bieri O, Scheffler K. Influence of MT effects on T(2) quantification with 3D balanced steady-state free precession imaging. Magn. Reson. Med. 2011;65:195–201.

136. Mugler JP 3rd, Brookeman JR. Three-dimensional magnetization-prepared rapid gradient-echo imaging (3D MP RAGE). Magn. Reson. Med. 1990;15:152–157.

137. Christensen KA, Grant DM, Schulman EM, Walling C. Optimal determination of relaxation times of fourier transform nuclear magnetic resonance. Determination of spin-lattice relaxation times in chemically polarized species. J. Phys. Chem. 1974;78:1971–1977.

138. Olsson H, Andersen M, Lätt J, Wirestam R, Helms G. Reducing bias in dual flip angle T1 -mapping in human brain at 7T. Magn. Reson. Med. 2020 doi: 10.1002/mrm.28206.

139. Yoneyama M, Nakamura M, Obara M, et al. Hyperecho PROPELLER-MRI: Application to rapid high-resolution motion-insensitive T2-weighted black-blood imaging of the carotid arterial vessel wall and plaque. J. Magn. Reson. Imaging 2016 doi: 10.1002/jmri.25377.

140. Norbeck O, Sprenger T, Avventi E, et al. Optimizing 3D EPI for rapid T1 -weighted imaging. Magn. Reson. Med. 2020 doi: 10.1002/mrm.28222.